UNIVERSITÀ DEGLI STUDI DI BERGAMO
Dipartimento di Ingegneria e Scienze Applicate

Dottorato di ricerca in
TECNOLOGIE PER L'ENERGIA E L'AMBIENTE

XXVIII ciclo

Anno 2017

CHARACTERIZATION OF DYNAMIC PROCESSES OF IMMISCIBLE DISPLACEMENT IN POROUS MEDIA

Doctoral thesis:

Diego Casagrande

Supervisor:

Prof. Francesco Bassi

Contents

List of Tables

List of Figures

Summary

The proposed research work has been developed focusing on three modern techniques for the quantitative characterization of porous materials and visualization of two-phase immiscible flow through their pore space: pore-scale numerical simulation, X-ray radiography and X-ray tomography. First of all, it is wise addressing the motivations sustaining the present research. To this end, let us recall the qualitative definition of two key parameters which, more than others, affect the dynamics of two-phase flow in porous media: *relative permeability* and *capillary pressure*.

Relative permeability, k_r henceforth, relates the flow rate of a phase in a multi-phase system through a porous medium to the applied pressure gradient. In other words, the relative permeability is related to the effectiveness of the applied pressure gradient in squeezing a single phase through a porous material, interested by a multi-phase flow. It depends on several factors, such as the nature of the porous medium (porosity, tortuosity, specific surface area, etc...), its wettability properties, the pore-scale Reynolds number, the saturation of the voids by the considered phase, the intrinsic phase-averaged velocity of the phase, i.e. the actual velocity of the phase throughout the void "channels". In addition, k_r is characterized by a hysteretical behaviour, i.e., its value depends on the history of the flow through the pore space.

Capillary pressure, P_c hereafter, is defined as the pressure jump occurring across a fluid-fluid interface within a multi-phase mixture. It depends on the same local quantities as k_r and it is also affected by hysteresis.

Well, why are k_r and P_c so important in the ensuing discussion? Actually, they are two key quantities entering the mass- and momentum-balance equations of multiphase flow through porous media: thus, one cannot "model" a multiphase flow through a porous medium without at least a rough knowledge of k_r and P_c. And, in turn, why should one care so much about modeling such flows? The straight answer to this question is: there is a branch of practical applications involving such flows, as oil/brine or gas/brine flow through oil and gas reservoirs during primary (i.e., not "assisted") or secondary (i.e., "assisted" or "forced") recovery, hydrogen/water flow through the membranes of fuel cells, vapor/liquid flow through the porous layers within heat pipes and many others. This should be enough to motivate the interest towards measurement techniques capable of providing reasonably accurate values of k_r and P_c. In this respect, the opacity of most porous media of practical relevance

(e.g. reservoir rocks, metal foams, etc...), introduces an additional complication that prevents the use of any direct or indirect measurement method relying on optical access. Indeed, until few years ago, curves relating k_r and P_c to the average phase saturation were obtained by time-demanding experimental techniques measuring the pressure drop throughout a cylindrical rock plug of porous medium, interested by a known flow rate of a fluid phase. These indirect measurement methods yield mean values of k_r and P_c throughout the sample and relate them to the average phase saturation within the sample. While this limitation is somehow acceptable for the wetting fluid phase in a binary mixture, as it tends to form a continuous fluid network throughout the entire porous domain, "global" measurements on the non-wetting phase are often misleading, as this phase tends to break-up into isolated fluid parcels and only those parcels connected to the terminal sections of the sample "interact" with the measurement system.

So far, I have been trying to convince that a reasonably accurate estimate of relative permeability and capillary pressure has relevant practical consequences. Let's now address the different measurement approaches investigated in this thesis: post-processing of either radiographic and tomographic images and micro-scale numerical simulations.

X-ray tomography is a quick and non-destructive technique widely employed in geosciences, which allows to characterize the internal structure of an object. The porous medium being inspected intercepts and attenuates the X-ray beam. Tomographic reconstruction tools allows exploiting the intensities of the emerging X-rays and decomposing the object into a very large number of very small (e.g. few μm per edge) cubic blocks, named "voxels" labelled either void or material. Thus X-ray tomography returns also indirect information about the material occupying each voxel. The 3D array of voxels making up the porous space is suitable for pore space morphological measurements. It must be converted into a computational mesh, before being usable for numerical simulation. There exist different approaches to accomplish this task. In the present work, each voxel is associated to a computational cell. This choice yields a rough, step-wise representation of the pore/grain interface (i.e. the porous matrix bounding surface) but guarantees very high mesh quality, with positive consequences on the convergence rate in the numerical solution of the governing equations. The computational mesh resulting from the sequence of X-ray tomography and mesh generation processes is referred to as *digital model*.

Pore-scale numerical simulation is a relatively modern approach to study the mechanical, electrical, hydraulic and thermal properties of porous media (Krishnan et al., 2006; Bai and Chung, 2011; Mostaghimi et al., 2012). The fundamental governing equations are solved within the fluid occupying the void spaces . The accurate geometric information required to implement this method comes from X-ray tomography, which provides a "block-wise" representation of the porous medium. Two-phase flow numerical simulations have been performed on the digital models

of reservoir rock samples. Procedures for estimating k_r and P_c thereof have been proposed and tested. Based on the gained experience, I may state that the pore-scale numerical measurement of k_r and P_c can be attempted for porous systems characterized by an evident homogeneity, so that a numerical simulation interesting a limited number of pores may be representative of the whole porous system. Duo-film metal foams are an example thereof. Nevertheless, porous systems such as reservoir rocks are characterized by strong inhomogeneity, from pore-scale to macroscopic scale (e.g. high permeability fractures in reservoir formations). Thus, a very large representative volume or, alternatively, a very large number of relatively-small samples, should be tomographed and simulated. Limitations of present tomographic systems and computational resources prevent either of these possibilities, in the near future.

Tomographic experiments have been carried out at the Delft University of Technology. A state of the art commercial tomographic system devoted to multiphase experiments has been made available for high resolution visualization of the fluids inside rock samples. With fluids at rest the local curvature of the interface could be measured with a code developed in-house and, in turn, a direct estimate of P_c could be derived via Young-Laplace relationship. Also X-ray radiographic (in contrast to tomographic) experiments have been performed. These allowed to track the movement of the fluid interface as one fluid is injected and displaces the occupying one. Fluid saturation versus time profiles could be recorded and used to constrain a "history-match" procedure for the calculation of hydraulic properties of the rock.

Moreover, the effect of wettability on the sample filling (temporal evolution of the sample saturation) has been investigated by the implementation of a dynamic contact angle model which takes into account a variability of the contact angle between two immiscible fluids at the solid wall, according to a widely accepted wetting theory. The model has been previously tested on a simple geometry, where a water capillary filling has been mimicked.

The most noteworthy results of this research work have been published in a number of scientific articles (see List of publications).

Acknowledgements

I would first like to express appreciation and deep gratitude to my tutors, Prof. Gianni Schena and Prof. Marzio Piller. Without their support, advice and encouragement this thesis would not have been possible. I am grateful for the trust and confidence they placed in me and for the opportunity they offered me to be part of their research group. I would also like to express my gratitude to my supervisor, Prof. Francesco Bassi.
My sincere acknowledgement goes to the University of Bergamo, for the support given to me and for funding my PhD.
I would also like to thank the Department of Petroleum Engineering at the Delft University of Technology who have financed my stay abroad and has made available its laboratory facilities. I am really grateful to Prof. Pacelli Zitha who supervised and encouraged my research activity in Delft, instilling me his enthusiasm. A special thank goes to my colleagues Nikita Lenchenkov, Durgesh Kawale, Ania Peksa, Elisa Battistutta and Saskia Roels for their precious advices and help and to Wim Verwaal, Marc Friebel and Ellen Meijvogel, whose expertise and technical support have been essential for the success of our work.
To my fantastic friends, my greatest hug: they know how to fill up my life with happiness.
To my marvelous family, for their unceasing presence and love, I address my everlasting thanks and all my gratitude. Their generosity and way of being contribute to make me the person I am. To my "little" sister, who is the brightest sun in every, even rainy, day.
... And my unconditional love to my Katy, the best partner I could ever wish to share my life with. To her hand, which constantly keeps mine firmly. To her gifted and gentle soul, that makes me feel the luckiest guy.

List of publications

Piller M., **Casagrande D.**, Schena G., Santini M. *Pore-scale simulation of laminar flow through porous media.* Journal of Physiscs: Conference Series. Vol. 501 (2014). doi:10.1088/1742-6596/501/1/012010

Casagrande D., Piller M., Santini M., Schena G. *Characterisation of water-oil drainage process through a reservoir rock sample by digital core analysis.* International Journal Oil, Gas, Coal Technology. Vol. 8, no. 4, pp. 399–416 (2014). doi:10.1504/IJOGCT.2014.066300

Casagrande D., Schena G., Piller M. *Dynamic wetting in morphologically complex porous media.* Presented at 32^{nd} UIT Heat Transfer Conference, Pisa, 23-25 June 2014.

Casagrande D., Piller M., Schena G. Zitha, P. L. J. *X-ray radiographic imaging of unsteady flows in porous media.* Journal of Flow Visualization & Image Processing, Vol. 22 (1-3), pp. 1–14 (2015). doi:10.1615/JFlowVisImageProc.2016016488

Piller M., **Casagrande D.**, Schena G., Zitha, P. L. J. *Accuracy and reliability of capillary pressure estimate based on fluid-fluid interface curvature.* Submitted. Under review.

Chapter 1

Porous media and multiphase flows

1.1 Introduction

Porous media include a wide range of materials, from natural media (sands, soils, sandstones, carbonates, granites and others) to industrial materials (filters, ceramics, metal foams). They are employed everywhere in nature, science and technology. In particular, scientists, geologists and engineers dealing with production of oil and gas or movement of water and contaminants through the ground have great interest in studying geological materials, measure or estimate their properties, comprehend the essential mechanisms governing multiphase fluid flows and study the mutual interactions between fluids and rock.

1.2 Properties of a porous medium

A porous medium is defined as a portion of space that is occupied partly by a solid phase (*solid matrix*) and partly by voids (*pore space*). Because of its random and heterogeneous nature, the characterization of a porous sample is a thorny affair which requires an appropriate definition of representativeness. Bear (1972) suggests to define a Representative Elementary Volume (REV), that is the minimum volume U_o for which the measured property does not depend to the sample volume. Indicating with S_o the surface area of U_o, it must intersect both the void space and the solid matrix with corresponding area of intersection equally distributed over S_o. Let's consider a volume ΔU_i containing a sufficient number of pores and grain and its centroid P. Porosity ϕ_i, applied to the volume ΔU_i, is defined as follows:

$$\phi_i = \frac{(\Delta U_{porous})_i}{\Delta U_i}; \tag{1.1}$$

where ΔU_{porous} is the pore volume associated to ΔU_i. The relation (1.1) demonstrates how porosity depends on the choice of ΔU_i: as we change the volume ΔU_i, the corresponding value of ϕ_i may vary significantly, as shown in Figure 1.1. A limit value, denoted with ΔU_o, points out the transition from microscopical inhomogeneity domain to macroscopic domain (porous media domain). Above this value porosity is almost constant and possible deviations are due exclusively to medium heterogeneity.

The definition of REV is the first step to pass from the microscopic or molecular level of description to a macroscopic level, which lays on the assumption that a fluid phase is a continuous medium that completely fills the space and "*at every point and at every instant of time, kinematic and thermodynamic variables can be assigned, which are continuous and differentiable functions of the spatial coordinates and of time*" (Bear, 1984). The macroscopic level of handling flows in porous medium implies that it is necessary to associate with each point of the space average quantities, since punctual, fluctuating values are meaningless for practical purposes. Averaging, over ΔU_o, permits to remove the effect of microscopic heterogeneity without ignoring the macroscopic features of the medium. A modern interpretation of REV relies on the availability of a sufficient number of samples, in order to define representative statistical moments (Kanit et al., 2003). Evidently, different REVs should be defined for each of the physical properties of the medium (porosity, grain size, etc...).

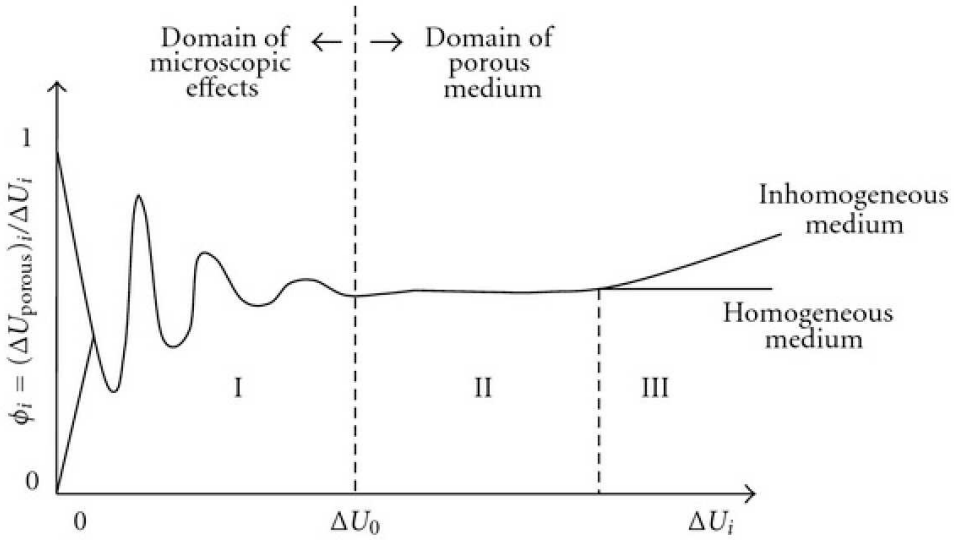

Figure 1.1: Definition of REV for porosity. Adapted from Bear (1972).

In general total **porosity** ϕ is defined as the fraction of bulk volume occupied by pores. A part of the total porosity, named effective porosity or kinematic porosity,

is made up of interconnected, open-to-flow pores, whereas the remaining are unconnected or blind pores. From the fluid-dynamic point of view, unconnected pores can be equated with the solid matrix. Hence porosity can be expressed as follows:

$$\phi = \frac{V_P}{V_T} \tag{1.2}$$

where V_P is the total pore volume and V_T is the total volume of the sample (bulk volume). According to this definition, porosity of porous media could range from 0 to 1, but most sedimentary rocks (main constituents of hydrocarbon reservoirs) have porosities less than 50%.

The nature of reservoir rocks not only determines the amount of fluids that can be trapped within the pore space, but also quantifies the ability of a fluid to flow through the channel networks that constitute the pore system. The measure of the aptitude of a rock to transmit a fluid is called permeability.

For a medium sample completely saturated by a single fluid phase, we talk of **absolute permeability**. The absolute permeability (coefficient) k is defined by the well-known Darcy's law:

$$Q = -\frac{Ak}{\gamma}\frac{\Delta P}{\Delta L} \tag{1.3}$$

where γ [Pa $\cdot$ s] is the fluid dynamic viscosity, A [m^2] is the cross-sectional area of the sample, $\Delta P/\Delta L$ is the pressure gradient and Q is the volumetric flow rate.

The (1.3) is a semi-empirical law and neglects gravitational effects. Assuming a constant pressure drop, it determines a direct proportionality between the absolute permeability k and the flow rate Q: higher is k, higher is Q and the capacity for flow. The unit of measurement of k is Darcy, where 1 Darcy $= 0.987 \times 10^{-8}$ cm^2. The Darcy's law is valid when problems of fluids saturating the pore space of porous materials are handled at the macroscale and the hypothesis of continuum is the basic assumption.

The absolute permeability is an own property of a porous medium and includes in itself a large number of physical and hydraulic characterisctics. The exclusive dependance of permeability on porosity may be criticized. In fact, even though a formation is usually considered homogeneous and isotropic, there is no specific trendline between permeability and porosity values and the correlation is purely qualitative. High porosity stones (pumice stones) can have zero permeability. Indeed the absolute permeability should be more accurately expressed as a function of porosity, pore size, grain size (see Figure 1.2), specific surface area, irreducible and residual fluid saturations.

Many models have been proposed in literature, which aim to predict this hydraulic property. According to Hagen-Poiselle's theory, the porous medium can be described with a tube-bundle model and the absolute permeability can be estimated

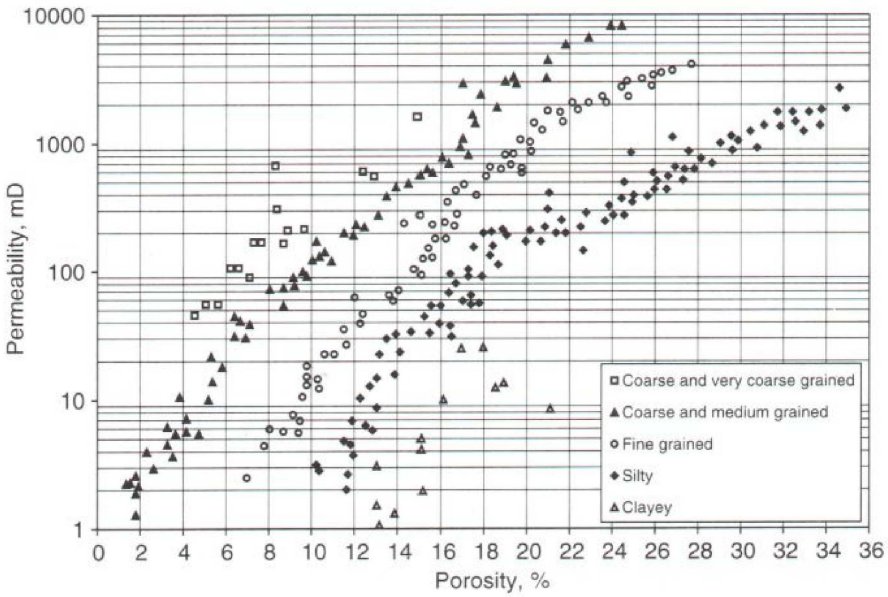

Figure 1.2: Influence of grain size in the relationship between permeability and porosity. Adapted from Chilingarian (1927).

by means of the widely used Kozeny-Carman (Kozeny, 1927; Carman, 1937) relation. It correlates porosity to permeability in a simplistic model, since the permeable medium is represented with a uniform cross-section and does not provide alternative pathways for fluid flow. The development of the Kozeny-Carman relation outlined by Lake and Panda (1994) leads to Eq. (1.4):

$$k = \left(\frac{1}{2\tau a_{v,gr}^2}\right)\frac{\phi^3}{(1-\phi)^2} \tag{1.4}$$

where τ and $a_{v,gr}$ indicate respectively the so-called tortuosity (ratio of the mean effective flow path length through a porous medium to the thicness of the medium) and the specific surface area (total area exposed to flow within the pore space per unit of grain volume), respectively. Thus, k increases strongly with ϕ and decreases weakly with τ, because the low "power" reduces its effect. The range of uncertainty in ϕ is moderate, τ cannot be measured directly. Unlike porosity, τ depends mainly on pore space geometry and has values greater than 1.

Other relations provide more complicated permeable medium models (Dullien, 1992) that include correction factors for pore non-uniformities and relate permeability to various free parameters, such as shape factor and local roughness. The limitation of these models is that they require independent determination of the above mentioned parameters, whose estimation is generally empirical.

1.3 Fluid-fluid interaction

Fluids in porous rocks permeate the cahotic and complex topology of the pore space. Type and nature of fluids and solid grains getting in contact with them determine both rock-fluid mutual interactions and the evolution of the ongoing displacement. Frequently more than one phase (gaseous or liquid phase) can flow simultaneously and fill the pore space.

In a reservoir oil, water and gas generally coexist in an immiscible state. However, as a common practise, chemicals can be injected into the reservoir to make water more miscible with oil. This technique has the effect to increase the overall mixture solubility, which is the main peculiarity of Enhanced Oil Recovery (EOR) methods. We talk about chemical (or micellar) flooding. This type of flood is characterized by a chemical slug, generally a mixture of water, surfactant, a cosurfactant and salt (i.e. sodium chloride) that is able to solubilize the trapped oil it encounters, displacing more oil than conventional methods for oil recovery. Therefore fluid flows in porous media can be distinguished into two broad categories: miscible and immiscible displacements. The physics of each of these displacements is significantly different, as in these processes system wettability and fluid-fluid interfacial tension, which will be addressed in the following section, play an important role.

Miscible displacements tipify floodings with no capillarity and nearly zero interfacial tension. When two fluids get in contact, a transition zone of hydrodynamic dispersion between them is immediately created.

Immiscible displacements involve fluids with no-zero interfacial tension and capillarity represents a driving force.

Our research focuses mainly on oil and water. Since oil and aqueous phases are generally considered immiscible, here we deal only with immiscible displacements. In other words, we ignore phenomena of dissolution of one phase into another one. Moreover we neglect related phenomena of adsorption-desorption and possible chemical interactions between the minerals constituting the rock matrix and the fluids filling the pore system (i.e. surface charges) or processes of rock alteration by circulating fluids (erosion, deposition, cementation), which unavoidably change physical and electrical properties of both rock and fluids and whereof study demands a detailed knowledge of physics and chemistry at nano-scale.

As previously asserted, the absolute permeability is an intrinsic property of the permeable medium and does not suffice to describe the dynamics of multiphase flow systems. To this end, other properties such as **wettability**, **interfacial tension**, **relative permeability** and **capillary pressure** must be introduced.

1.3.1 Wettability and interfacial tension

Immiscible fluids occupying simultaneously the void space of porous media compete for the occupancy of the pore-grain interface. The configuration of the well-defined

interface that separates the immiscible fluids is pinpointed by the relative wettability of the solid surface to the fluids. In other words, wettability is the parameter used to describe the relative adhesion of two immiscible phases to a solid surface and the preferential tendency of one of them to wet the surface. This phase is identified as the *wetting phase*, while the other is the *non-wetting phase*.

The molecules within each fluid attract each other with the same force in all directions, whereas molecules at the interface undergo an inward-directed force that tends to minimize the surface into a spherical surface. This phase boundary force is called *interfacial tension* or *surface tension* σ [N/m]. From a thermodynamic perspective, it is defined as the energy required to increase the area of the phase interface A by one unit:

$$\sigma = \left(\frac{\partial G}{\partial A}\right)_{T,P} \tag{1.5}$$

where G is the Gibbs free energy.

Interfacial tension (also IFT) together with the contact angle characterizes the wettability properties of a solid surface. Indeed the fluid-fluid interface intersects the solid surface at an angle θ, which is defined for an oil-water system by the Young's equation (1.6):

$$\cos(\theta) = \frac{\sigma_{os} - \sigma_{ws}}{\sigma_{ow}} \tag{1.6}$$

where:

σ_{os} = interfacial tension between solid and oil;
σ_{ws} = interfacial tension between solid and water;
σ_{ow} = interfacial tension between water and oil.

The difference between solid-oil and solid-water interfacial tensions takes the name of adhesion tension or wall adhesion and determines the wetting characteristics of the solid surface, either of partial or total wetting. Three wettability conditions may occur for partial wetting, depending on the values of wall adhesion and contact angle (measured in the aqueous phase), as follows:

1. **Water-wet**: the contact angle $\theta < 90°$ and the wall adhesion is positive.

2. **Intermediate wet**: the contact angle $\theta = 90°$ and the wall adhesion is zero.

3. **Oil-wet**: the contact angle $\theta > 90°$ and the wall adhesion is negative.

At a pore level, wettability may vary from strongly water-wet to strongly oil-wet, through intermediate wet and different wettability conditions may be observed within the same reservoir rock. As an example, sandstones are strongly water-wet

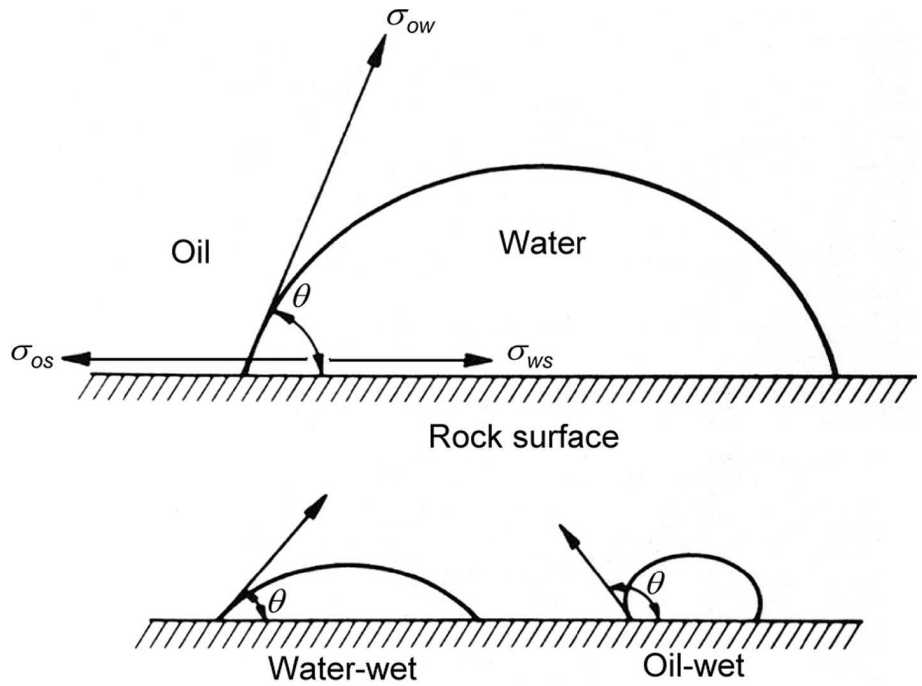

Figure 1.3: Relationship between interfacial tensions and contact angle, expressed by the Young's equation and different interface configurations for partial wetting.

before oil migrates from the source rock to the reservoir but a permanent wettability alteration may take place when oil enters the pores and some compounds (i.e. asphalthenes) are adsorbed by the solid surface, leading to mixed wettability conditions (Salathiel, 1973). The plausible interface configurations for a partially wetted system are sketched in Figure 1.3.

In general, in hydrocarbon-bearing formations, the wettability of reservoir rocks depends on both rock characteristics (hydrocarbons constituents and minerals of the solid surface) and fluid properties. Most sandstones, clastic sedimentary rocks whose dominant mineral is quartz, are water-wet. Indeed, silica are water-wet as well as calcite, but the rock behaviour is different in presence of different hydrocarbons. Isooctane is usually the non-wetting phase, nevertheless some crude oils getting in contact with a surface could change its wettability from water-wet to oil-wet (Willhite, 1986). In a water-wet water-oil-rock system, water tends to occupy the smaller pore bodies and covers the major portion of the pore-grain interface of the bigger pores. In the presence of preferentially oil-wet rocks saturated with water, oil will enter into the smaller pores displacing water from the external layers of larger pores. Definitely, a porous medium saturated with the non-wetting phase spontaneously imbibes the wetting phase.

Wettability is a fundamental property in fluid transport within porous rocks and its determination is extremely important in improving oil recovery techniques, by the

use of appropriate fluids. Moreover, wettability affects many other petro-physical properties, such as relative permeability and capillary pressure and has influence on the overall immiscible displacement evolution, the fluid distributions and the final saturations.

1.3.2 Immiscible displacements

Immiscible fluid flows can be subdivided into two categories, based on how fluid properties evolve during the process. We talk about *steady-state* and *unsteady-state* flows. The former occurs when all the macroscopic properties in all points of the system are time independent. Steady-state flows are driven by a constant pressure gradient and the fluid saturations are constant. At a point of the porous medium, changes in pressure and fluid velocity cause instantaneous changes in pressure or flow rate in any part of the system. No "displacement" takes place in the pore space, as each fluid follows its own path without interfering with flow of the other fluids. The latter occurs when the fluid properties change with respect to time and the fluid saturations vary with time at a given point. In nature, the majority of processes fall into this type of flow.

Within the unsteady-state category, we can distinguish two kinds of displacement depending on the wettability properties of the rock-fluid system:

- **DRAINAGE:** the porous sample is initially saturated with the wetting phase (e.g. water) and the injected fluid, the non-wetting one (e.g. oil), progressively fills the pore space displacing the water phase.
- **IMBIBITION:** the pore space is initially filled by the non-wetting phase and the injected wetting phase imbibes the sample, pushing the non-wetting one out of the void space. Basically, imbibition is the process where capillary forces act to make the wetting-phase spontaneously advance throughout the rock sample.

1.3.3 Saturation history and relative permeability

A fluid injected into a porous medium may saturate partially or totally the pore space. Saturation quantifies the space filled by a single phase and is defined as the ratio between the pore volume occupied by that phase and the total pore volume. In an oil-water displacement, we denote with S_w the water saturation and with S_o the oil saturation.

As mentioned before, in a strongly water-wet rock the pore-grain interface is covered with water. In that case oil will be mainly located in the centre of the pores. When a water-filled water-wet rock is oil-flooded during a laboratory test and

a full drainage is carried out, the sample is brought to *irreducible water saturation* $S_{w,i}$ [1] and water is restricted to thin layers covering the pore walls. Theoretically, keeping on flooding albeit at infinitely long displacement time, it is possible to remove even the smallest amount of pellicular water, so that $S_{w,i} = 0$ for a perfect water-wet system. The irreducible water saturation of reservoir rocks, whose degree of water-wetness is moderate, is quite low (about 10% of the pore space). After the subsequent water-flooding (imbibition) performed to produce oil, a significant amount of oil remains trapped in the form of floating and disconnected blobs. The *residual oil saturation* $S_{o,r}$ corresponds to the unmovable oil within the pores. For a water-wet reservoir rock $S_{o,r}$ is around 30%.

The absolute permeability describes the propensity of a porous medium to be traversed by a single fluid. When two competing immiscible fluids share the pore space, a **relative permeability** for each fluid can be defined. It quantifies how one fluid is hindered by the other and is the result of several factors: nature of the rock (porosity, tortuosity, specific surface area, etc...), relative wetting characteristics of rock and fluids (through the contact angle θ), saturation of the pores by the considered phase and saturation history, flow conditions (i.e. the actual velocity of the phase throughout the interconnected "channels" of the pore space).

The relative permeability k_r can be expressed as the ratio between the effective permeability of a rock partially filled with a fluid and the absolute permeability of the completely saturated rock. Considering a sample whose pore space is completely saturated with the two fluids ($S_w + S_o = 1$), the relationships between relative permeabilities for water (k_{rw}) and oil (k_{ro}) and the corresponding saturations are:

$$k_{r,w} = \frac{k_w(S_w)}{k_w|_{S_w=1}} \tag{1.7}$$

$$k_{r,o} = \frac{k_o(S_o)}{k_o|_{S_o=1}} \tag{1.8}$$

The Darcy's law is extended for two-phase flows and the expressions for an oil-water system are independently expressed as follows:

$$Q_w = -\frac{A\,k\,k_{r,w}}{\mu_w}\frac{\Delta P_w}{\Delta L} \tag{1.9}$$

$$Q_o = -\frac{A\,k\,k_{r,o}}{\mu_o}\frac{\Delta P_o}{\Delta L} \tag{1.10}$$

[1] Connate water saturation $S_{w,c}$ indicates the lower water saturation found *in situ*.

where Q_w and Q_o are the flow rates and the products $k\,k_{r,w}$ and $k\,k_{r,o}$ the effective permeabilities to water and oil.

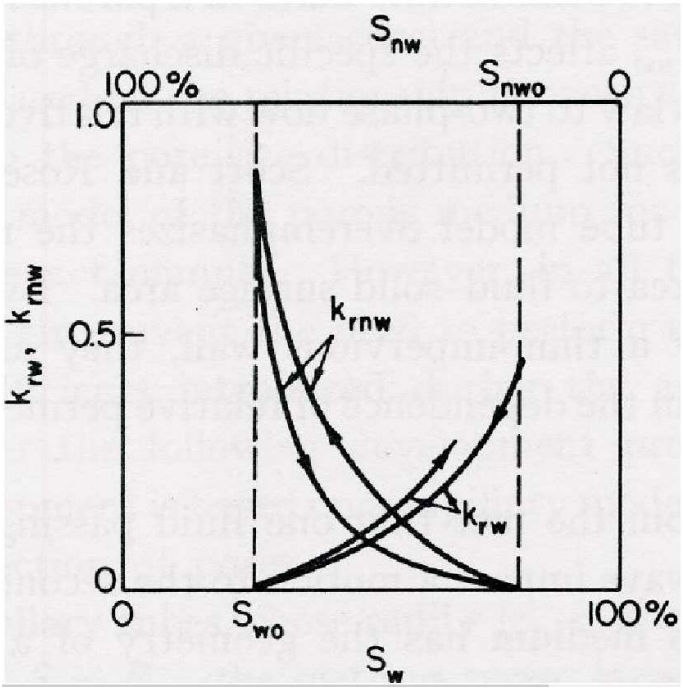

Figure 1.4: Typical relative permeability curves for wetting w and non-wetting nw phases, as a function of the wetting phase saturation. Effect of hysteresis during imbibition and drainage cycles. Adapted from Bear (1972).

Typical saturation-dependent relative permeability curves are shown in Figure 1.4, where the pedices $_{nw}$ and $_w$ denote non-wetting and wetting phases, in a generic two-phase system. The end-point relative permeabilities are the k_r at the saturation endpoints, S_{wo} and S_{nwo}, which define the remaining saturations of water and oil after extensive displacement has occured. As for relative permeability, the end-point saturation of each phase, for a specific displacement process, depends on the previous saturation history of that phase, the pore geometry, the wettabilities with respect to the competing phases. End-point saturation values could also depend on interfacial tension, when σ is very low and the rate of displacement, when it is very high. In Figure 1.4, for each phase two curves are drawn, one pertains to imbibition (towards increasing saturations in wetting phase), the other to drainage (towards decreasing saturations in wetting phase). This different behaviour of k_r, depending on the direction of saturation change, takes the name of *hysteresis*.

Values of k_r generally range from 0 to 1 over the entire saturation field, since permeability at $S = 100\%$ is greater than effective permeability at lower degree of saturation. However, sporadic cases of endpoint $k_r > 1$ have been observed

and reported in literature (Geffen et al., 1951; Odeh, 1959; Dullien, 1992; McPhee, 1994; Honarpour et al., 2000) and most of them ($1.4 < k_r < 2.4$) occur when the predominant phase is the non-wetting phase and the wetting one covers the rock surface in thin films: in water-wet water-oil systems $k_{r,o}(S_{w,i}) > 1$, while in oil-wet water-oil systems $k_{r,w}(S_{o,r}) > 1$. Geffen et al. (1951) experimentally observed an oil reative permeability over unity at irreducible water saturation and linked this singular behaviour to the dehydration of clay particles as the water content diminishes. Among several models proposed to explain this phenomenon, Berg et al. (2008) suggested a slip condition of the fluid-fluid interface: the non-wetting phase at the centre of the pore channels *slips* over the immobile layer of wetting phase, increasing the k_r beyond unity at immobile wetting fluid saturation.

1.3.4 Capillary pressure

Capillary pressure refers to the difference in pressure across the interface between two immiscible fluids in contact one with each other. The curvature of the interface describes the preferential property of one fluid to wet the solid surface (see Section 1.3.1). The pressure in the non-wetting phase is greater than the pressure in the wetting phase and consequently the curved interface is convex with respect to the non-wetting fluid and concave with respect to the wetting fluid. Therefore, the capillary pressure P_c can be mathematically expressed as follows:

$$P_c = P_{nw} - P_w \tag{1.11}$$

where P_{nw} and P_w are, respectively, the pressure of the non-wetting phase and the wetting phase. When the fluids wet, to the same extent, the solid surface (the contact angle between them is 90°), the pressure within each fluid is the same and the capillary pressure is zero. The standard definition of *macroscopic* P_c is derived directly from Eq. (1.11), *upscaling* the pressure difference between wetting and non-wetting phases over a REV:

$$P_c = < P_{nw} > - < P_w > \tag{1.12}$$

where $< P_{nw} >$ is the pressure of the non-wetting phase over the portion of the REV occupied by the non-wetting phase and $< P_w >$ is the pressure of the wetting phase over the portion of the REV containing the wetting phase (Bear, 1972; Scheidegger, 1974).

At equilibrium, the pressure difference between two adjacent immiscible fluids can be also related to the principal radii of curvature, R_1 and R_2, of the interface and the interfacial tension σ between the fluids, through the well-known Young-Laplace equation:

$$\Delta P = \sigma \left(\frac{1}{R_1} + \frac{1}{R_2} \right) \tag{1.13}$$

In a porous medium, Eq. (1.13) is the simplified expression of a *microscopic* capillary pressure. The extreme complexity of the pore system cannot be described analytically: since pore geometries or sizes can differ a lot from one pore to another, so will be the capillary pressure. Pores are often sketched out as capillary tubes. To determine the pore size, pore radii are assumed to be equivalent to the radius of the largest ball that can be inscribed within the pore. In this case the capillary pressure can be written as follows:

$$P_c = \frac{2\sigma cos(\theta)}{r} \tag{1.14}$$

where r is the radius of the inscribed ball.

According to Eq. (1.14), a particular P_c value is associated with a specific set of pores having the same radius r. Let us consider a water-wet reservoir rock filled with water. If the rock sample undergoes drainage by injecting oil, a pressure equal to capillary pressure must be applied to eject water out of the pores. At lower P_c oil will displace water out of bigger pores, at higher P_c water will be forced out of smaller pores. In this sense, for a drainage process, P_c can be defined as the pressure which must be overcome to force the non-wetting fluid to displace the wetting fluid in a capillary. Therefore the capillary pressure can be related to the wetting phase saturation within the capillary.

Figure 1.5 shows a typical P_c curve as a function of water saturation S_w for a water-wet water-oil system. It is common use to plot two curves, one for drainage and one for imbibition. The imbibition curve presents lower capillary pressure values than the drainage curve, for a fixed saturation, because of the natural tendency of the wetting fluid to saturate the rock. The hysteretical behaviour is the one observed for relative permeability. Note that for the drainage curve, at $S_w = 1$, a P_c greater than zero is required to force the oil phase to enter the void space. This pressure is named *entry pressure* or *threshold capillary pressure* $P_{c,t}$. In a primary drainage, oil does not invade a pore unless its pressure exceeds $P_{c,t}$, which can be approximately correlated to the pressure differential across the local oil-water interface inside the pore.

Several models have been proposed for capillary pressure, mostly relying on the thermodynamic theory applied to porous media. Hazzanizadeh and Gray (1993) stated that P_c can be expressed as function of the wetting phase saturation and specific area of the fluid-fluid interface per unit volume. Alpak et al. (1999) suggested that P_c can be related to solid areas that oil and water share in a porous material. The extent of these areas varies with grain size, rock local wettability of the rock and micro-scale effects.

Therefore P_c is not only function of factors such as interfacial tension σ, contact

angle θ, and pore size (through the curvature radius), but it also depends on saturation, saturation history and micro-scale heterogeneities (e.g. local roughness) of the pore/grain system.

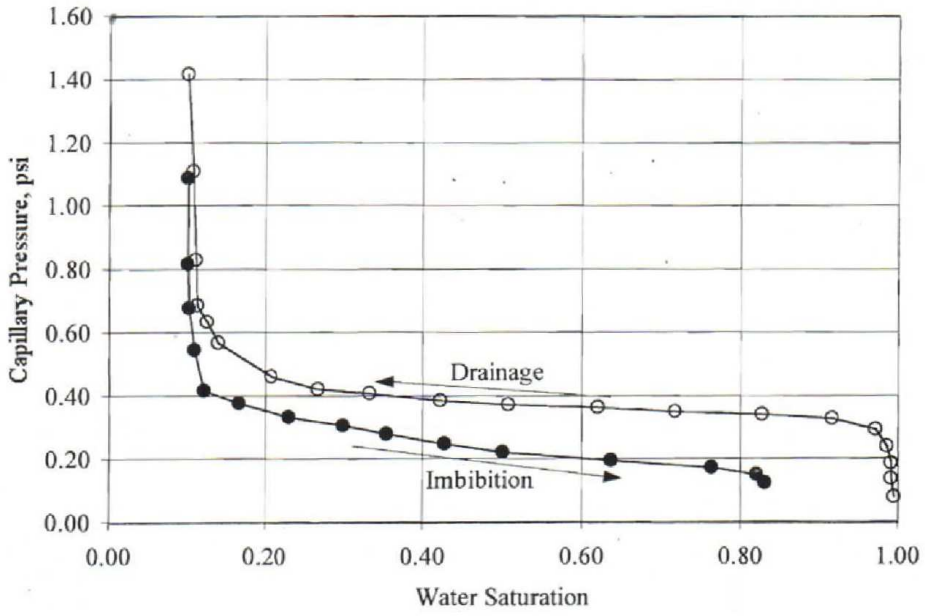

Figure 1.5: Typical capillary pressure curves as a function of the wetting phase saturation. Effect of hysteresis during primary drainage and secondary imbibition. Adapted from Morrow et al. (1973).

1.4 Estimation of k_r and P_c

Practically relative permeability and capillary pressure are derived by means of SCAL tests performed on cylindrical samples extracted from the reservoir rock. All laboratory tests can be classifiable into two methods:

- **Steady-state methods**: the two fluids are simultaneously injected into the core at constant flow-rates and pre-determined ratios. The saturations are measured directly via mass-balance and Darcy's law is employed.

- **Unsteady-state methods**: a single fluid is injected within the core, displacing the other fluid which initially fills the pores. The procedure is more rapid, but results may suffer of uncertainties ascribable to preliminary assumptions.

1.4.1 Steady-state methods

Steady-state methods are routinely used for relative permeability measurements. The sample is placed within a core holder and inlet and outlet sections are connected to pressure transducers. The pressure drop is measured. Metering pumps are used to inject the fluids and adjust the flow rates. In a water-oil displacement, water and oil are pumped-in at fixed volumetric ratio and the effluent rates are monitored until they are equal to the influent rates. At this point, it is assumed that a constant saturation is attained throughout the core and the *steady-state* condition is reached. The sample is weighted and the saturation is estimated, once total core mass M_T, dry core mass M_D, pore volume V_P and densities of the fluids ρ_w and ρ_o are known, as stated by the following relation:

$$S_w = \frac{M_T - M_D - V_P \cdot \rho_o}{V_P \cdot (\rho_w - \rho_o)} \tag{1.15}$$

The relative permeabilities $k_{r,w} = f(S_w)$ and $k_{r,o} = f(S_w)$ are derived from Eq. (1.9) and Eq. (1.10). The procedure is repeated, changing Q_w and Q_o, in order to get sufficient data to draw the entire relative permeability curve for each phase. The method is time-expensive, as a long time (sometimes several weeks) is required to reach the steady-state condition.

1.4.2 Unsteady-state methods

Unsteady-state methods, as they are named in the jargon of petro-physics (Akin, 2001; Toth et al., 2002), adopt a procedure where a single invading fluid displaces the defending fluid that initially saturates the pore space. Fluid production and pressure drop across the sample are continuously monitored and recorded (Loomis and Crowell, 1962). The acquired measurements require further processing to derive directly the relative permeability curves over a range of fluid saturations. Data processing for unsteady-state methods is much more complicated than for steady-state methods, as pressure gradient and fluid saturations vary with position and time throughout the sample. Indeed, the major difference in unsteady state techniques is that saturation equilibrium is not achieved during the test, reason why Darcy's law is not applicable.

The Buckley-Leverett theory (Buckley and Leverett, 1942) for incompressible and immiscible fluid displacement is the basis for all calculations. The Buckley-Leverett equation (1.16) represents the change in saturation through a one-dimensional porous medium and relates partial derivatives of phase saturation in space and time with fluid viscosities, volumetric flow rates and relative permeabilities. For a water-oil displacement:

$$\frac{\partial S_w}{\partial t} = u(S_w)\frac{\partial S_w}{\partial x} \qquad u(S_w) = \frac{Q}{\phi\, A}\frac{df_w}{dS_w} \tag{1.16}$$

where $Q = Q_w + Q_o$ is the total flow rate, f_w is the water fractional flow rate. The fractional flow rate f_i is the ratio between the flow rate of the $i-th$ phase Q_i and the total flow rate Q. When capillary pressure gradients and gravitational effects can be neglected, $f_w = f(S_w)$ and only depends on relative permeabilities and viscosities, as follows:

$$f_w = \frac{1}{1 + \dfrac{k_{ro}}{k_{rw}}\dfrac{\gamma_w}{\gamma_o}} \tag{1.17}$$

The Johnson-Bossler-Naumann (JBN) method (Johnson et al., 1959) is derived from Buckley-Leverett theory and is the most used for calculating relative permeabilites from unsteady-state displacement tests. JBN solution does not fully comply with practical experiments, as it neglects capillary and gravitational forces and assumes high flow rates in order to avoid *capillary end* effects (extremely high wetting phase saturation at the outlet section of the core). In addition it assumes that the core sample is homogeneous. The method provides relative permeability values for saturations higher than the breakthrough[2] saturation. Alternatively to JBN method that requires constant injection rate, Toth et al. (2002) have proposed a procedure that is more general for it may be applied also to constant pressure-drop experiments.

Capillary pressure is sometimes determined in conjunction with relative permeability measurements, even though a common practice is to measure P_c using distinct procedures. Methods for measuring capillary pressure may be grouped under three main classes: mercury methods, porous-plate methods and centrifuge methods. They differ in the measurement techniques and experimental setups. Generally the invading fluid is injected at increasing pressures (mercury method and porous-plate method) or increasing spin rates of a centrifuge (centrifuge methods) and the fluid production recorded. Fluid saturation data are easily retrieved and capillary pressure curves derived. A detailed review of these methods is given by Christiansen (2008).

An alternative approach to analytical solutions that allows to derive relative permeability and capillary pressure curves from a single experiment is the *history matching* technique. Experimental results are compared to those obtained with

[2]Breakthrough denotes the first appearance of the injected fluid at the outlet section of the sample.

numerical one-dimensional simulations carried out in samples with identical characteristics in terms of dimension, porosity and absolute permeability. Basically, a prescribed cost function is minimized to match the experimental data with those predicted by a two-phase core flow simulator designed to simulate SCAL experiments (Loeve et al., 2011). This data processing technique is very sensitive to the boundary conditions chosen for the history match and does not assure the uniqueness of the solution (Tavassoli et al., 2005). Several models can be adopted for history matching, each differs from the others essentially for the optimization and parametrization technique.

Chapter 2

Experimental methods and analysis techniques

Two-phase displacement processes in porous and permeable rocks are important in a number of petroleum engineering applications. Macroscopic properties (e.g. relative permeability and capillary pressure) of the reservoir rock can be measured either by laboratory experiments on large diameter cores (core-flooding) or by pore scale studies. Standard protocols for the characterization of the hydraulic properties of reservoir rocks prescribe to use brine (solution of water and salt) and oil as representatives of fluids present in real situations (Christiansen, 2008).

In the past, a popular approach used to predict absolute and relative permeability consisted in modeling the porous media as networks of pores and throats and to solve the associated hydraulic network (Bakke and Øren, 1997). However the advent of affordable high resolution X-ray computed tomography (X-CT) systems and the development of image analysis tools allow to access the full morphology of the pore-space with micrometric resolution.

In most cases the fluid motion is too fast and the changing morphology of the advancing front is difficult to be caught by means of micro CT machines, even though new solutions have been developed for CO_2/brine systems (Andrew et al., 2014b; Roels et al., 2014). Conversely, synchrotron-based X-ray systems are able to time resolve dynamic phenomena (Herring et al., 2014; Berg et al., 2014), due to their high photon flux and fast radiographic image acquisition, but remain an infrastructure of difficult access for this kind of experiments. When micrometric resolution is not required, *GANTRY*-based *medical* scanners can be used. Due to their higher frame rate, medical scanners are suitable to follow slowly evolving core-flooding phenomena (Vinegar and Wellington, 1987; Zhang et al., 2014).

Neutron transmission radiography (NTR) is another alternative to X-ray radiography. Since X-rays and neutrons interact differently with matter, the two radiation modalities are complementary. X-rays fail transmission through large core samples

but offer very high resolution on small samples. The neutrons are capable to image light elements (i.e. with low atomic numbers) such as hydrogen, water, carbon etc. and are little attenuated by the bearing minerals. The neutrons interact with the nucleus rather than with the electron shell. Thus, in principle, neutrons are well suited for the specific application we dealt with in this work (water-CO_2 and water-oil displacements) but their production at the petro-physical laboratory site remains a major limitation. Indeed, neutron imaging beamlines are traditionally installed at reactor facilities sites (Murison et al., 2015; Perfect et al., 2014). Recent advances in detecting systems allow high resolution. Voxel size of 11.8 μm were reported by Murison et al. (2015).

In the context of radiographic imaging applied to the visualization of the movement of fluids in rocks, magnetic resonance imaging (MRI) has been also employed (Chen et al., 2002). However MR techniques are more costly than a simple X-ray source/detector pair and subject to significant limitations in spatial resolution (Mitchell et al., 2013) and by the presence of iron (e.g. often consisting of small pyrite inclusions) in the solid matrix (Hall et al., 1997).

Among the imagining techniques, the X-CT is the most easily accessible, with good penetrating capability, highest spatial resolution and thus it is the most suited for the morphological characterization of porous media samples with micrometric pore sizes.

In this chapter the usefulness of a combined integration of coreflooding, X-CT and image analysis will be demonstrated. Specifically, the present study takes advantage of some underestimated capabilities of X-ray tomography systems in providing direct informations about the object being inspected through the acquired local attenuation maps. The main steps of this work are the following:

(i) Water-CO_2 and oil-brine displacements are performed in laboratory and continuously observed and recorded by means of fast X-ray radiographic projections.

(ii) The recorded images are processed and the fluid saturation profiles are derived.

(iii) Profiles describing the time evolution of the water and oil saturation within the core are used for an automatic history-match procedure that tunes the parameters of a relative permeability and capillary pressure model.

(iv) The volume reconstructed by processing the set of radiographic projections of the dry core sample is investigated for quantitative morphological measurements (porosity, pore size distribution).

2.1 X-ray radiography

2.1.1 Introduction

X-ray radiography is a non-destructive tool employed in investigation of non-trasparent materials, such as porous rocks. It provides planar images that map the variation of X-ray attenuation within an object.

The radiographic principle is conceptually simple: X-rays traverse a cross section of the sample along straight lines, the intensity of the attenuated X-ray signal emerging is converted by a scintillator into light and recorded as a digital image. The X-ray attenuation obeys the Beer-Lambert law (2.1) that states that there is a logarithmic dependence between the transmission of a ray through an object and the distance it travels:

$$\ln\left(\frac{I_0}{I_i}\right) = \int_L \mu\left(l, E\right)\, \mathrm{d}l \tag{2.1}$$

where μ is the local linear attenuation coefficient of the material in cm^{-1}, I_0 is the intensity of the incident impinging X-ray beam, I_i is the intensity emerging from the object (i.e. the *expected* detector intensity at the $i-th$ pixel of the recorded radiographic image) and L is the material thickness, namely the distance travelled. The un-attenuated incident intensity I_0 is read on the so called flat-field that is the radiography taken without sample before starting an acquisition. Hereafter the pixel index will be neglected, for brevity.

The logarithm of the intensity ratio is also referred to as projection. It contains an integral (through the length travelled in the material) information about the attenuation properties encountered by the ray. This datum should be de-convoluted to extract informations about the local internal morphology of the inspected object.

The linear attenuation coefficient μ of a material is a function of the photon energy E and, more specifically, can be expressed as follows:

$$\mu = \rho\left(a + b\frac{Z_e^{3.8}}{E^{3.2}}\right) \tag{2.2}$$

where ρ is the bulk density of the material, Z_e the effective atomic number of the material, a and b energy-dependent coefficients.

Today the micrometric resolution, that is normally obtained at the tomographic beam-lines of synchrotron facilities, is achievable with micro- and nano-CT laboratory tomographic machines based on open-type cone-beam tubes. These tubes can focus the X-ray beam to less than 1 micron spot size and allow the production of a Bremsstrahlung (i.e. polychromatic and incoherent) X-ray beam, suitable for micrometric spatial resolution tomography in a millimetric sized sample.

A typical X-ray tomography station is made up of three main hardware components: a X-ray polychromatic source, a planar digital detector (either CCD- or

CMOS- arrays or flat panels are used to capture intensity data after X-ray to visible light conversion on a scintillator) and a high-precision rotating stage.

2.1.2 X-ray radiographic set-up

The experimental setup employed in the specific application has been constructed in the Petroleum Engineering laboratory at the Delft University of Technology. A benchtop X-ray CT scanner is used to inspect a *still* sample undergoing continuous flooding. The experimental procedure will be detailily described in Section 2.1.4.

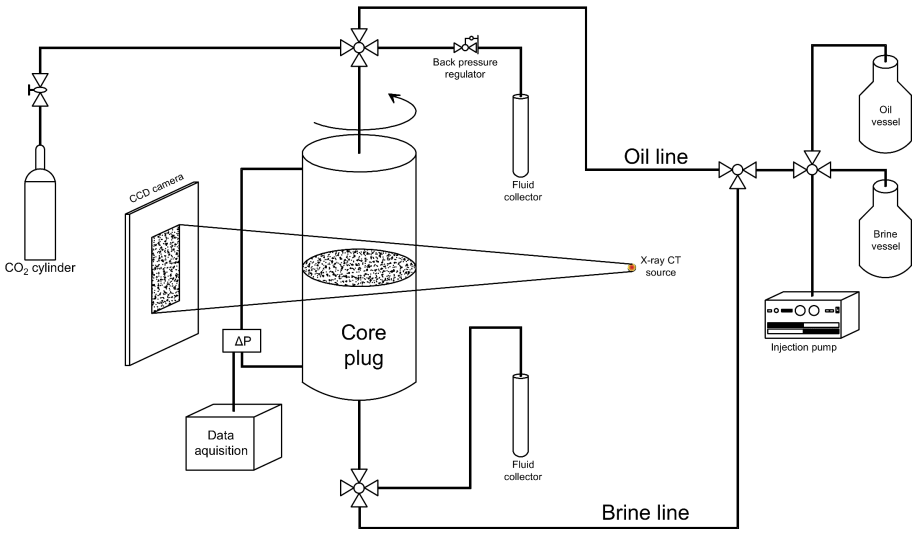

Figure 2.1: Schematic drawing of the experimental setup.

The schematic drawing of the radiographic system is sketched in Figure 2.1. It includes a high precision Harvard Apparatus Phd-Ultra® positive-displacement type pump, suitable for feeding the sample at an injection rate ranging from 0.0001 μl/hr to 220 ml/min. The hydraulic system is endowed with thin and flexible tubes of diameter 1.587 mm.

In order to minimize the adverse effects of core repositioning during the tests, the pumping apparatus is entirely assembled inside the X-ray shielded CT cabinet. A picture of the CT cabinet, whereof the laboratory is equipped, is shown in Figure 2.2. The external flow lines are arranged to prevent them to get into the field of view of the detector during image acquisition.

The specimen is radiographed with the nanofocus cone-beam CT from Phoenix |X-ray® (nanotom). The minimum achievable focal spot size (500 nm) of the open-type X-ray source allows for high resolution tomographic images. The X-ray detector

is a large area Hamamatsu 16 bit flat panel sensor (C7942SK-25) with 2304 × 2304 pixels (120 × 120 mm), pixel size 50 μm. It can operate in a 2 × 2 or 4 × 4 binning mode thus lowering resolution but allowing faster image readout. The open-type nanofocus X-ray source uses a tungsten target and is operated at 70 kVp and 170 μA, furnishing a power of 11.9 W. The nominal radiographic resolution is 7 μm.

Figure 2.2: CT cabinet from Phoenix |X-ray® (nanotom).

2.1.3 Radiography of fluid flow in rocks

Recently, X-ray radiography technique has been applied to visualize porosity and equilibrium fluid distribution in limestone rocks (Cadoret et al., 1995), to track fluid flow in packed beds (Gupta et al., 1997), to map the concentration of a tracer during a diffusion test (Tidwell et al., 2000) and to measure the change in water content during a moisture process in homogeneous and heterogeneous fractured materials (Roels and Carmeliet, 2006).

Here X-ray radiography is used to sample the moving phase interface in a sequence of brine-CO_2 and oil-brine displacements performed on a Bentheimer sandstone plug. Radiographic images of the static dry core are taken and averaged. Temporal sequences of radiographies are acquired for the sample undergoing primary imbibition (brine-saturation) and subsequently primary drainage. A method is proposed to compute two dimensional instantaneous saturation distributions from the radiographic sequence.

When the displacement through the rock plug is pressure-driven, the sample must be coated by glue to prevent leakages and inserted in a core-holder for a firm

and accurate positioning. The rock plug is coated with 2 thin layers of glue, obtained mixing resin (RENCAST CW 2215) and hardener (REN HY 5160); the first layer is very thin, in order to accelerate the glue drying and avoiding resin penetration into the pores and possible occlusions. The core-holder, designed and devised in the Petroleum Engineering laboratory at the Delft University of Technology, is made by Peek (polyether ether ketone).

For the specific application, Eq. (2.1) is written as:

$$\log\left(\frac{I_0}{I}\right) = \mu_H l_H + \mu_V l_V + \mu_R l_R + \mu_B l_B + \mu_O l_O \tag{2.3}$$

where the sub-scripts of the average linear attenuation coefficients identify the sealing material of the core Holder and the glue, the pore Voids, the Rock and the fluids (Brine and Oil) occupying the pore spaces.

The attenuation due to the core holder and the glue is known; thus the recorded intensity is corrected by the multiplicative term $\exp(\mu_H l_H)$. The attenuation of the void pore space is negligible.

The *measured* projection of a dry plug is:

$$\log\left(\frac{I_0}{I_{DRY}}\right) = \mu_R l_R \tag{2.4}$$

where l_R is the total thickness of the rock. The noise on I_{DRY} is mitigated by frame averaging.

For a dry plug undergoing imbibition that is radiographed still in the same position previously used for imaging the dry rock, the following system of equations can be written:

$$\begin{pmatrix} \mu_R & 0 \\ \mu_R & \mu_B \end{pmatrix} \begin{pmatrix} l_R \\ l_B \end{pmatrix} = \begin{pmatrix} \log\left(\frac{I_0}{I_{DRY}}\right) \\ \log\left(\frac{I_0}{I_{IMB}}\right) \end{pmatrix} \tag{2.5}$$

thus:

$$l_B = \frac{\log(\frac{I_{DRY}}{I_{IMB}})}{\mu_B} \tag{2.6}$$

The local saturation in the imbibition displacement is $S_B = l_B/l_V$, where l_B is the computed brine length, l_V is the local thickness of the pore space. The distribution of l_V can be measured from the radiography of a fully-saturated sample, for which $S_B = 1$ and $l_B = l_V$.

Subsequently the brine saturated rock undergoes a drainage process where oil is injected to displace the brine. The local accumulated thickness of brine, l_B, can be derived from

$$\log\left(\frac{I_0}{I_{O\&B}}\right) - \mu_R l_R = \mu_B l_B + \mu_O \left(l_V - l_B\right) \tag{2.7}$$

The oil saturation is $S_O = (1 - S_B) = l_O/l_V$. Repeating this process at each pixel position allows computing the saturation profile.

Assuming an axisymmetric sample and an axisymmetric distribution of fluids (i.e. no asymmetry due to, e.g. fluid *fingering*), a single projection carries the entire information of the sinogram that can be adopted to reconstruct a two dimensional (axial symmetric) slice via filtered back projection (FBP) (Baruchel et al., 2000). This assumption is not applicable to the present configuration, since the rock plug is inherently heterogeneous and fluid saturations are unevenly distributed.

The average linear attenuation coefficients of all the materials involved in the experiments have been measured individually with the CT scanner, at the same X-ray tube energy value as the one set for the radiographic experiments. In addition the materials have been tomographed with a Siemens medical scanner available in the Department of Geoscience and Engineering at the Delft University of Technology and the attenuation measured.

Table 2.1: Average attenuation properties of the scanned materials.

Material	Attenuation coeff. $[\mathrm{cm}^{-1}]$	Attenuation coeff. [HU]	Density $\left[\mathrm{kg/m}^3\right]$
Air/CO_2	0	-1000	1.225
Plexi	0.221	154	1180.3
Peek	0.238	241	1320.1
Oil	0.146	-240	773.5
Brine 1% KI	0.229	194	1005.6
Brine 3% KI	0.292	522	1020.3
Brine 4% KI	0.318	657	1027.8
Brine 5% KI	0.347	809	1034.5
Brine 10% KI	0.439	1288	1075.7
Rock	0.532	1771	2655

The attenuation values at 70 kVp and the densities of all the materials are summarized in Table 2.1. As reported by Kak and Slanley (1998), the linear attenuation coefficient values typically recorded by commercial (medical) CT systems are integers ranging from -1000 to 3000. This range refers to an international standard scale called the Hounsfield Scale, with a Hounsfield Unit HU defined as:

$$\mathrm{HU} = \frac{(\mu - \mu_w)}{\mu_w} \times 1000 \tag{2.8}$$

where μ_w is the attenuation coefficient of water. The value of HU = 0 corresponds to water and HU = -1000 is assumed to correspond to air (assuming $\mu_{air} = 0$).

Brine used in the experiments is a solution of water doped with potassium iodide (KI). Different salt concentrations have been tested and the corresponding brines tomographed. In Figure 2.3 a grey-scale radiography acquired with the medical scanner shows the average linear attenuation map of some of the materials used in the tests. Light greys correspond to high-attenuating materials, dark greys to low-attenuating materials. It appears evident how attenuation properties of 10 wt% KI doped brine can be compared to those of the rock sample, thus unsuitable to ensure enough phase contrast in the recorded images.

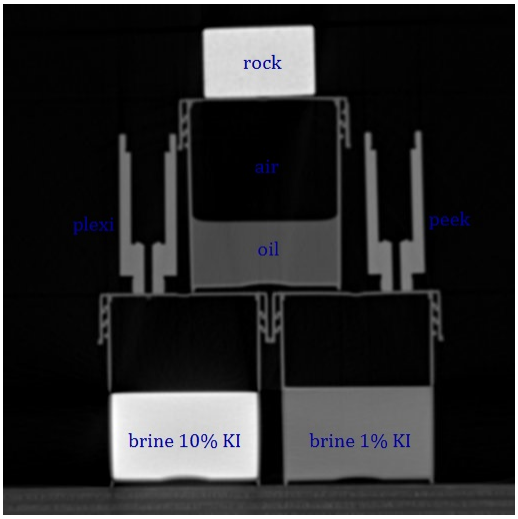

Figure 2.3: Map of average linear attenuation coefficients for some of the materials reported in Table 2.1.

2.1.4 Experimental procedure

Experiments are carried out following the protocol dictated for *unsteady-state* displacements in rock plugs and commonly adopted in petroleum engineering laboratories. All tests are performed on a cylindrical Bentheimer sandstone plug, SAMPLE 1 henceforth, (D = 9.45 mm, L = 30.71 mm), extracted from a bigger block. The analyzed sample is shown in Figure 2.4. The specific sandstone has been studied by Roels et al. (2014) and its physical and electrical transport properties are reported by Peksa et al. (2015). A complete mineralogical characterization of the rock, determined from X-ray diffraction (XRD) and X-ray fluorescence (XRF) measurements, is reported by van Hemert et al. (2013) and reveals that quartz, orthoclase and

kaolinite are the main constituents of the rock. The average porosity derived from image analysis of radiographic acquisitions is $\phi \approx 0.23$ (see Section 2.2.1 for details). The experimental absolute permeability k is about 3.2 Darcy.

Figure 2.4: Glue-coated Bentheimer sandstone sample (SAMPLE 1).

The experimental procedure consists in the following steps:

1. CO_2 is injected for at least 30 minutes to displace all the air trapped in the piping system and in the rock plug.

2. Brine is injected into the sample from the bottom section to the top section, for 50 PV until total saturation is achieved. The initial injection flow rate is 0.2 ml/min and produces an interstitial velocity of 0.02 cm/s. The corresponding pore Reynolds number Re_p for imbibition is 1.5×10^{-4}. During imbibition, a "back pressure" of 25 bar is mantained for almost 25 minutes, this ensures that even the smallest amount of CO_2 dissolves in brine solution. Further experimental tests performed on plugs of the same rock demonstrate that a complete brine saturation can be attained as long as injection flow rate is low and injected volume is at least 50 PV.

3. At $S_B = 1$ the rock sample is brine-flooded at stair-wise increasing and decreasing flow rates and the absolute permeability k is estimated with a standard permeability test (Figure 2.5).

4. Oil is injected downward, from the top section to the bottom section, in order to guarantee gravity stable displacement until the pressure drop across the sample is constant. The injection flow rate is 0.2 ml/min. The corresponding pore Reynolds number Re_p for drainage is 4.2×10^{-5}.

Operative absolute pressure and pressure drop are continuously measured using range-selective pressure transducers. Brine adopted for brine/CO_2 displacement (imbibition) is a solution of water doped with 4 wt% of KI. This concentration allows the best image contrast between the fluids and fluids and sandstone. The dynamic viscosity γ_B at $20°C$ is 1.203 $\times 10^{-3}$ Pa $\cdot$ s. The representative oil adopted for oil/brine (drainage) displacement is hexadecane ($C_{16}H_{34}$) 99% in purity. The dynamic viscosity γ_H at $20°C$ is 3.205 $\times$ 10^{-3} Pa $\cdot$ s. The pore Reynolds number, based on the square root of the measured absolute permeability ($Re_p \equiv v_D \sqrt{k}/\nu_f$), is chosen in order to investigate the validity of Darcy flow regime, where v_D is the Darcy's velocity, $\nu_f = \gamma_f/\rho_f$ is the kinematic viscosity of the injected fluid.

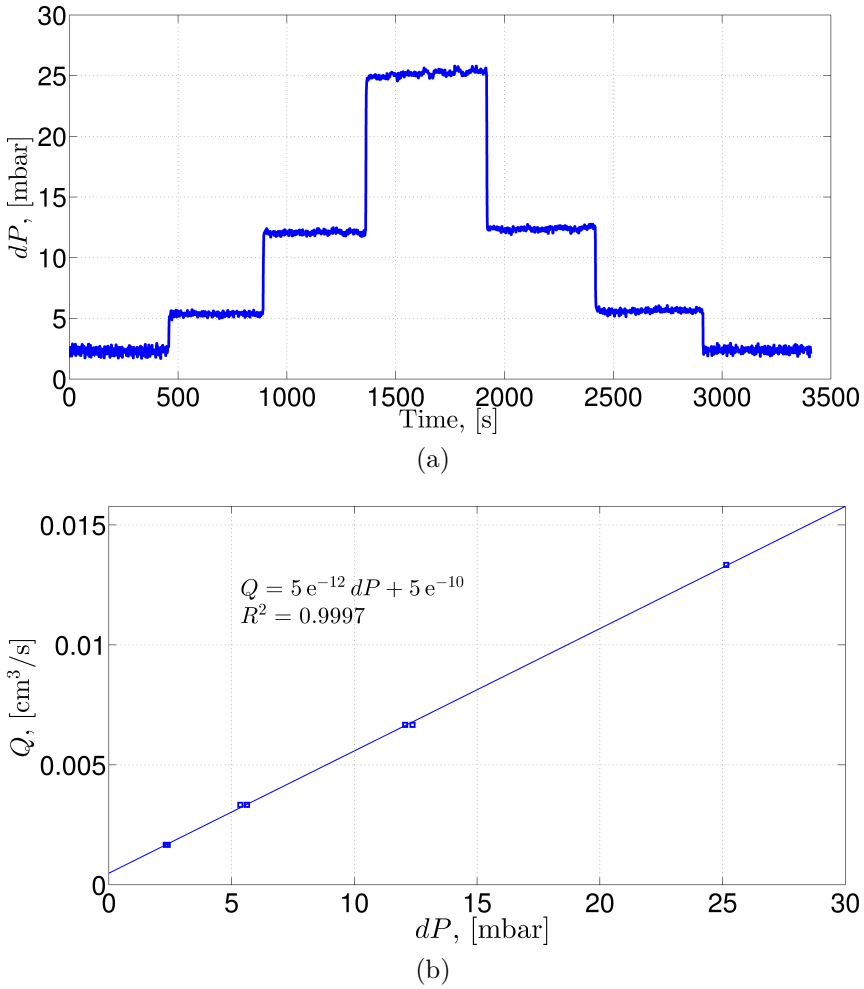

Figure 2.5: (a) Permeability test at $S_B = 1$: recorded pressure drop dP during brine injection. (b) Estimation of k: relation between injection flow rate Q and recorded pressure drop dP.

2.2 Results

2.2.1 Porosity distribution

The two-dimensional porosity distribution, figure 2.6(a), is calculated as $l_V/(l_R+l_V)$, where l_R and l_V are obtained, respectively, from the radiography of the dry and brine-saturated core sample. A mean value of $\phi \approx 0.23$ is computed, in remarkable agreeement with measurements reported elsewhere, i.e., $\phi = 0.2467$ (van Hemert et al., 2013) and $\phi = 0.24$ (Roels et al., 2014). The porosity variation along the axis of the sample is reported in Figure 2.6(b): in principle, this information can be used to account for material non-homogeneity in the history-match process. Nordtvedt et al. (1999) demonstrate the significant effect of violating the homogeneity assumption on the determination of the relative permeabilities and residual oil saturation via a history-match approach. The porosity profile in Figure 2.6(b) is a row-averaged porosity, any local inhomogeneity and geometric distorsion due to the x-ray traversed path length are smoothed.

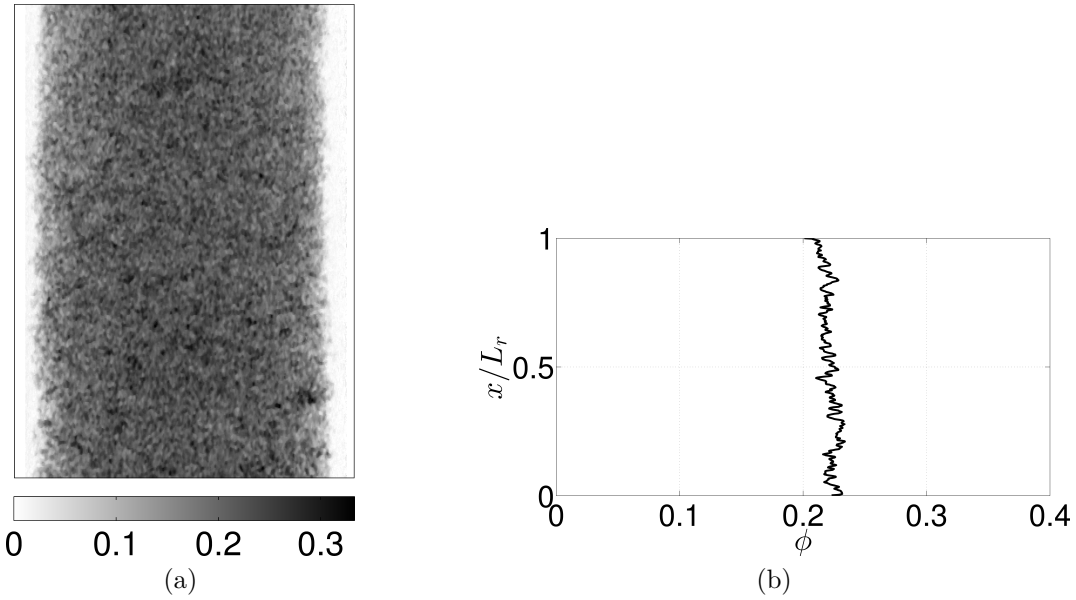

Figure 2.6: (a) Local, two-dimensional porosity distribution $\phi = l_V/(l_R + l_V)$ (see Eq. (2.6) with $S_B = 1$) obtained from the dry sample radiography. (b) Porosity profile along the sample's axis.

2.2.2 Primary imbibition

A sequence of radiographic images is acquired during primary imbibition. The rising brine interface is barely recognizable in radiographic modality and unsuitable for image segmentation. On the contrary, in the associated brine saturation images obtained resorting to Eq. (2.5) and Eq. (2.6), the upward-advancing brine interface can be clearly seen as shown in Figure 2.7(a,c,e).

The corresponding saturation profiles are also visualized in Figure 2.7(b,d,f). The row-averaged saturation values are plotted versus the non-dimensional length of the core. L_r is the portion of the core length in the field of view of the detector.

The mobility ratio $M = \gamma_{inv}/\gamma_{def}$ is 81.8, the capillary number $Ca = (\gamma_{inv} v_{inv})/\sigma$ is 1.5×10^{-6}, where the subscripts *inv* and *def* stand for invading and defending fluid, respectively.

According to Lenormand's observations (Lenormand et al., 1988) the displacement occurs in transition regime. A plug flow-like front can be observed at the interface between invading and defending fluids (brine/CO_2), due to the high mobility of the brine phase. The pattern presents a nearly flat front and some irregularities could be observed at the scale of a few pores.

2.2.3 Primary drainage

Once it is completely saturated with brine, the sample is drained by injecting oil from the top section to the bottom section and a new set of radiographic images is taken during the displacement. The oil saturation values are calculated from Eq. (2.7). A sequence of three oil saturation images is reported in Figure 2.8(a,c,e) and the corresponding oil saturation profiles are reported in Figure 2.8(b,d,f). The mobility ratio M is 2.66, while the capillary number Ca is 3.98×10^{-6}. According to Lenormand, the displacement occurs in transition regime close to capillary fingering. Indeed the interface appears more irregular and indented, if compared to the advancing front during imbibition.

Time elapsed between two subsequent radiographic aquisitions $\Delta t = 23$ s, average porosity ϕ and sectional area A of the sample are used to validate the saturation profiles. At recording times t_1 (Figure 2.8(a)) and t_2 (Figure 2.8(c)) the oil front has not yet reached the outlet section of the tomographed region. Thus, the amount of oil injected in the time interval $\Delta t = t_2 - t_1$ must be equal to the oil accumulated within that region in Δt:

$$V_{\mathrm{O,inj}}{}^{(t_2)} - V_{\mathrm{O,inj}}{}^{(t_1)} = Q_O \cdot \Delta t = A\,\phi \int_0^{L_r} \left(S_O^{t_2} - S_O^{t_1}\right) \mathrm{d}x \tag{2.9}$$

The oil flow rate Q_O imposed at the metering pump matches that computed by the time sequence of saturation profiles $S_O^{t_1}$ and $S_O^{t_2}$.

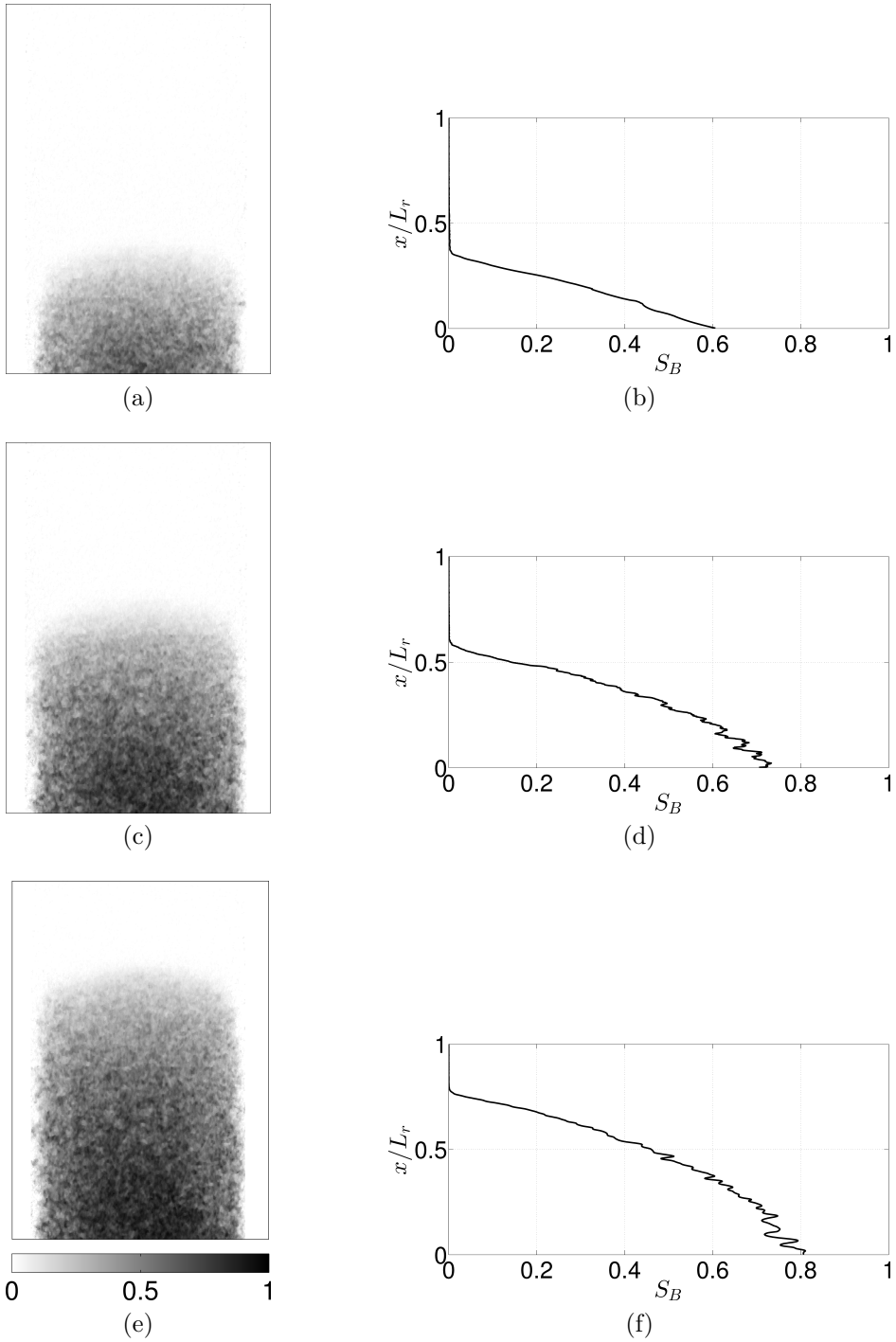

Figure 2.7: Brine saturation calculated from the radiographic images during brine injection (a,c,e) and corresponding brine saturation profiles (b,d,f) at different recording times.

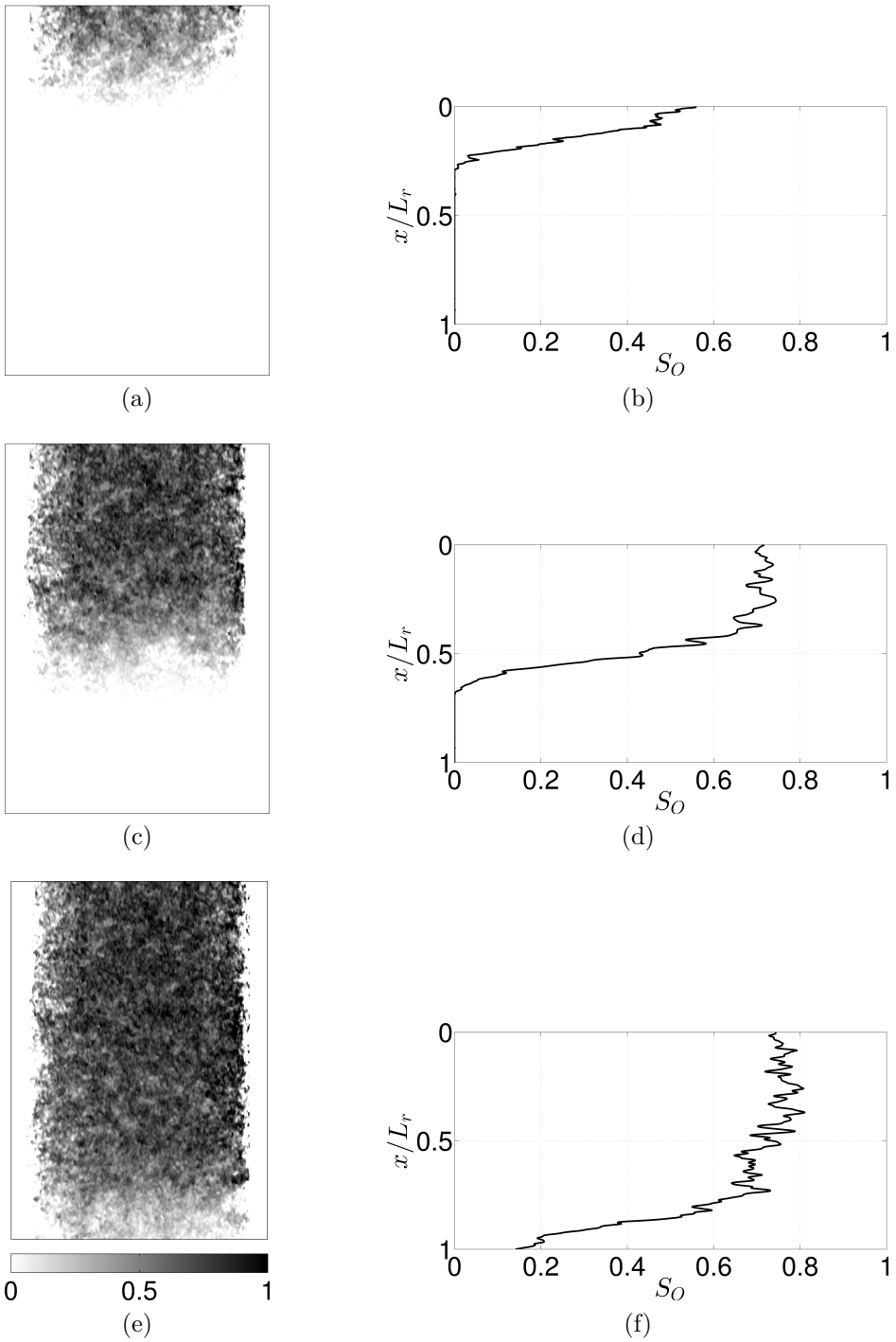

Figure 2.8: Oil saturation calculated from the radiographic images during oil injection (a,c,e) and corresponding oil saturation profiles (b,d,f) at different recording times.

2.2.4 History matching

The characterization of the hydraulic properties of the sandstone sample for the primary drainage process is achieved with a history matching process where the best fitting is sought for, between the experimental saturation profiles derived by radiography and the corresponding simulated profiles. The relative permeability k_r and capillary pressure P_c curves are estimated by simulating the drainage process using a one-dimensional, finite-difference model (Christiansen, 2008). The model assumes that the sample is both isotropic and homogeneous.

The algorithm consists in solving pressure and saturation differential equations for one of the two phases (say the invading oil phase). Here an implicit pressure and explicit saturation (IMPES) approach is used to solve the mass balance equations for saturation profile.

The dependence of relative permeability on brine saturation S_B is represented by the Corey (Brooks and Corey, 1966) model:

$$k_{r,B} = k_{r,B}^{max} \left(\frac{S_B - S_{B,i}}{1 - S_{O,r} - S_{B,i}} \right)^{n_B} \tag{2.10}$$

$$k_{r,O} = k_{r,O}^{max} \left(\frac{1 - S_B - S_{O,r}}{1 - S_{O,r} - S_{B,i}} \right)^{n_O} \tag{2.11}$$

where $k_{r,O}$ and $k_{r,B}$ are the oil and brine relative permeabilities, $k_{r,O}^{max}$ and $k_{r,B}^{max}$ the permeabilities at maximum oil and brine saturations, respectively, $S_{O,r}$ and $S_{B,i}$ the residual oil saturation and the irreducible brine saturation, n_O and n_B *power-law* coefficients.

For the capillary pressure the Bentsen-Anli (Bentsen and Anli, 1977) model is used:

$$P_c = P_{c,t} + P_{c,s} \log \left(\frac{1 - S_{B,i}}{S_B - S_{B,i}} \right) \tag{2.12}$$

where $P_{c,t}$ and $P_{c,s}$ are denoted as *threshold* and *span* capillary pressures (Christiansen, 2008).

More general models could be used (Lomeland and Ebeltoft, 2008; Lomeland et al., 2005), where needed, to improve the correspondence between numerical and experimental data. Eight parameters, appearing in Eq. (2.10), (2.11) and (2.12), are considered as *free*, i.e., $k_{r,O}^{max}$, $k_{r,B}^{max}$, n_O, n_B, $P_{c,th}$, $P_{c,sp}$, $S_{O,r}$, $S_{B,r}$. Optimal values of the free parameters are determined, so as to minimize difference between three experimental (mean) saturation profiles and the corresponding simulated profiles, in least-squares sense. A constrained genetic algorithm (GA) optimization is used for this purpose (Goldberg, 2002). The following bounds are prescribed to the free parameters:

$$
\begin{array}{ccccc}
0.05 & \leq & S_{B,i} & \leq & 0.50 \\
0.05 & \leq & S_{O,r} & \leq & 0.50 \\
0.50 & \leq & n_B & \leq & 2.50 \\
0.50 & \leq & n_O & \leq & 2.50
\end{array}
\qquad
\begin{array}{ccccc}
0.05 & \leq & k_{r,B}^{max} & \leq & 1.00 \\
0.05 & \leq & k_{r,O}^{max} & \leq & 1.00 \\
0.00\,\text{psi} & \leq & P_{c,t} & \leq & 2.00\,\text{psi} \\
0.00\,\text{psi} & \leq & P_{c,s} & \leq & 2.00\,\text{psi}
\end{array}
$$

The relative permeability and capillary pressure curves resulting from the GA optimization are shown in Figure 2.9. The computed profiles that best fit the experimental profiles of brine saturation are shown in Figure 2.10. The spatial coordinate is normalized to the total length of the core L.

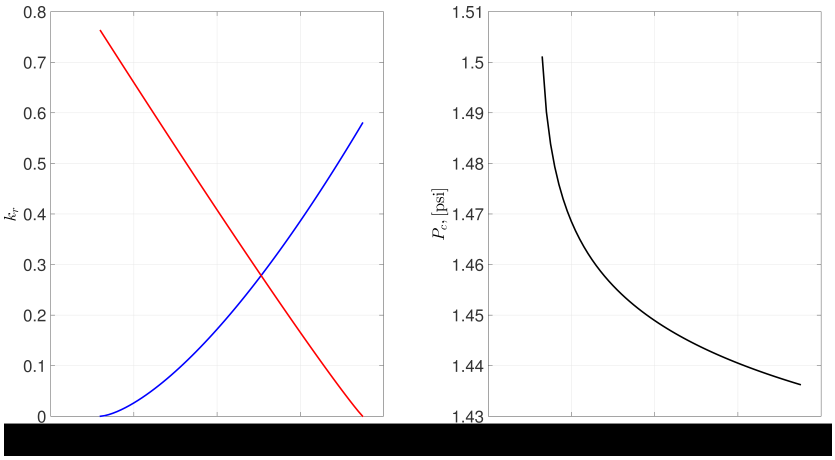

Figure 2.9: Relative permeability and capillary pressure curves for the drainage process. $k_{r,B}$ versus brine saturation is reported in blue, $k_{r,O}$ in red.

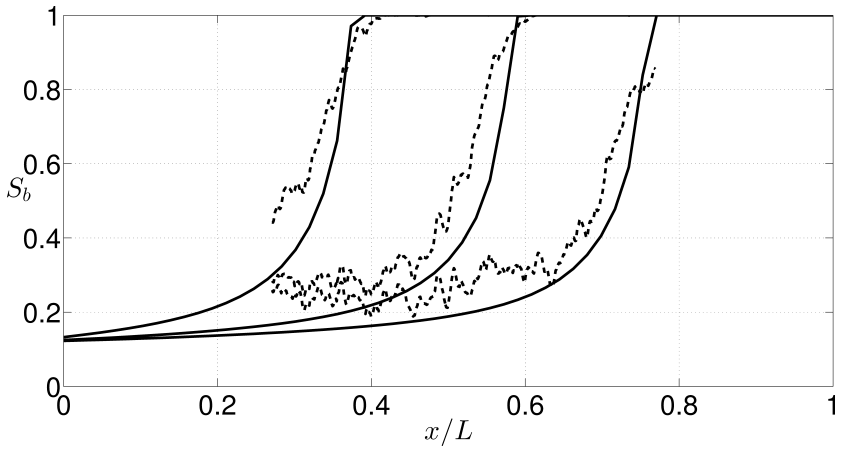

Figure 2.10: Comparison of numerical (continuous line) and experimental (dashed line) profiles of brine saturation for the drainage process.

2.3 X-ray computed tomography

Porous media are opaque to visible light which limits the characterization of their complex pore space often made up of stubby pores connected by narrower throats. The opacity also prevents the direct visualization of all the important phenomena related to the fluid flow in such a complex morphology. Millimetric samples of porous rocks are semi-transparent to hard X-ray (energies from about 12 to 120 keV) and the rock-pore density contrast is favourable to planar grey-scale images with high dynamic range.

As previously demonstrated, nowadays available X-ray tomographic systems allow for digital radiographies with micrometric planar resolution. Additionally, the simple recording of sequences of X-ray radiographic projections acquired with high frame-rate detectors during the evolving percolation process in an immobile sample, provides qualitative and quantitative informations about the object being inspected by means of attenuation maps. Two-dimensional porosity and fluid content maps can be derived from integral attenuation properties through the path length travelled by the X-rays. Nevertheless, the aggregate attenuation conveyed by the radiographic projection loses information about the third spatial dimension.

X-ray computed tomography (X-CT) retrieves the "lost" information, exploiting the radiographic principles discussed in section 2.1. In a full tomographic acquisition the specimen is placed on the stage and rotated by small angular steps and the radiographic operation is repeated at each step. A set of X-ray attenuation measurements at a fixed object position and system configuration is called *view*. Multiple sets of view over a range of angular orientations are made up of several hundreds of projections, depending on the diameter of the object, and allow a complete tomographic characterization of the sample.

The very high spatial resolution achievable with modern CT station make this technique suitable for reconstruction and inspection of porous media with micrometric pores and throats. Hence X-ray computed tomography (X-CT) has been used for long time in petrophysical laboratories for pore-space visualization and for related post processing including morphological measurements (Coles et al., 1998; Josh et al., 2012).

2.3.1 Image reconstruction

The reconstruction of an image from the acquired set of projections represents an inverse problem. The mathematical principle of CT reconstruction for parallel rays was developed early in the last century by Radon and Parks (2009). The Radon inverse recreates the map of the linear attenuation coefficients of the object cross-section from the collection of projections taken around it (i.e., from the *sinogram*). The process can be seen as a filtration of the projection in the Fourier domain (the projection is convolved with a high-pass filter) and a back projection into the

pixels of the image grid (each projection is superimposed over a square grid at the corresponding acquisition angle). The whole operation is often referred to as filtered back projection (FBP). The algorithm generalizing in 3D the Radon inverse for diverging cone-beams is due to Feldkamp et al. (1984) and is also cast around the original filtered back projection technique. The filtered back projection (FBP) is the most popular reconstruction method that efficiently computes the image of the internal structure of the sample in a single reconstruction step (Pan et al., 2009). The FBP is demanding in terms of data set for it requires a dense full angular coverage of the object with equal spaced projections but it is very fast when compared with iterative algebraic methods. The assumption of monochromatic radiation is made as if all the photons have the same energy, even though, strictly speaking, only a synchrotron generates monochromatic X-ray beam. Only a few research codes implement polychromatic reconstruction algorithms. They often use maximum likelihood minimization principle to fit the image under reconstruction to the projection data. The approach is computationally very demanding due to the optimization problem they solve (Elbakri and Fessler, 2003; Wu et al., 2014).

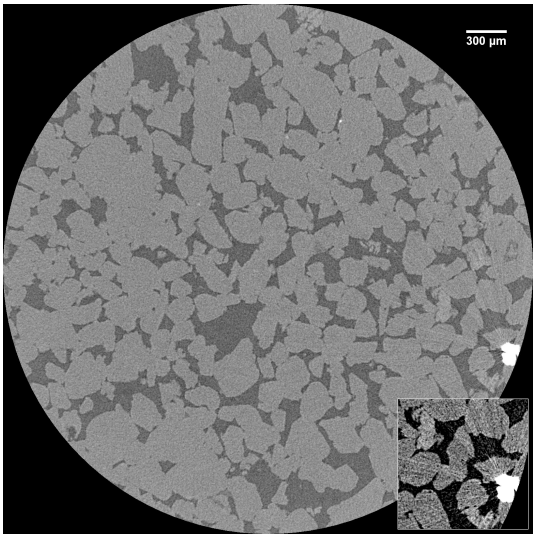

Figure 2.11: Streak artefact owing to pyrite inclusion and detail after contrast enhancement.

During the reconstruction process, the raw intensity data in the sinogram are converted to *CT numbers* or *CT values*, whose range is determined by the acquisition system. The image reconstruction proceeds slices by slices. The slice is a grey level image that cuts the object perpendicularly to the axis of the rotation stage. The grey level slices are stacked to form the tomographic volume from which sub-volumes of interest are extracted. The tomographic volume, named *digital volume*, consists in a three-dimensional grey level map of voxel luminosity. High attenuating

materials, e.g. the rock matrix, appear as brighter regions (high CT values), whereas low-attenuating materials, e.g the voids, appear as darker regions (low CT values). Fluids present in the pore space exhibit intermediate CT values.

Acquisition and reconstruction processes produce a series of artefacts (beam-hardening, ring artefacts, streak artefacts and partial-volume effects) which lead to unexpected CT values in the the reconstructed slice. Exhaustive explanation and interpretation of CT artefacts have been given by Ketcham and Carlson (2001); Wildenschild and Sheppard (2013); Jovanović et al. (2013). An example of streak artefact is shown in Figure 2.11. Brighter stripes are generated by photon scattering when impinging on the iron ore (pyrite) inclusion.

Most of the modern CT facilities have reconstruction programs that include algorithms specifically dedicated to artefacts reduction.

2.3.2 Example of a home-made X-ray tomography device

The X-ray micro-tomographic facility available at University of Bergamo is shown in Figure 2.12. The tomographic system is based on an open type Hamamatsu X-ray source 160 kVp. An Aerotech rotary air-bearing drive stage provides superior angular positioning and velocity stability.

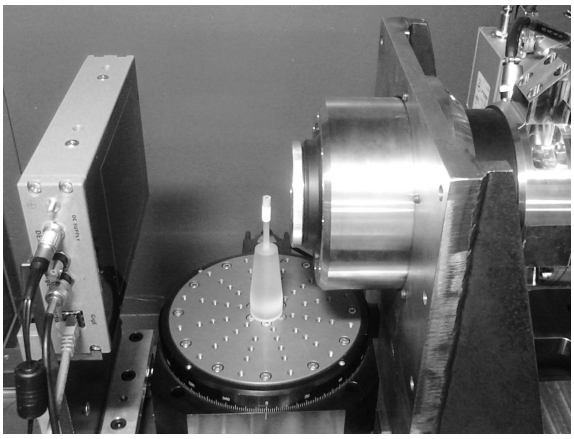

Figure 2.12: One-micron focal spot cone-beam source of the X-ray computed tomography system at University of Bergamo.

The X-ray projections are collected by a Dexela-Perkin Elmer 1512 flat panel Complementary Metal-Oxide-Semiconductor (CMOS) X-ray detector. The detector has a pixel size of 75 microns and allows binning. The frame rate is 30fps at full resolution. The cabinet has 5 mm of lead shielding. To mitigate the effect of the beam hardening on imaging a thin aluminium filter plate is used to filter low energy

X-rays exiting from the source. The commercial software VGStudio MAX from Volume Graphics GmbH (http://www.volumegraphics.com/en/) that includes beam-hardening correction is used for slice reconstruction and artefact reduction.

2.4 Image processing

2.4.1 Volume segmentation

The whole digital volume is treated with non-linear filters to mitigate the noise. The basic median filter with a $3 \times 3 \times 3$ kernel is a good candidate for removing noise whilst preserving edges. The algorithm underlying this filtering technique acts replacing the CT value of a voxel with the median value of the local neighbourhood (26 surrounding voxels). Edges are kept sharpen, as the new CT value is the value associated to an original voxel.

The segmentation of the gray-level voxel volume into a boolean three-dimensional matrix where the pore space and solid material are represented by 1 and 0 respectively is based on the histogram of the luminosity value of all the voxels. Peaks and valleys in the histogram are used to distinguish between solid and void (i.e. material and pore space). The segmentation threshold is placed in the valley. To minimize the effect of subjectivity, automated histogram-based segmentation algorithms exist, among which the Otsu's algorithm turned out to provide the most accurate results (Iassonov et al., 2009). Three-dimensional morphological functions are further applied to remove both buoyant isolated rock voxels floating within the pore space and unconnected pore voxels present in the solid matrix. Commercial and proprietary image analysis tools are used to filter, segment and binarize the digital volume to obtain the pore space mask.

The image processing workflow is sketched in Figure 2.13. Histograms of voxel luminosity of the un-filtered and filtered digital volumes are shown in Figure 2.14. Filtering has the effect to sharpen the peaks associated with each phase, making easier the threshold positioning.

Definitely, the segmentation process is non-trivial. The filtering may introduce biases on the results, since features enhancement in the treated volume entails unavoidably a loss of information (Iassonov et al., 2009). Additionally, any mislabelling of features occurring when assigning a voxel of the reconstructed volume to one or the other phase, could significantly affect subsequent pore space characterization and related measurements. Thus the accuracy of the whole procedure should be thoroughly evaluated to ensure that the resulting binary volume represents the "true" internal structure of the rock (Leu et al., 2014).

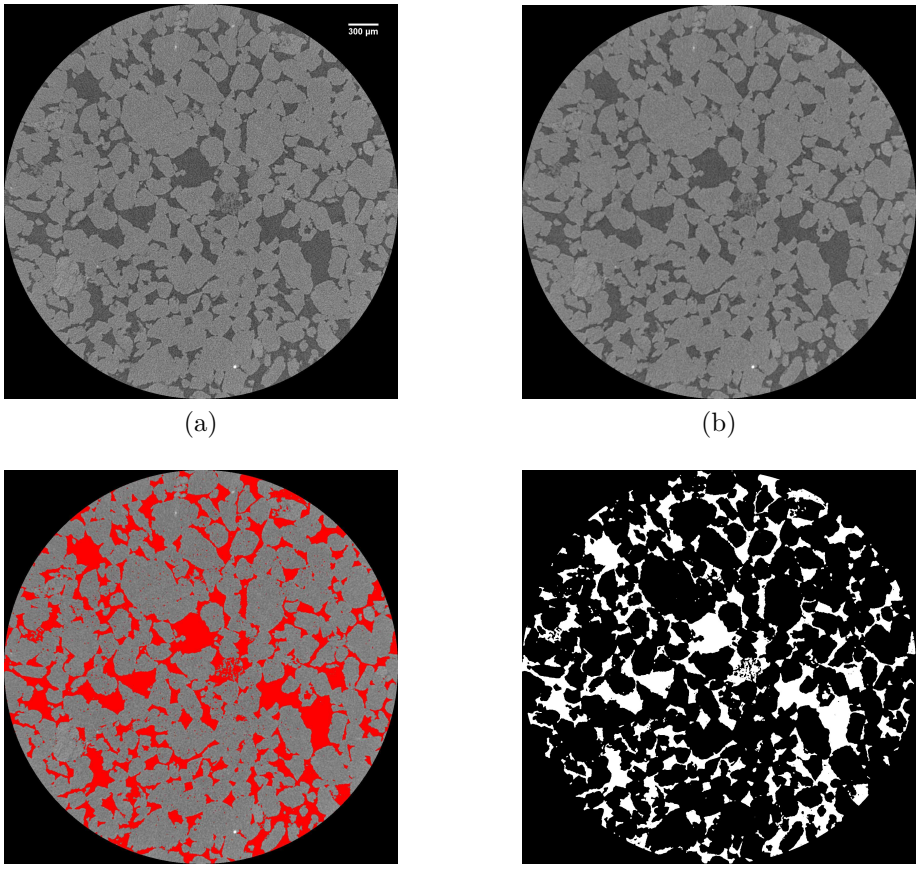

Figure 2.13: Image processing workflow. (a) Original un-filtered grey-scale slice. (b) Filtered grey-scale slice. (c) Segmented slice via Otsu's algorithm. (d) Binarized slice after outliers' removal.

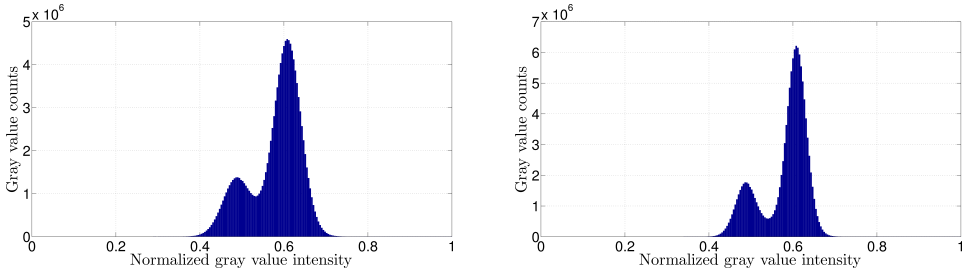

Figure 2.14: Histograms of voxel intensity of grey-scale un-filtered (a) and filtered (b) digital volumes.

2.4.2 Pore space characterization

The binary volume obtained from segmentation is suitable for pore space morphological measurements. Indeed, the newly identified porous domain consists of a set of cubic cells describing the pore system in an objective manner. Sub-volumes of interest are extracted from the stack of slices. An easy-to-estimate parameter is the average "three-dimensional" porosity $\bar{\phi}$, calculated as the ratio of the 1-voxels to the total number of voxels of the binary volume. The $\bar{\phi}$ value (0.236), calculated for a 1000 x 1000 x 1000 voxels^3 cube, is in excellent agreement with the radiographic results reported in Section 2.2.1.

In order to quantify the effect of sample size on porosity estimation a sensitivity analysis is conducted. The porosity is calculated for several cubic sub-volumes of different sizes as a function of the cube side length L_c in the range of L_c=[20 ÷ 600] voxels. In Figure 2.15, porosity variation across the sample (dashed blue line) and average porosity calculated from the first up to the current slice N_{cs} (dashed cyan line) are compared to $\bar{\phi}$ (dashed red line). Slice-by-slice porosity oscillates above and below the average value from about 0.18 to 0.27.

The percentage error $\epsilon_\phi\%$ in terms of absolute deviation between $\phi = f(L_c)$ and $\bar{\phi}$ is reported in Figure 2.16. As expected, the percentage error decreases as L_c increases. A 300 x 300 x 300 voxels^3 cube can be reasonably considered a good choice for REV. The selected volume is used for all morphological measurements.

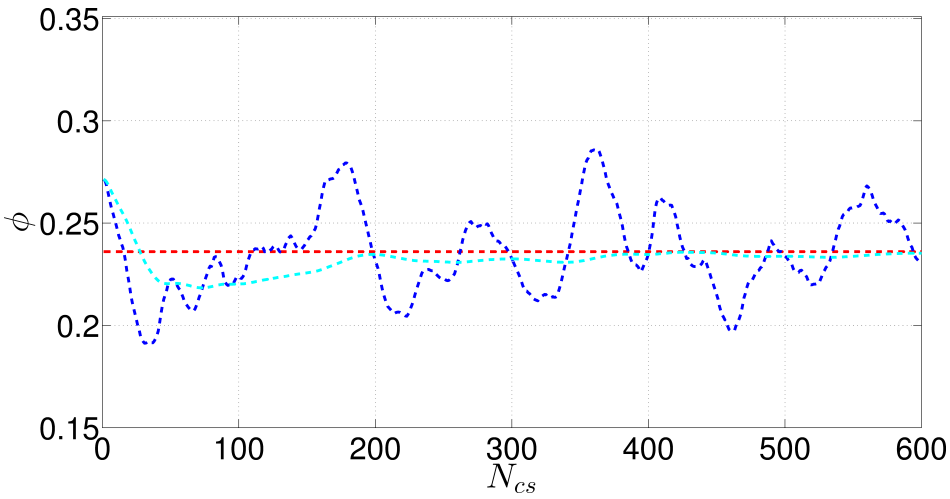

Figure 2.15: Slice-by-slice porosity (blue line) and average porosity up to the current slice N_{cs} (cyan line) compared to $\bar{\phi}$ (red line).

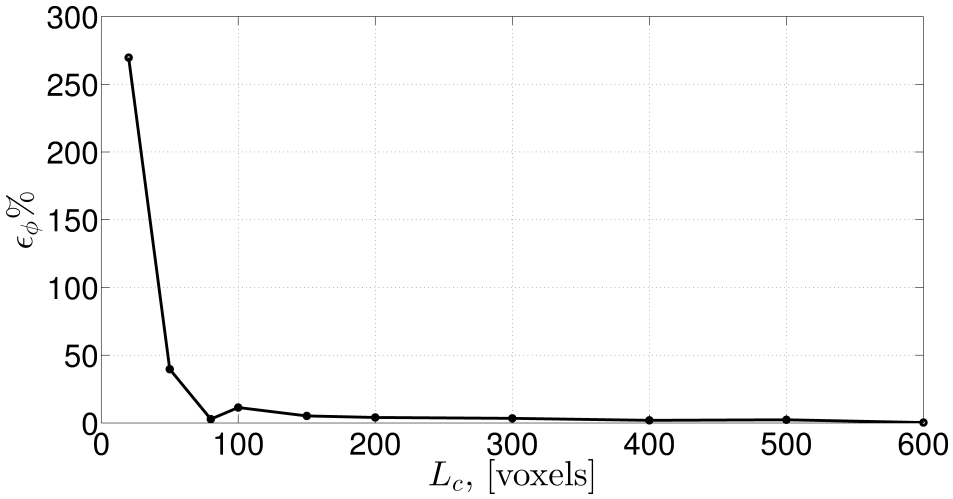

Figure 2.16: Percentage error on porosity estimation $\epsilon_\phi\%$ as a function of the cube side length L_c.

Figure 2.17(a) is a three-dimensional visualization of the digital volume of SAMPLE 1. The cube size length is 300 voxels. The voxel size is 2.5 μm. The isosurface representing the pore space walls is coloured in red. The material is shown as transparent grey, whereas the pores are left void. The pore space is often sub-divided into pore bodies that are relatively stubby and narrow ducts or throats connecting them. The individual pores are segmented with a proprietary code that exploits a distance-transform-based (DT) watershed algorithm. The standard 3D watershed-transform is a parameter-free technique used to resolve pores in an objective manner and takes inspiration from hydrology watershed theory. Firstly, the DT is applied to the binary volume. The DT map assigns to each voxel of the pore space the distance to the nearest solid voxel (i.e. the distance to the void/grain interface). According to the easier 2D topographic interpretation the DT gives the elevation (and $-$DT gives the deepness) of the topographic surface, the water placed on any pixel, enclosed by a common watershed line, flows downhill sliding on the steepest slope toward a common local intensity minima: pixels draining to a common minimum form a catchment basin, which represents the pore region. The watershed is the set of local intensity maxima pixels that separate the catchment basins and correspond to the pore throats. It is well known that the standard watershed suffers of severe over-segmentation. Here the pathology is successfully treated with a H-minima transform that suppresses all the local minima regions whose depth is less than a set scalar threshold. In order to accurately calculate three-dimensional gradients, used by the watershed method to identify local minima, the resolution of the original volume is magnified by a factor 3. The segmented pores are visualized in Figure 2.17(b). Pore-size distribution and histogram of the pore volumes are shown in Figure 2.18(a) and (b), respectively.

In Figure 2.19 the pore space isosurface and the segmented pores of a reservoir quartzose sandstone sample, SAMPLE 2 henceforth, are visualized. The cube side length is 200 voxels. The voxel size is 4.5 μm. Pore-size distribution and histogram of the pore volumes are shown in Figure 2.20. The statistics on the watershed-segmented pores of SAMPLE 1 and SAMPLE 2 are based on 320 and 352 pores, respectively.

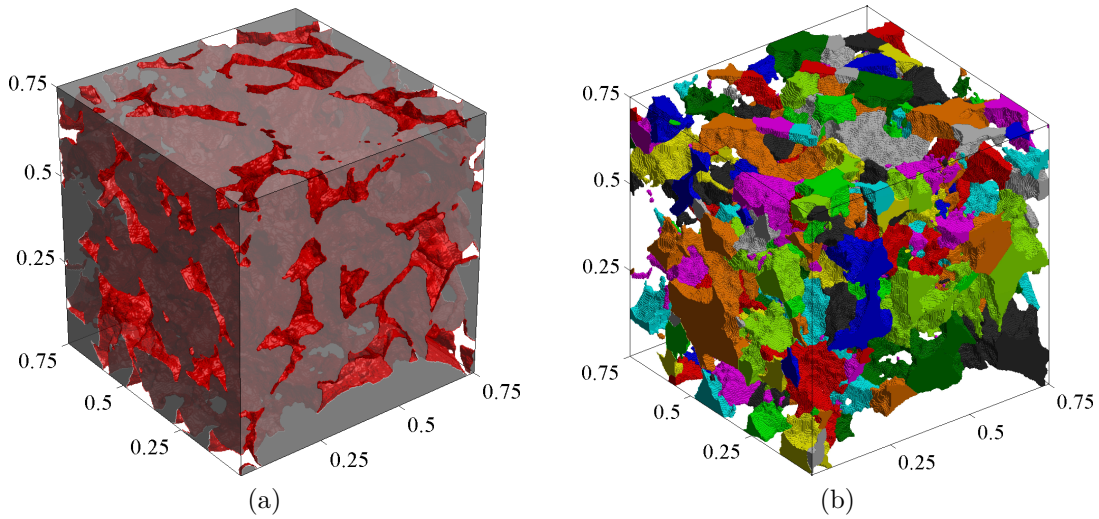

Figure 2.17: SAMPLE 1. Voxel size 2.5 μm. (a) Digital sample (pore space isosurface in red). (b) Segmented pore space. Lengths are expressed in millimetres.

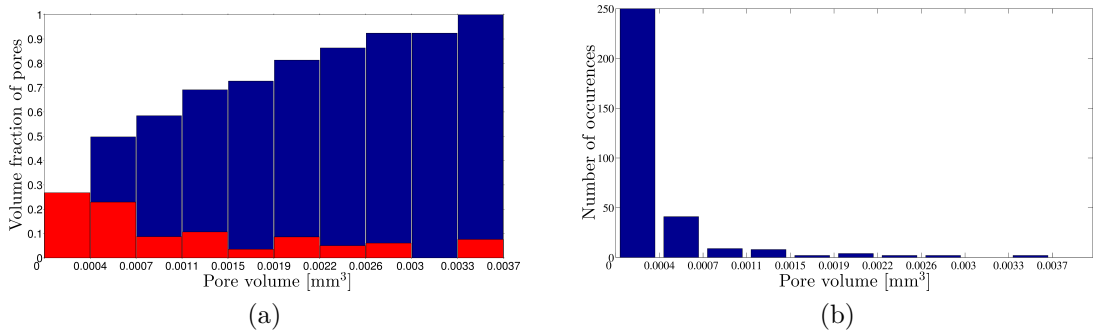

Figure 2.18: SAMPLE 1. (a) Pore-size distribution (red) and cumulative pore-size distribution (blue). (b) Histogram of the pore volumes.

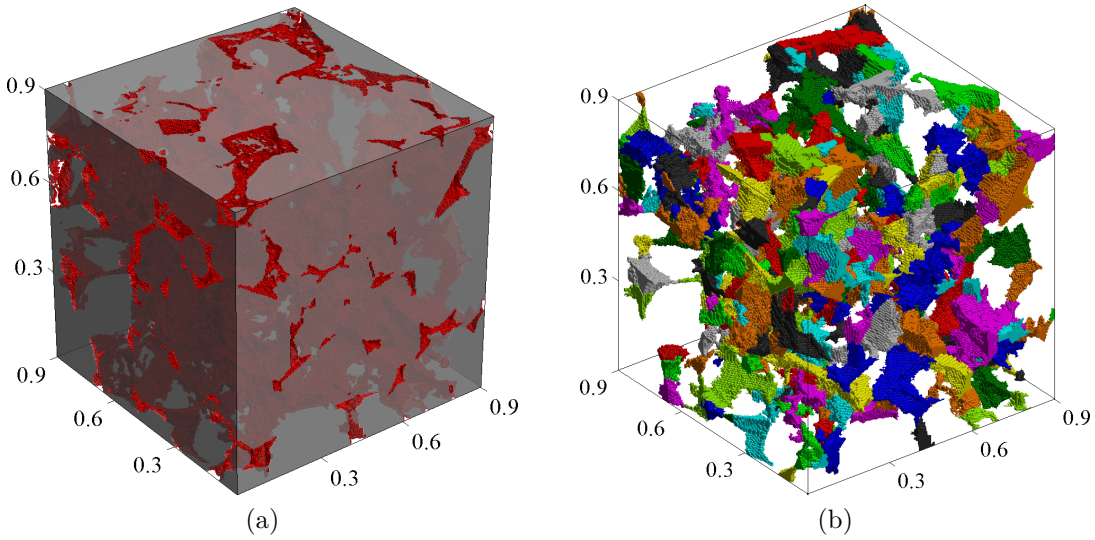

(a) (b)

Figure 2.19: SAMPLE 2. Voxel size 4.5 μm. (a) Digital sample (pore space isosurface in red). (b) Segmented pore space. Lengths are expressed in millimetres.

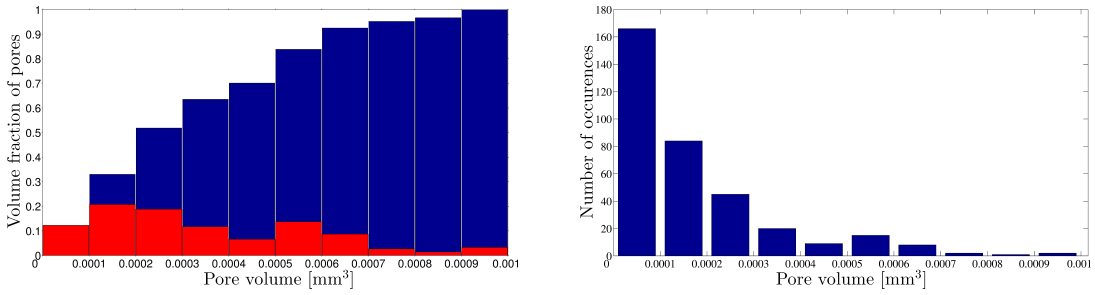

(a) (b)

Figure 2.20: SAMPLE 2. (a) Pore-size distribution (red) and cumulative pore-size distribution (blue). (b) Histogram of the pore volumes.

The pore space characterization suggests a significant difference in terms of porosity and pore-size distribution between the two sandstone samples. The former is characterized by a relatively high void fraction, the latter by a low void fraction. Specific surface area $a_{v,gr}$ and porosity ϕ are used to estimate the absolute permeability via Kozeny-Carman relation (see Eq. (1.4)). The Kozeny-Carman correlation

overestimates the experimental measurements for both the sandstone samples. This difference could be ascribed either to macroscopic inhomogeneities in the sample used in the experiments, or to inaccuracy in isosurface reconstruction, or to inadequacy of the digital domain as a representative elementary volume (REV) for permeability.

Porosity and absolute permeability (experimental and estimated via Kozeny-Carman correlation) of SAMPLE 1 and SAMPLE 2 are summarized in Table 2.2. The peculiarity in terms of porosity reflects on the rock permeability, as the majority of pores are interconnected and contribute to fluid flow. The experimental absolute permeability of SAMPLE 2 has been obtained with laboratory tests performed on a bigger sample (1 inch in diameter core plug) of the same rock type, whose results are reported in Jin et al. (2007).

For both samples the pore diameter is estimated, as D_H and D_{eq}, by extending the concept of hydraulic diameter to the pore network and by calculating the equivalent diameter from the volume of the segmented pores. Results are reported in Table 2.3. In particular, $D_{eq,min}$ values give an important information about the minimum resolution that should be admitted for an adequate pore space discretization.

Table 2.2: Porosity and absolute permeability of the two sandstone samples.

Sample	ϕ	k_{exp} [Darcy]	$k_{Koz-Car}$ [Darcy]	$a_{v,gr}$ [mm^2/mm^3]
SAMPLE 1	0.236	3.204	5.94	30.0
SAMPLE 2	0.114	0.191	0.44	15.8

Table 2.3: "Hydraulic" and equivalent pore diameters of the two sandstone samples.

Sample	$\bar{D}_H$ [μm]	$\bar{D}_{eq}$ [μm]	$D_{eq,min}$ [μm]	$D_{eq,max}$ [μm]
SAMPLE 1	41	63	11	192
SAMPLE 2	17	60	5	124

2.5 Conclusions

To summarize, some appealing and underestimated capabilities of experimental techniques, X-ray computed tomography above all, are demonstrated.

Imbibition and drainage are performed according to the classical *unsteady-state* protocol. The displacement evolution is continuously monitored by means of fast X-ray radiographic projections, the recorded images are processed to convert the attenuation maps into fluid saturation maps and the fluid saturation profiles are derived. This work proves that using simple radiographies of multiphase flows provides a real-time and low-cost method for tracking flooding processes through rock core samples. Most important, due to the much higher frame rate attainable by taking radiographic images, when compared to traditional X-ray CT scanning, flows with higher injection rates can be followed. The availability of profiles describing the time evolution of the water and oil saturation within the core are an extremely valuable *a priori* information for history-matching, allowing to derive relative permeability and capillary pressure curves. Indeed, this time sequence of saturation profiles is expected to be a robust constraint for any inversion method used to retrieve macroscopic fluid flow properties of the core.

An exemplifying application is used to demonstrate the procedure, where a history match optimization is carried out to compute oil and brine relative permeability and capillary pressure curves for a drainage process. In principle, the radiography-derived saturation profiles can represent the input data for different history match procedures such as those implemented in PRORES–Sendra (PRORES), that is the most widespread software used by many petro-physical laboratories to process SCAL experiments. The proposed procedure appears to be fast and does not require any additional technical equipment. The diameter of the plug can be much larger than the one of the sample object of this study, thus adding statistical significance to the data. Here the choice of a relatively small sample is dictated by the need of the specimen to fit in the field of view of the detector and to be tomographed at a sufficiently high resolution.

Lastly, the digital sample provided by the full tomographic acquisition of the dry core and subsequent image reconstruction is used for pore space characterization and quantitative morphological measurements. The pore bodies are objectively identified via a distance-transform watershed algorithm, pore size and pore size distribution are easily deduced. This statistical analysis furnishes an extremely important information about the minimum resolution that should be adopted to accurately resolve the pore space under investigation.

The choice of an adequate REV undergoes the request to handle a volume with a sufficient number of pores and throats to be representative of the real porous medium. Here the suitability of the REV (a cube of side 0.8 mm) is verified through a sensitivity analysis on porosity. Bigger volumes may be considered, provided that

a lower resolution of the scanned sample is acceptable. Ultimately, a compromise between a resolution sufficient to capture the narrowest throat giving contribution to flow and a digital volume, which can be processed with the computing resources nowadays available, is desirable.

Chapter 3

Numerical methods

The problem of predicting macroscopic rock properties, such as relative permeability and capillary pressure, from the underlying microscopic structure has been studied for a long time. The recent advent of affordable computational resources able to process large datasets paved the way for numerical methods enabling predictions possible on "images" of rock plugs and providing results that would be arduous to obtain with traditional laboratory experiments.

Traditionally, the estimation of the most significant petro-physical properties is approached numerically with two different tools: pore network modelling and direct simulation.

The first approach consists in a prior extraction of a topologically representative network of the pore space from the image, that is a two- or three-dimensional lattice of stubby bodies (pores) connected by narrower channels (throats). Flows are subsequently modelled through the pore network. Bakke and Øren (1997) simulate a drainage displacement in a pore network derived, by modelling the main sandstone-forming geological processes on thin section images of a real sandstone. Dong and Blunt (2009) use the Maximal Inscribed Spheres (MIS) method, proposed by Silin and Patzek (2006), to extract a simplified pore network from X-CT images and compare calculated porosity and permeability with experimental results.

The second approach consists in solving the governing equations of flow and transport on a grid derived directly from the boolean three-dimensional image of the rock. Hazlett (1995) simulates capillary-dominated displacements in images of a Berea sandstone sample derived from X-ray CT to predict phase distributions and capillary pressure. Koroteev et al. (2014) exploit the Direct Hydrodynamic (DHD) Simulation technology to describe two-phase flow displacement processes and derive relative permeability curves at different flow regimes. Mostaghimi et al. (2012) simulate low-Reynolds-number flow and transport through digital samples of rock cores at the scale of pores, using a finite-difference solver. The absolute hydraulic permeability and the longitudinal dispersion coefficient are calculated. The same method is used to compute the permeability of a range of consolidated

and unconsolidated porous rocks (Mostaghimi et al., 2013). Zaretskiy et al. (2012) use the mixed finite-element/finite-volume model CSMP++ (Matthï et al., 2007) for simulating the pore-scale fluid flow and solute transport accompanied by chemical reactions in a digitalized Fontainebleau sandstone sample.

We focus on the second approach to study, characterize and synthesise via relative permeability and capillary pressure the dynamics of multiphase flow of immiscible fluids (i.e. oil and water) in the pore-space of a reservoir rock sample, mimicking routine laboratory measurements. The pore space of a sandstone sample reconstructed using X-ray computed tomography and segmented by image processing tools, as illustrated in Sections 2.3 and 2.4, provides the basic information required to generate a numerical grid suitable for CFD simulations.

The presented work bases on the followins steps:

(i) Single-phase flow is simulated in the digital sample previously reconstructed, allowing to compute the absolute permeability k.

(ii) Two-phase flows are simulated in the same digital sample following the *steady-state* approach.

(iii) The numerical output data are *up-scaled* to derive relative permeability k_r and capillary pressure P_c curves.

(iv) The threshold capillary pressure $P_{c,t}$ is estimated with three different methods.

The digital workflow proposed here guarantees a fast and cheap routine for computing petro-physical properties from small samples such as drilling cutting or crushed sidewall when suitable cores are not available. Thus, the suggested procedure is complementing and corroborating traditional experimental laboratory data. Obviously, the study is conducted at a pore level, thus the rock heterogeneities are captured at the micro-meter scale and cannot provide all the informations conveyed by a full diameter core (e.g., systems of fractures and their orientation).

The finite-volume/volume-of-fluid (FV-VOF) commercial solver ANSYS FLUENT® (`http://www.ansys.com/`) is used to simulate two-phase flows. FV-VOF solvers are computationally expensive, need high power computing (HPC) facilities and the communication between processors is often the bottleneck. Here this problem has been solved by running our simulations on a new generation top performance eight-core processors.

3.1 Mesh generation

Two fundamental strategies can be followed to construct a mesh for a digital sample of a complex, porous matrix. The simplest approach, by which the present results have been obtained, consists in generating an unstructured mesh of cubes, where the computational cells coincide with the void voxels obtained from the X-ray tomography. In the second approach, an unstructured, tetrahedral or hybrid mesh is automatically generated once a STL (Standard Tessellation Language) representation of the pore-grain interface is available. An STL file describes a raw unstructured triangulated surface by the unit normal and vertices (ordered by the right-hand rule) of the triangles using a three-dimensional Cartesian coordinate system. Several commercial tools are available, to this end. Some experience has been gained with the +FE module by Simpleware (http://www.simpleware.com/), which provides utilities for generating both surface (triangular/quadrilateral) and volume (tetrahedral/hexahedral) meshes. The resulting pore/rock surface is stair-step like for the cubic mesh and smooth for the tetrahedral mesh.

The voxel-based mesh generation approach presents some distinctive positive features. The fluid-solid interface reconstructed by X-ray tomography is inherently rough and any smoothing operation is arbitrary. The stair-step pattern of the interface represents the real surface roughness with length scale comparable to the voxel size. The cubicmesh generation process is fast and automatic (Gerbaux et al., 2010). This approach reduces the time needed to set up a mesh suitable for CFD studies and does not require specialized and costly commercial meshing softwares. Even for large volumes, the mesh generation process takes just a few minutes on a desktop computer.

The drawback of a voxel-based mesh is the direct dependence on the tomographic image resolution that could cause some regions to be under-resolved. The most natural way to overcome this problem is to use one of the many mesh adaptivity capabilities provided by most commercial CFD packages. The hanging node mesh adaptation technique available in Fluent ® provides the ability to operate on meshes with a variety of cell shapes, including hybrid meshes. The refined mesh is characterized by nodes on edges and faces that are not vertices of all the cells sharing those edges or faces. Ultimately, global and local (by Octree techniques (Samet, 2006)) refinements can be easily achieved by splitting the cubic cells, without affecting the quality of the mesh. The significant meshing flexibility unavoidably goes to the detriment of additional required memory.

The pore-grain (void-material) interface can be identified by the list of linear indexes of the voxels lying on the border of the pore space and connected to grains according to a given voxel-neighbourhood connectivity. For fluid-dynamic simulation a connectivity of 6 must be used, as fluxes propagate across contact surfaces. Given a connectivity of 6, one voxel of the pore space is on the interface if at least one

of the six (connected) neighbours is part of a solid grain. The identification of the pore/grain interface is required for subsequent selection of the surfaces where the boundary conditions have to be enforced.

The base mesh used in the present simulations contains about 9.80×10^5 hexahedral cells. The suitability of cubic meshes for this kind of simulations has been confirmed by Gerbaux et al. (2010), who compared results of cubic (i.e. hexahedral) and tetrahedral meshes and state that the differences between results are minimal.

3.2 Computational method

3.2.1 Volume of Fluid

Among the computational fluid dynamic (CFD) methods available for multi-phase immiscible fluid flows in porous rocks, the Immiscible Lattice Boltzmann Model (ILBM) and the Finite-Volume Volume-of-Fluid (FV-VOF) method are the most widely used.

LB methods can be seen as a natural evolution of the cellular automata fluids. The LB formulation has been proposed by Gunstensen et al. (1991) and have emerged rapidly (Wolfram, 1986; Succi, 2001). The elemental fluid cell is identified with the (cubic) voxel of the wet pore-space as segmented from the tomographic volume. Thus explicit meshing of the pore-space is not necessary. The wet cells of this regular 3D set are populated by particles that can move (i.e. stream) according to 18 discrete velocities or remain at rest, when the most common D3Q19 lattice geometry is adopted. Within one cell the microscopic particle population is distributed according to a particle-distribution-function that evolves in time. Cell macroscopic physical properties and hydrodynamic variables can be computed by microscopic lattice population-fractions. This particle-based technique simulates propagation and collision of particles. The particles can represent different phases interacting with each other. For two-phase incompressible flows two particle distributions are necessary at each wet cell site thus doubling the amount of data with respect to the single phase case. The dynamics of the fluid-fluid interface are governed by additional forcing terms that mimic the interaction between immiscible fluids. Fluid wettability is introduced by adding a fluid-rock adhesive term rather than a contact angle. Examples of relative permeability estimates obtained by means of LB methods are reported by Keehm et al. (2004); Hao and Cheng (2010).

An alternative to LBM is to resort to traditional CFD methods as the FV-VOF. The VOF is a technique largely employed to tackle problems in which two or more immiscible fluids are present and the dynamics of the interface is of interest. It was first introduced by Nichols and Hirt (1975, 1981). Various improvements have been developed subsequently and a non-exhaustive list is reported by Tang et al. (2004).

Here VOF is used for tracking the shape of the water/oil interface.

The Volume of Fluid (VOF) model is based on the concept of *volume fraction* α. The porous medium is a multiphase system, where the phases are denoted by i = 1, 2, 3, ... , N. If U_i is the volume occupied by the i-phase within the considered volume U, at time t and space position (x, y, z):

$$\alpha_i(x,y,z,t) = \frac{U_i(x,y,z,t)}{U} \qquad \sum_{i=1}^{N} \alpha_i = 1; \tag{3.1}$$

The phase volume fraction α is defined at each computational cell of the fixed regular and uniform grid and satisfies the following conditions for interface tracking:

$$\alpha_i(x,y,z,t) = \begin{cases} 0 & \text{outside the i-th phase} \\ 1 & \text{inside the i-th phase} \\ > 0, < 1 & \text{at the fluid-fluid interface} \end{cases}$$

In an oil-water system the two volume fractions are related as $\alpha_o = 1 - \alpha_w$.

The well-known Navier-Stokes equations are solved. The mass- and momentum-conservation equations for the oil-water "mixture" are:

$$\frac{\partial \rho_m}{\partial t} + \nabla \cdot (\rho_m \boldsymbol{v}_m) = 0 \tag{3.2}$$

$$\frac{\partial (\rho_m \boldsymbol{v}_m)}{\partial t} + \nabla \cdot (\rho_m \boldsymbol{v}_m \boldsymbol{v}_m) = -\nabla P_m + \gamma_m \nabla^2 \boldsymbol{v}_m + \rho_m g + \boldsymbol{F}_{ST} \tag{3.3}$$

where ρ_m and γ_m are, respectively, the mixture density and dynamic viscosity and $\boldsymbol{v}_m$ and P_m the mixture velocity and pressure. The term $\boldsymbol{F}_{ST}$ stands for the body force due to the surface tension, g is the gravity vector.

Here the fluids are considered immiscible and incompressible. Thus, the velocity field is subject to the incompressibility constraint $\nabla \cdot \boldsymbol{v}_m = 0$.

According to the local value of α, the thermo-physical properties are assigned to each control volume within the domain and computed as weighted average of the corresponding pure fluid properties, where volume fractions α_o and α_w are used as weights:

$$\rho_m = \alpha_o \, \rho_o + \alpha_w \, \rho_w \qquad \gamma_m = \alpha_o \, \gamma_o + \alpha_w \, \gamma_w \tag{3.4}$$

After solving Eq. (3.2) and Eq. (3.3), the volume fraction function is advected with the velocity field $\boldsymbol{v}_m$. The continuity of the secondary phase (i.e. oil) is enforced by the following equation:

$$\frac{\partial \alpha_o}{\partial t} + \boldsymbol{v}_m (\nabla \alpha_o) = 0 \tag{3.5}$$

Given the fixed grid, the VOF algorithm updates the volume fraction α, once the velocity field $\boldsymbol{v}_m$ and the volume fraction α at the previous step (Euler explicit scheme) are known.

The volume fraction function is discontinuous passing through the interface. In 2D the interface should look like a continuous smooth line. The reconstruction problem consists in finding the appropriate approximation to the section of the interface in each cell, by knowing the volume fraction in the considered cell and the neighboring cells. Here the accurate VOF Piecewise Linear Interface Construction (PLIC - GeoReconstruct) method is used for its accuracy. The method tracks and approximates the interface with piecewise linear segments. In each cell the interface has a linear slope which defines the unit normal vector $\hat{n}$ to the segment. The normal unit vector $\hat{n}$ and the volume fraction in the cell uniquely determine a straight line. This represents the *reconstruction* step. Once the interface has been reconstructed, it must be moved by the underlying flow field (*propagation* step). Here the pressure-implicit with splitting of operators (PISO) scheme for pressure-velocity coupling is used (Ferziger and Perić, 2001). The non-iterative time advancement (NITA) option for time stepping has been preferred in the present calculations for its efficiency since it reduces the computational time and allows only one outer iteration per single time step.

The basic idea behind FV methods is to convert the governing equations to algebraic equations that can be solved numerically. This technique consists of integrating the governing equations on the control volumes generated by the meshing process, yielding discrete equations that conserve each quantity on a control-volume basis. The VF commercial solver FLUENT® adopts a cell-based, co-located discretization approach (Ferziger and Perić, 2001). The accuracy of the available spatial discretization algorithms ranges between first and fourth-order. In the present application second-order upwind schemes for the advective term are preferred for robustness, while the viscous term is discretized by the least-squares method.

3.2.2 Surface force model

The VOF-PLIC method is coupled with the continuum surface force (CSF) algorithm for approximating the surface tension term $\boldsymbol{F}_{ST}$ in Eq. (3.3). The CSF model has been proposed by Brackbill et al. (1992). In a simple case of constant surface tension along a fluid-fluid interface, at equilibrium, the pressure drop across the interface depends on the surface tension and the two radii of curvature, as stated by the Young-Laplace equation (1.13).

In the CSF model the surface curvature is computed from local gradients in the surface normal n at the interface. The surface normal n is defined as the gradient of the secondary phase, i.e. oil, volume fraction:

$$n = \nabla \alpha_o \tag{3.6}$$

The curvature κ can be expressed in terms of the divergence of the unit surface normal $\hat{n}$:

$$\kappa = \nabla \cdot \hat{n} \tag{3.7}$$

where

$$\hat{n} = \frac{n}{|n|} = \begin{cases} -1 & \text{if } n \text{ points the water phase} \\ +1 & \text{if } n \text{ points the oil phase} \end{cases}$$

The force acting at the interface can be expressed as the volume force $\boldsymbol{F}_{ST}$, as follows:

$$\boldsymbol{F}_{ST} = 2\sigma_{o,w}\kappa \frac{\rho_m \nabla \alpha_o}{(\rho_o + \rho_w)} \tag{3.8}$$

where $\sigma_{o,w}$ is the oil-water surface tension. Eq. (3.8) shows how the volume force of a cell is proportional to the mixture density ρ_m in the cell.

The wettability properties of the solid surface are specified through a static contact angle θ_s coupled with the wall-adhesion option available in the VOF model. The imposed θ_s that the fluid-fluid interface is assumed to form with the wall is used to adjust the surface normal in the cells near the wall and, in turn, the interface curvature near the wall. The surface unit normal at the fluid cell next to the wall is:

$$\hat{n} = \hat{n}_w \, cos\,(\theta s) + \hat{t}_w \, sin\,(\theta s) \tag{3.9}$$

where $\hat{n}_w$ and $\hat{t}_w$ are the unit vectors normal and tangential to the wall, respectively. The combined use of the the surface normal thus calculated and the surface normal computed form the gradient of the phase volume fraction determine the local curvature of the interface, appearing in the surface tension term $\boldsymbol{F}_{ST}$ of the CSF model.

It must be borne in mind that the calculation of the surface tension term on triangular or tetrahedral meshes is not so accurate as on quadrilateral and hexahedral meshes, hence it is strongly recommended to mesh with quadrilaterals or hexahedra, regions where effects of surface tension are important.

3.3 Pore-scale simulations

3.3.1 Single-phase flow

In the present work the SAMPLE 2 of reservoir sandstone rock is analysed. The voxel size of the digital sample is 4.5 μm and the sub-volume used for numerical simulations is a 200^3 voxels cube. Single-phase flow simulations are performed to estimate the hydraulic absolute permeability, using the method described by Piller et al. (2009). The traditional laboratory permeability tests are mimicked by injecting a single fluid within the pore space initially saturated with the same fluid. As we are only concerned with laminar flow of liquids at very low pore-Reynolds number, the incompressible, steady-state Navier-Stokes equations are solved.

Three different types of boundary conditions are enforced on the boundary of the computational domain. No-slip boundary conditions are imposed on the solid-fluid interface, while on the fluid-fluid open portions of the boundary either velocity-inlet or pressure-outlet conditions are enforced. The choice of boundary conditions is of course rather arbitrary. Nevertheless, the point here is to reproduce a flow subject to specific flow conditions and compute the transfer function of the porous sample with respect to pressure gradients originated by the imposed injection flow rate. In this perspective, the enforcement of velocity-inlet and pressure-outlet boundary conditions seems appropriate.

The sample absolute permeability is estimated by applying the Darcy's law to a water injection and subsequently to an oil injection. Different flow rates are tested. The results underline the significant influence of the fluid injection velocity on the computed k values. At high rates (e.g above 0.1 m/s) the pore Reynolds number does not assure the validity of Darcy's law and the absolute permeability of the two fluids, $k_{sim,o}$ and $k_{sim,w}$, are sensibly different as shown in Table 3.1. The permeability values converge to the same value only at lower rates (e.g. 0.01 m/s). This velocity value, ensuring laminar flow, is adopted as inlet velocity at the injection section of two-phase flow simulations. The corresponding computed absolute permeability is in excellent agreement with the experimental absolute permeability (0.191 Darcy).

Table 3.1: Computed absolute permeability at different fluid injection velocities.

Velocity inlet [m/s]	$k_{sim,o}$ [Darcy]	$k_{sim,w}$ [Darcy]
0.15	0.162	0.090
0.05	0.199	0.152
0.01	**0.206**	**0.204**

3.3.2 Two-phase flow

Two-phase flows are numerically performed allowing to estimate relative permeability and capillary pressure values for both drainage and imbibition. The experimental procedure here adopted is referred to as *steady-state* method (see Section 1.4.1) even though the flow dynamics is typically non stationary (Tiab and Donaldson, 2004). Multiple experiments are necessary to estimate the entire relative permeability and capillary pressure curves over a range of saturation.

In *drainage* the sample is initially saturated with water, in *imbibition* the sample is initially saturated with oil. Oil and water are co-injected within the water-wet sample. The considered fluid properties are as follows:

$$\begin{aligned} \rho_w &= 998.2 \ \text{kg/m}^3 \ ; & \gamma_w &= 0.001 \ \text{kg/m} \cdot \text{s} \\ \rho_o &= 800.0 \ \text{kg/m}^3 \ ; & \gamma_o &= 0.003 \ \text{kg/m} \cdot \text{s} \\ \sigma_{o,w} &= 0.05 \ \text{N/m} \ ; & \theta_s &= 30^\circ \end{aligned}$$

where ρ and γ stand for the fluid density and dynamic viscosity, respectively, $\sigma_{o,w}$ is the surface tension and θ_s the static contact angle.

Numerically, both the constant injection rate and the constant pressure drop cases can be simulated. Here the constant mixture velocity is imposed at the sample's inlet while the static pressure is enforced at the outlet. In turn, the latter condition implies zero capillary pressure at outlet, a boundary condition that is commonly used in special core analysis simulations. The zero-velocity (*no-slip*) condition is imposed at the pore-fluid interface. An entry velocity of 0.01 m/s yields a pore-scale Reynolds number R_p of 4×10^{-3}, assuming the square root of the absolute permeability as the characteristic linear dimension. The applied boundary conditions for drainage and imbibition are summarized in Table 3.2.

Table 3.2: Boundary conditions used in the two-phase flow simulations.

Boundary	Condition
Inlet	Velocity inlet; α_o assigned
Outlet	Pressure outlet; either $\alpha_o = 1$ (imbibition) or $\alpha_w = 1$ (drainage) assigned to recirculating fluid
Pore/rock interface	No-slip condition; wall adhesion specified through static contact angle θ_s.

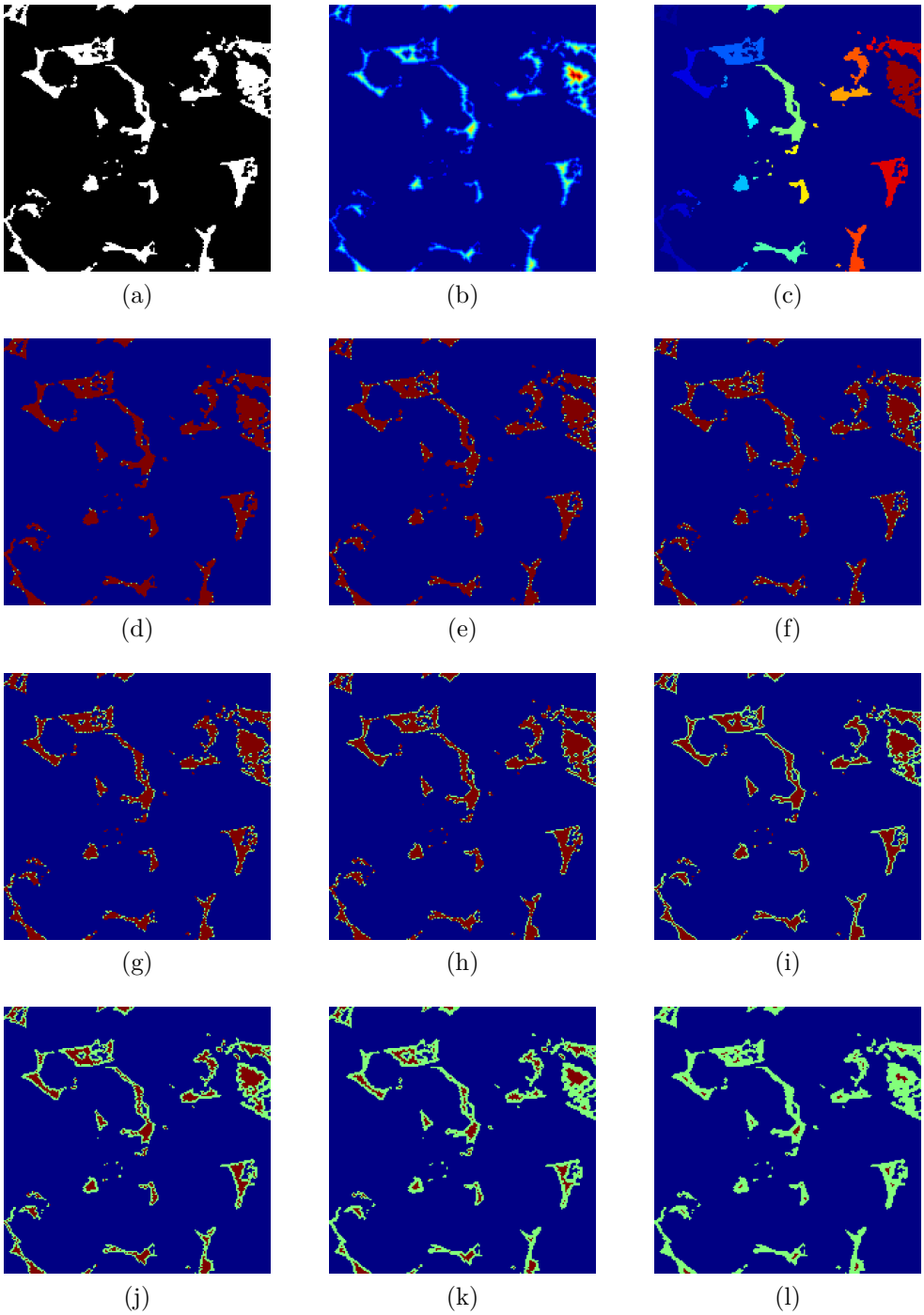

Figure 3.1: (a) Binary inlet section. (b) Distance map of inlet section. (c) Labelled inlet section. From (d) to (l) fluid maps at the inlet section at increasing water/oil ratios. Solid matrix is blue-coloured, water is in green, oil is in red.

According to the wetting properties of the rock sample, the water layer covers the pore surface, while the oil occupies the core of the pore body. Thus, at the fluid inlet section of the meshed pore-space, specialized image-processing tools are used to identify the boundaries of the pores and to adjust the thickness of the water layer according to the prescribed water/oil volumetric ratio, as shown in Figure 3.1. Ten tests are performed, by assigning the following water volume fractions to the inlet section: $\alpha_w = 0\%$ (full drainage); $\alpha_w = 2.88\%$; $\alpha_w = 8.81\%$, $\alpha_w = 14.33\%$; $\alpha_w = 21.19\%$; $\alpha_w = 26.26\%$; $\alpha_w = 41.91\%$; $\alpha_w = 62.24\%$; $\alpha_w = 80.26\%$; $\alpha_w = 95.93\%$. Each test, corresponding to a "steady-state" laboratory experiment, provides a couple of points in the oil and water relative permeability curves and a single point in the capillary pressure curve. The complete curves can be derived by changing the oil/water injection ratio and measuring the microscopic variables when fluid displacement reaches equilibrium.

3.4 Results

3.4.1 Relative permeability

Relative permeability estimates are cumbersome, since they usually rely on measurement techniques that do not have access to the internal topology of the pore space. On the contrary, numerical methods allow for measurements on internal sections of the sample that are not possible with traditional laboratory experiments which provide results with respect to inlet and outlet sections only. Here measurements of pressure at inlet and outlet are acquired on sections intersecting the cell-centre of the first cell and the cell-centre of the last cell in the flow direction, in order to avoid perturbations due to the imposed boundary conditions.

Once reached the stationary conditions, in terms of fluid saturation and pressure drop, the effective permeabilities for both oil and water are obtained by using Darcy's law:

$$\boldsymbol{q}_w = -\frac{k\, k_{r,w}}{\mu_w} \nabla P_w \tag{3.10a}$$

$$\boldsymbol{q}_o = -\frac{k\, k_{r,o}}{\mu_o} \nabla P_o \tag{3.10b}$$

where $\boldsymbol{q}_{w,o}$ denotes the specific discharge of the considered phase and $\nabla P_{w,o}$ is the phase pressure gradient.

The numerical output data must be up-scaled to estimate k_r and P_c as function of the water saturation, that are the set of data necessary for macro-scale reservoir

simulations. The variable $\boldsymbol{q}_{w,o}$ is a volume-averaged specific discharge (weighted on the total sample volume), whereas the phase pressure at inlet and outlet section used to compute the phase pressure gradient $\nabla P_{w,o}$ is an intrinsic surface-averaged pressure (weighted on the void fraction of the section occupied by the considered phase).

The distribution of the two fluid phases at an advanced stage of drainage is depicted in Figure 3.2, where the sandstone material is not shown. The oil phase is shown in red, the water phase in transparent blue. The volume rendering shows the complexity of the process with differential advancement of menisci inside the porous space. The temporal evolution of the fluid interfaces and their morphology are continuously visualized. This is of great help for the full understanding of the distinguishing features of these pore-scale non-equilibrium processes. Fingering instability of the displacing front due to the viscosity contrast of the competing fluids, snap-off, bubble clustering growth, ganglia formation and coalescence are some pore-scale dynamic phenomena that can be captured. Trapping mechanisms, the related residual saturation of the non-wetting phase and the irreducible saturation of the wetting one are associated to these complex interfacial phenomena, the medium topology and the rock wettability.

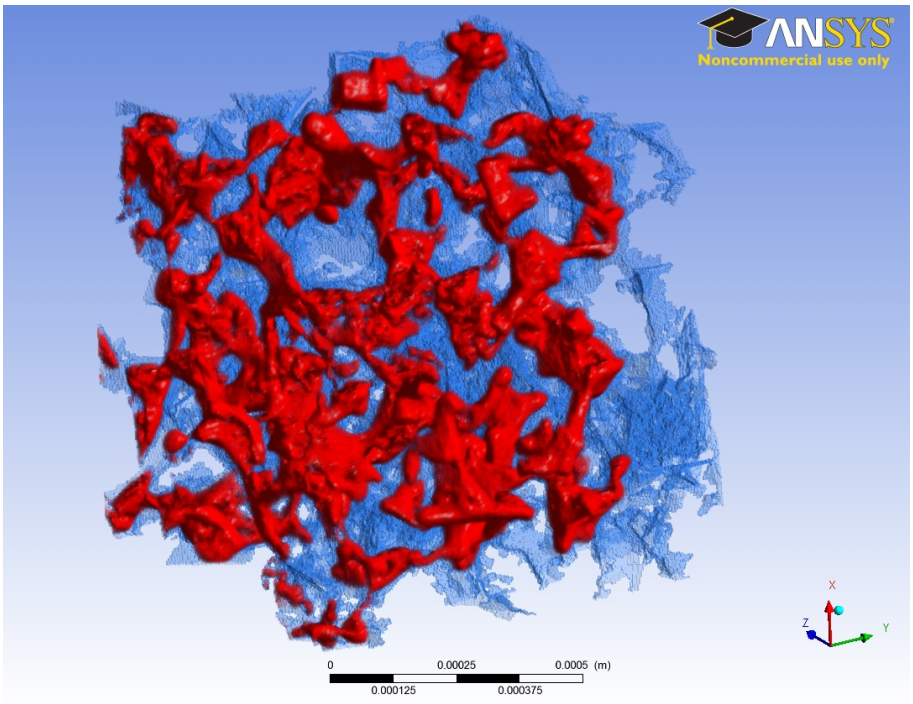

Figure 3.2: Evolution of the oil phase (displayed in red) during a drainage process in a 200^3 voxels sample. The pore-grain interface is shown in light blue.

The sample average saturation, pressure drop and flow rates are continuously monitored during the transient process. Both saturation versus time (Figure 3.3) and pressure drop across the sample versus time (Figure 3.4) profiles are used to identify the attainment of stationary conditions necessary for measurements.

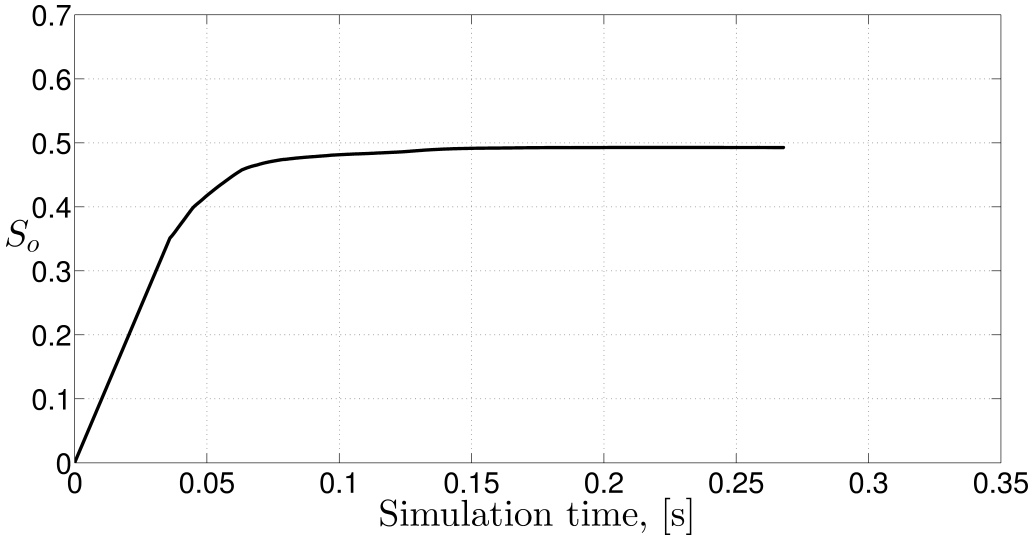

Figure 3.3: Oil saturation versus simulation time, inlet water fraction $\alpha_w = 8.81\%$.

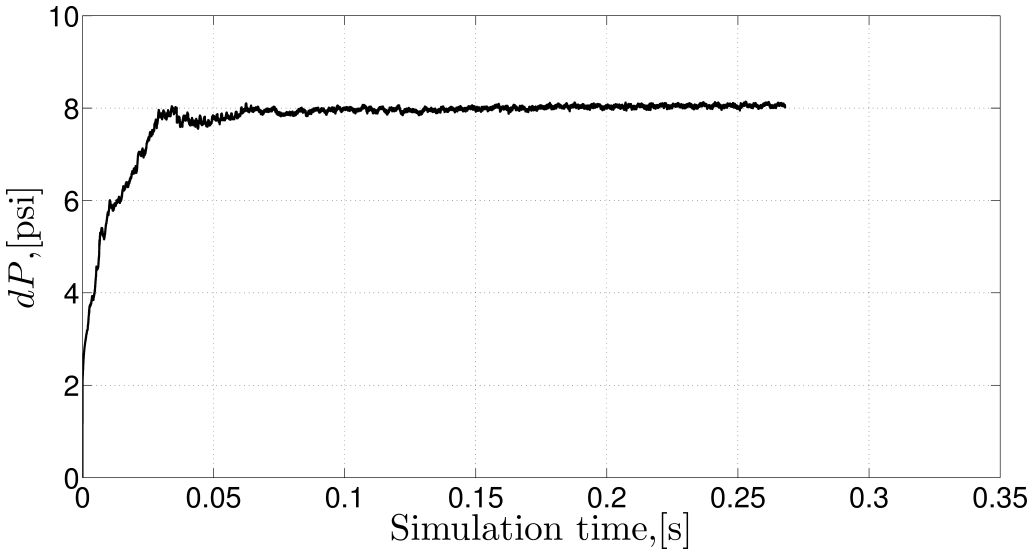

Figure 3.4: Pressure drop versus simulation time, inlet water fraction $\alpha_w = 8.81\%$.

The computed relative permeability curves are presented in Figure 3.5(a) and fitted with the classical two-parameter Corey correlation:

$$k_{r,w} = k_{r,w,\max}\left(\frac{S_w - S_{w,i}}{1 - S_{w,i} - S_{o,r}}\right)^{n_w} \tag{3.11a}$$

$$k_{r,o} = k_{r,o,\max}\left(\frac{1 - S_w - S_{o,r}}{1 - S_{w,i} - S_{o,r}}\right)^{n_o} \tag{3.11b}$$

The irreducible water saturation $S_{w,i}$ is computed by extrapolation with piecewise cubic Hermite polynomial interpolation (PCHIP) from the $k_{r,w}$ set of data prescribing $k_{r,w}(S_{w,i}) = 0$. A similar PCHIP procedure allows to compute the residual oil saturation $S_{o,r}$ from the $k_{r,o}$ set by prescribing $k_{r,o}(S_{o,r}) = 0$. The computed values are:

$$S_{w,i} = 0.1993; \quad S_{o,r} = 0.1791$$

Each couple of points, at a fixed water saturation value, represents a single test. The comparison between the simulated and the experimental data for drainage is shown in Figure 3.5(b). The regression of the calculated relative permeabilities with the Corey correlation yields the following values for the parameters, appearing in Eq. (3.11):

$$\begin{aligned} k_{r,w,\max} &= 0.344; \quad n_w = 4.205 \\ k_{r,o,\max} &= 0.972; \quad n_o = 0.953 \end{aligned} \tag{3.12}$$

The numerical method allows computing values across the entire saturation range. The calculated relative permeability curve for water is in good agreement with experimental data while a remarkable disagreement is observed for the oil relative permeability, as highlighted in Figure 3.5(b).

The small dimensions of the digital sample might explain this discrepancy. Moreover, the advancing non-wetting phase (oil) is more susceptible of instability in terms of pressure and velocity field than the wetting phase (water). This instability could affect the $k_{r,o}$ estimation, as proven by Figure 3.6, in which $k_{r,o}$ (red line) and $k_{r,w}$ (blue line), computed during the stage of the process at constant saturation, are shown. The disagreement between experimental and numerical results could be ascribed to the different approach in k_r estimation, as well: in the laboratory tests only the wetting-phase (water), as a continuous fluid network through the pore space, is connected to inlet and outlet sections and, in turn, to the measurement apparatus; conversely, measurements acquired on the discontinuous non-wetting phase (oil) could be ambiguous and misleading.

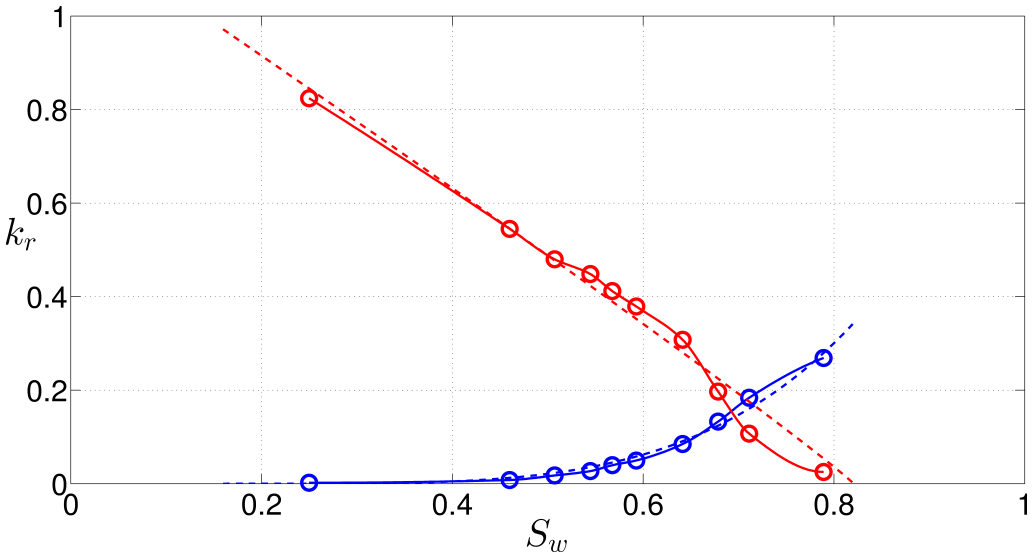

(a)

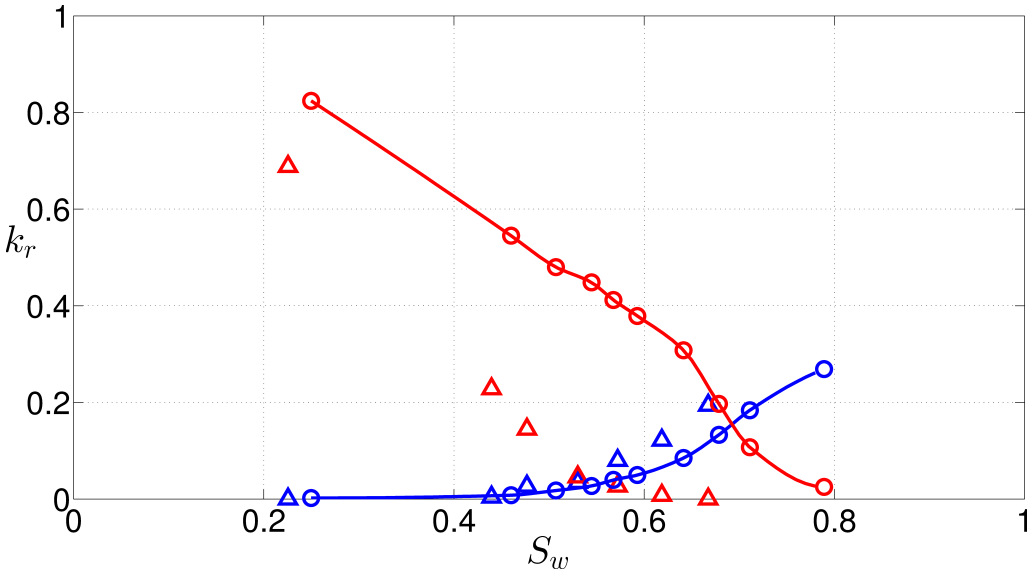

(b)

Figure 3.5: Water (blue) and oil (red) relative permeabilities as a function of the sample water saturation. (a) Computed data for drainage (∘ symbol), interpolating polynomial (solid line) and Corey fitting (dashed line). (b) Experimental data (△ symbols) and interpolating polynomial (solid line) of the computed data for drainage (∘ symbol).

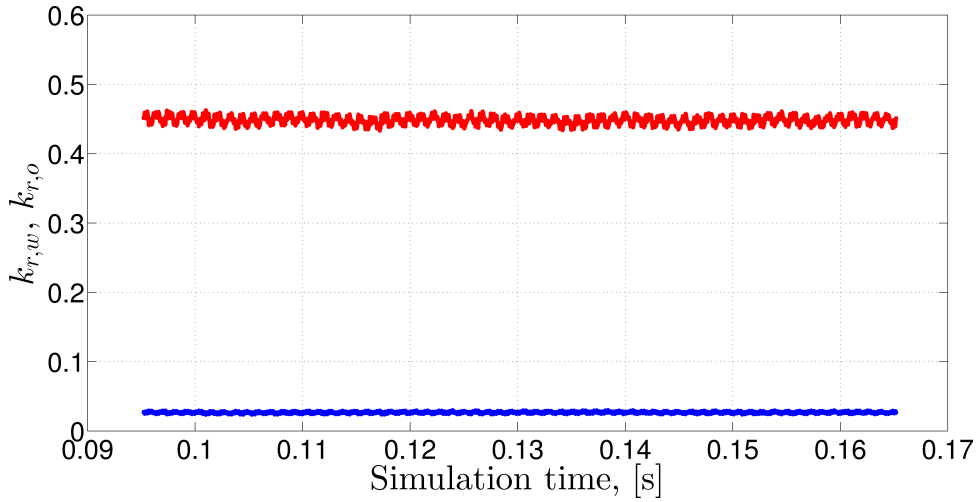

Figure 3.6: Water and oil relative permeabilities, calculated during the final stage of a drainage. The red graph refers to oil, the blue graph refers to water. Inlet water fraction $\alpha_w = 8.81\%$

3.4.2 Capillary pressure

The capillary pressure P_c represents a key parameter for reservoir studies. Let's recall its universally accepted macroscopic definition, for an oil-water water-wet system:

$$P_c = < P_o > - < P_w > \tag{3.13}$$

Because of the small size of the digital sample, $< P_o >$ and $< P_w >$ are computed as intrinsic volume-averaged pressures at every time step and their difference yields the capillary pressure. One measurement at stationary state is a point of the capillary pressure curve. The computed capillary pressure data for drainage are fitted with the two-parameters Bentsen-Anli function, as shown in Figure 3.7(a):

$$P_c = P_{c,t} - P_{c,s} \log\left(\frac{S_w - S_{w,i}}{1 - S_{w,i}}\right) \tag{3.14}$$

where $P_{c,t}$ is the *threshold* capillary pressure and $P_{c,s}$ is the so-called *span* pressure.

A comparison with the experimental data is reported in Figure 3.7(b). The computed capillary pressure is in agreement with the experimental capillary pressure for water saturations above 46%. The regression of the calculated P_c with the Bensten-Anli correlation yields the following values for the parameters, appearing in Eq. (3.14):

$$P_{c,t} = 0.52; \qquad P_{c,s} = 0.88 \tag{3.15}$$

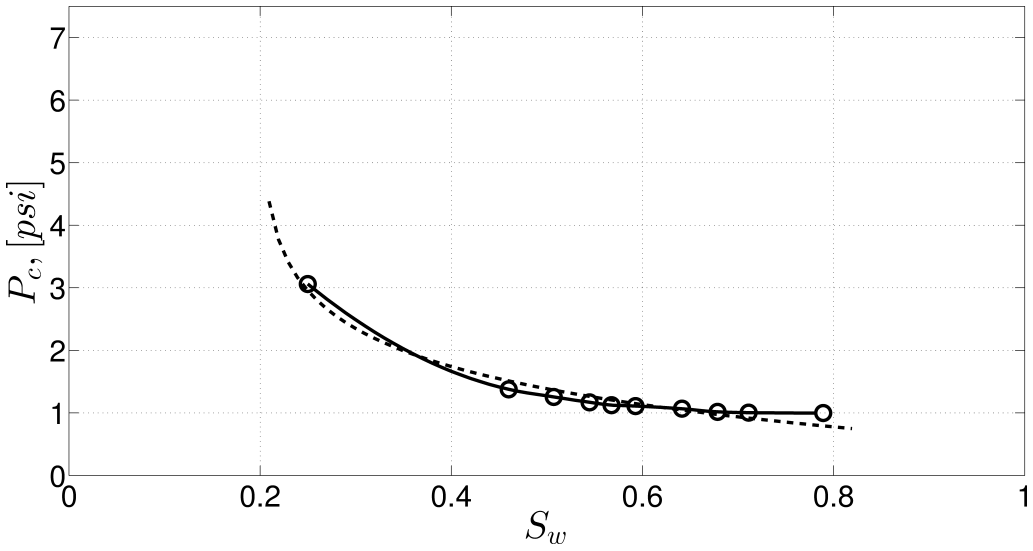

(a)

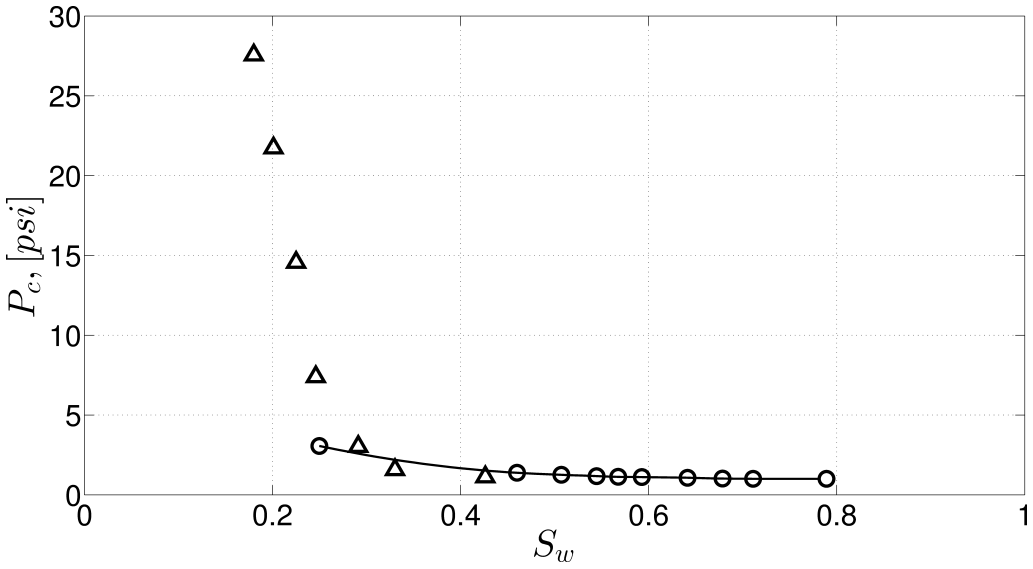

(b)

Figure 3.7: Capillary pressure as a function of the sample water saturation. (a) Computed data for drainage (∘ symbol), interpolating polynomial (solid line) and Bentsen-Anli fitting (dashed line). (b) Experimental data (△ symbol) and interpolating polynomial (solid line) of the computed data for drainage (∘ symbol).

Figure 3.7(b) shows that different ranges of S_w are covered by laboratory experiments ($\triangle$ symbol) and numerical experiments ($\circ$ symbol). In laboratory experiments one fluid displaces another in imbibition or drainage processes, that are often carried out at displacement rates much higher than those typical of reservoir phenomena. The numerical methods allow simulating fluid displacement processes at lower velocities and the correspondingly low pore-scale Reynolds numbers (0.004 in the present simulations) ensure a laminar flow (see Section 3.3.1). This gives the chance to explore lower values of P_c at high S_w (Figure 3.7(b)).

While the injection oil/water ratio is imposed, the resulting degree of saturation is a dependent variable that is also influenced by the morphology of the pore space and the wettability of the fluid/rock system. With a water fraction at the inlet section of 2% (8%) the final water saturation is about 46% (50%). On the other hand, in a full drainage experiment (only oil is injected), the final water saturation is 25%. Thus a very small increase in water fraction (2%) prevents the oil to displace an additional 21% in water. This behaviour is shown as a saturation gap in Figures 3.7(a) and 3.7(b).

The threshold capillary pressure is the pressure at which the drainage process begins, in other words the pressure that should be exceeded before any oil can start flowing through the sample (Egerman et al., 2006; Christiansen, 2008). It is recognized that in a drainage process, the largest pore radius that the non-wetting phase encounters at the entrance of the pore space determines the threshold capillary pressure. Here three alternative methods are used to estimate the $P_{c,t}$.

The first method is based on a morphological analysis of the pore-space. The largest pore radius in a 100 micron thick inlet section is estimated computing the medial path for passing through the thick section and inflating the *maximal spheres* with centre on the path. A method for generating the medial path that is used in virtual endoscopy is adopted (Schena and Favretto, 2004). The $P_{c,t}$ is then obtained from the Young-Laplace equation (1.14), where r is the radius of the largest maximum sphere with centre on the media axis and is estimated via distance transform. The $P_{c,t}$ value is 0.56 psi.

The second method for estimating $P_{c,t}$ exploits a displacement simulation that fulfills a classical protocol used for laboratory experiments (Christiansen, 2008). The core sample, saturated by water, is invaded by oil at very low flow rate (2×10^{-3} m/s), in order to consider the pressure difference across the sample nearly equal to the capillary pressure. Vice versa, at higher injection rates, viscous resistance would increasingly dominate the pressure drop (Christiansen, 2008). The $P_{c,t}$ is measured at the very first stage of the injection process, as shown in Figure 3.8. The $P_{c,t}$ value is 0.34 psi.

The third method for estimating $P_{c,t}$ consists in a step-by-step drainage. Oil is injected into the sample for a fixed number of simulation steps with a predefined injection rate. Then the simulation is repeated several time, each time halving the

oil rate. In other words, the method minimizes the oil injection velocity down to condition of no-flow. The threshold capillary pressure is derived as the intercept of the regression line fitting the capillary pressure versus velocity inlet, as shown in Figure 3.9. The estimated $P_{c,t}$ is 0.24 psi.

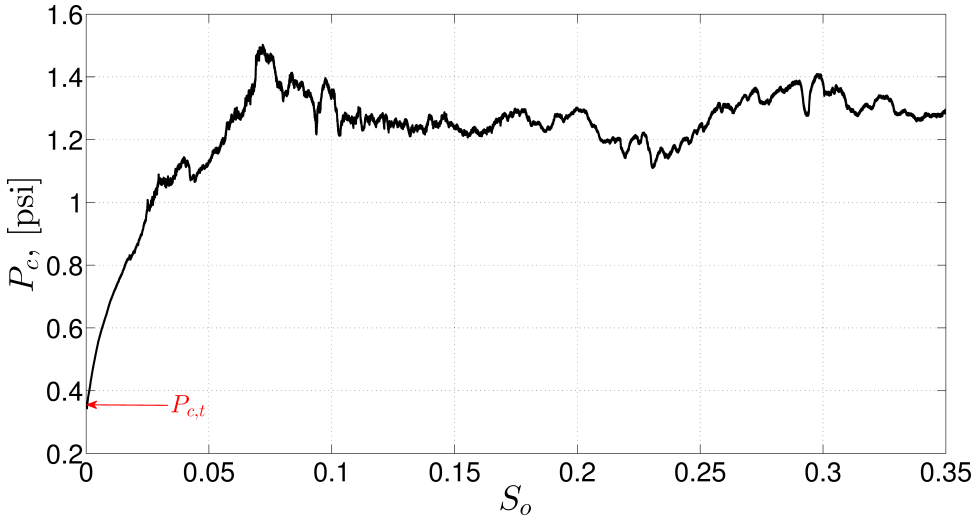

Figure 3.8: Capillary pressure as a function of oil saturation. Oil injection rate 0.002 m/s .

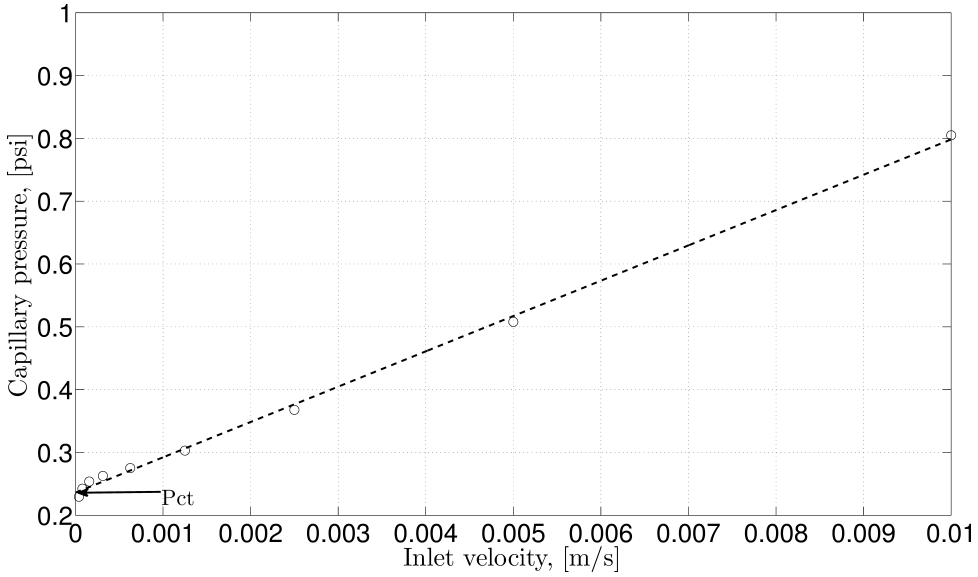

Figure 3.9: Capillary pressure as a function of the oil inlet velocity.

The step-by-step drainage is intended to compute a lower limit for the $P_{c,t}$. Namely, the method yields the minimum pressure difference capable of intruding a minimum amount of oil through the inlet section of the sample. This pressure difference is therefore related to the capillary pressure acting across the largest opening at the inlet section. Nevertheless, the actual threshold capillary pressure corresponds to the pressure difference that must be applied across the sample, in order to allow a continuous filament of oil to pass through the sample (Egerman et al., 2006). This pressure difference is related, in turn, to the capillary pressure acting across the largest among the smallest openings (throats) encountered along all the possible paths which connect inlet and outlet sections of the sample. These considerations provide an explanation for the lowest value of $P_{c,t}$ returned by the third method, among all the proposed methods and suggest that the third method should yield reliable results when applied to a sufficiently large sample, such that the areal pore-size distribution does not differ significantly from the volumetric pore-size distribution. In spite of the aforementioned limitations, the method has the lowest computational cost among the proposed methods for the calculation of $P_{c,t}$ and, for the present sample, provides a value of $P_{c,t}$ of the same order of magnitude as the other methods.

The graph in Figure 3.8 shows unstable values of capillary pressure at increasing saturation values. It refers to a capillary pressure experiment carried out according to the aforementioned method proposed by Christiansen (2008), exclusively devoted to threshold capillary pressure estimation. The experiment is carried out with injection velocity 0.002 m/s, i.e. 50 times lower than the one adopted for capillary pressure and relative permeability estimates. In addition these measurements of capillary pressure are taken before breakthrough, therefore well away from the plateau where the saturation reaches the complete stability. In general, minor capillary pressure instability can manifest also at stable values of saturation since it is related to the change in morphology of the oil/water interface.

The threshold capillary pressure $P_{c,t}$ values computed with the aforementioned methods are summarized in Table 3.3.

Table 3.3: Threshold capillary pressure calculated with different methods.

Method	$P_{c,t}$ [psi]
Morphological method	0.56
Slow drainage $v_{\text{in}} = 0.002\,\text{m/s}$	0.34
Step-by-step drainage	0.24
Fitting, Eq. (3.14)	0.52

3.4.3 Hysteresis effect

The imbibition process is mimicked following the same procedure adopted for drainage: five tests, each corresponding to a different oil/water injection volumetric ratio, are performed to derive the relative permeability and capillary pressure curves, in accordance with the steady-state protocol. The water volume fractions assigned to the inlet section are $\alpha_w = 100\%$ (full imbibition); $\alpha_w = 70.31\%$; $\alpha_w = 57.27\%$; $\alpha_w = 34.05\%$; $\alpha_w = 14.33\%$. All the displacements are carried out on the sample initially filled with oil ($S_o = 1$). In traditional laboratory experiments, imbibition after primary drainage usually starts at irreducible water saturation $S_{w,i}$, thus $S_o = 1 - S_{w,i} \neq 1$. Nevertheless, the purpose here is to verify if a different behaviour of k_r and P_c occurs when the wetting phase (water) saturation is increased or decreased in the rock sample.

Figure 3.10 shows the comparison between the simulated drainage (∘ symbol) and imbibition (□ symbol) data. The hysteretical behaviour is evident and confirms a rule of thumb maintaining that the relative permeabilities of the non wetting phase during imbibition are lower than those for drainage, at equal saturation values (Geffen et al., 1951).

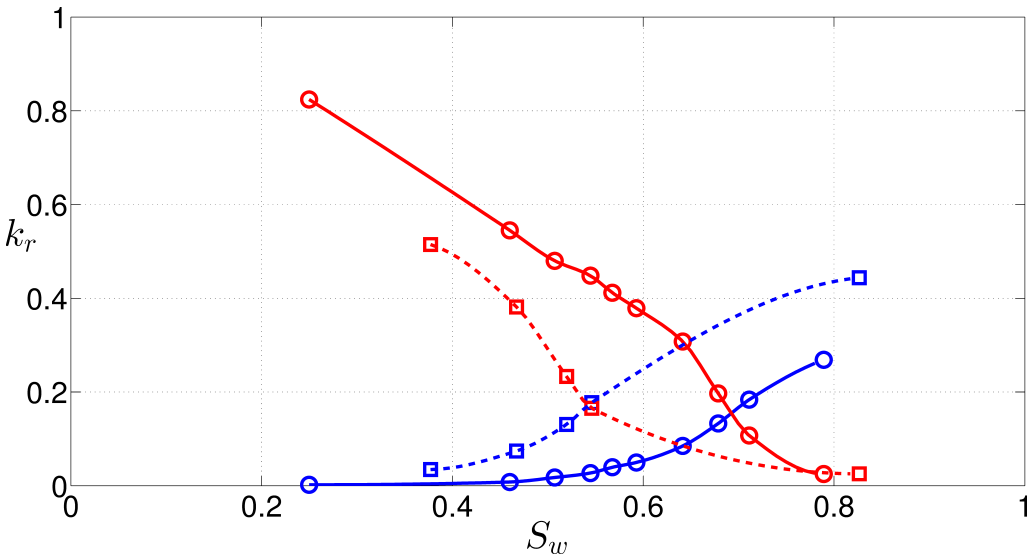

Figure 3.10: Water and oil relative permeabilities as a function of the sample water saturation. Interpolating polynomial (solid line) of the computed data for drainage (∘ symbol) and interpolating polynomial (dashed line) of the computed data for imbibition (□ symbol).

An analogous effect is observable in the simulated capillary pressure curves. The P_c data for drainage (∘ symbol) and imbibition (□ symbol) are displayed in Figure 3.11, together with the corresponding interpolating polynomials, drawn as a solid line and a dashed line, respectively. The capillary pressure imbibition curve is not complete and data span a range of water saturation values from 38% to 83%. Results corroborate the theory that numerical simulations are capable to inspect the portion of the capillary pressure curve at lower P_c values, when compared to the laboratory tests. The evidenced hysteretical behaviour of capillary pressure complies with the physics of drainage and imbibition phenomena. During imbibition, when the pressure in the oil phase slowly decreases, water tends to spontaneously imbibe the pore space and S_w increases. Normally, the measured capillary pressure values are lower than those for drainage, at a fixed S_w. Once the pressure in the water phase equates the pressure in the oil phase ($P_c = 0$), higher S_w values can be reached by forcing water to displace more oil, so that the water pressure exceeds the oil pressure. This explains the slightly negative P_c value (-0.18 psi) at $S_w = 83\%$.

In Figure 3.12, the comparison between numerical (□ symbol) and experimental (△ symbol) results is shown. Different ranges of S_w are covered by the two methods, as stated for drainage. Numerical and experimental set of data are in agreement within each other for water saturations above 38%.

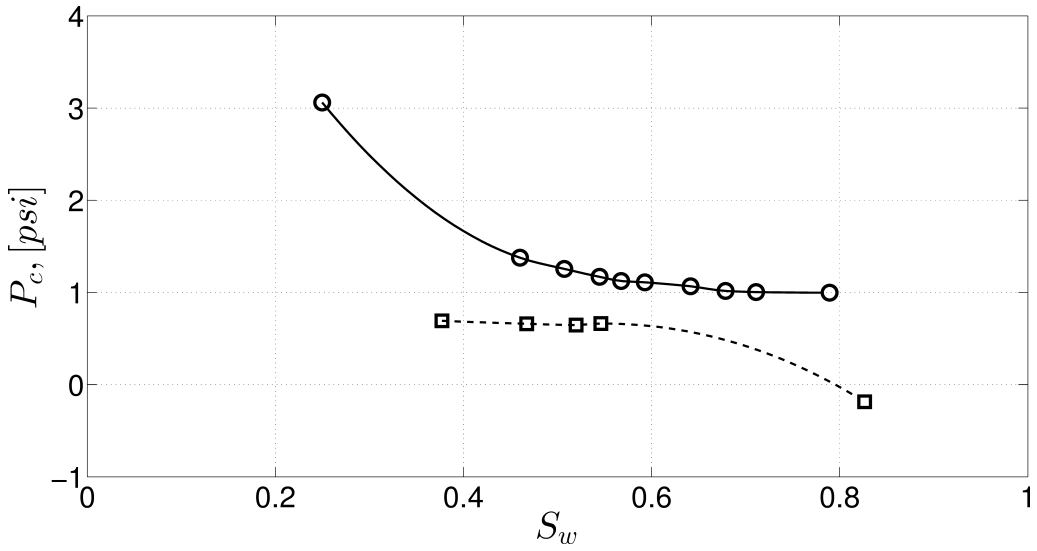

Figure 3.11: Capillary pressure as a function of the sample water saturation. Interpolating polynomial (solid line) of the computed data for drainage (∘ symbol) and interpolating polynomial (dashed line) of the computed data for imbibition (□ symbol).

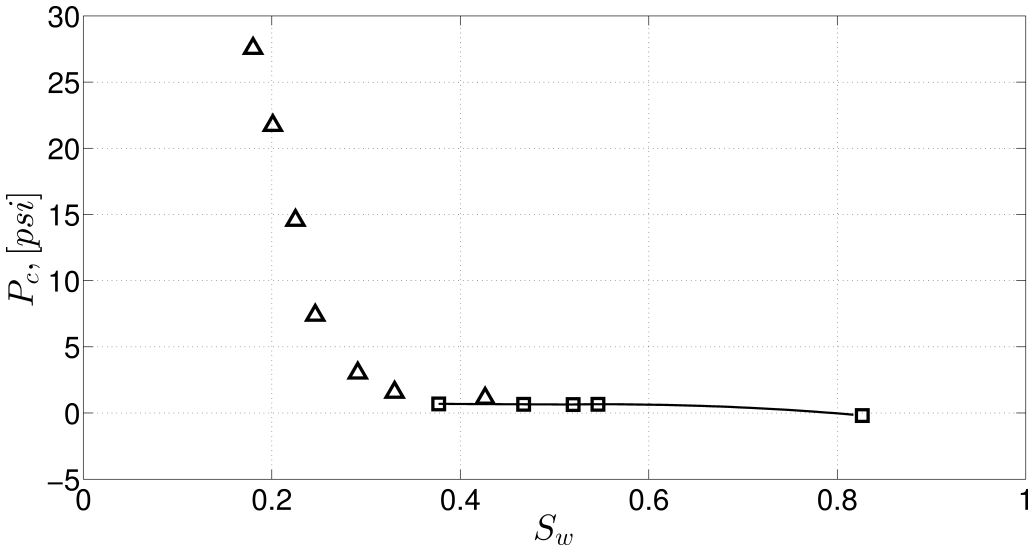

Figure 3.12: Capillary pressure as a function of the sample water saturation. Experimental data (△ symbol) and interpolating polynomial (solid line) of the computed data for imbibition (□ symbol).

3.5 Conclusions

The use of commercial CFD softwares to compute the relative permeabilities and the capillary pressure of a porous sample, paves the way to the diffusion of numerical methods for petro-physical computing, the standardization of the digital rock workflow and the reproducibility of numerical results.

A large number of benchmarks are published in the literature showing the adherence between laboratory and simulated multiphase experiments. Here the remarkable capabilities of a well-established commercial FV-VOF solver ANSYS-Fluent®, supported by a rigorous post-processing of the numerical output data, are demonstrated. However a number of free open source CFD packages exists for multiphase simulation, e.g. OpenFoam (http://www.openfoam.com/). In general, the reliability of the entire digital rock physics workflow is founded on the use of a representative elementary volume. A 200^3 voxels volume turned out to be a REV for porosity and absolute permeability, thus it is considered appropriate for the procedure of relative permeability and capillary pressure estimation. Undoubtedly one can foresee that larger tomographic volumes (e.g. 1000^3 voxels or more) are amenable to be processed and ensure more reliable results, provided that adequate computational resources are available (a 1000^3 voxels volume with porosity 12% has 120 million

cells).

The numerical approach here adopted is capable to model the physical process in which one or two immiscible fluids are co-injected and displace the fluid that initially occupies the pore space. The procedure uses the full morphology of the rock as reconstructed by X-ray CT. According to the available literature, the use of a traditional CFD model for two-phase flow simulations at pore-scale is an original contribution of the present work and represents a promising tool for future exploitation. The key strength of the proposed workflow is the CFD employment for estimation of parameters, such as capillary pressure and relative permeability, traditionally derived by means of time-costing and invasive laboratory experiments, here estimated via direct numerical simulation.

Relative permeability and capillary pressure curves are calculated according to the so called *steady-state* protocol. All the microscopic variables are up-scaled, in order to mitigate the local fluctuations of pressure and velocity fields. The relative permeability k_r of each phase is computed via Darcy's law where the oil pressure drop and the water pressure drop are computed separately rather than taking the mixture as a whole. The capillary pressure P_c is estimated via macroscopic approach, where the phase pressure is computed as an intrinsic volume-averaged pressure. On the whole, the numerical results are in agreement with the experimental results, except for the oil relative permeability curve, for which a disagreement between the two sets of data is undeniable. There may be various causes of this discrepancy, which could be ascribed, first of all, to the different dimensions of the samples used for the characterization: a one inch in diameter core plug for the laboratory experiment and a 200^3 voxels cube of side 0.9 mm for the numerical simulations.

The procedure, adopted in a drainage displacement, is replicated for imbibition allowing to derive the corresponding relative permeability and capillary pressure curves. Surprisingly the hysteresis behaviour is found in both the parameters, suggesting the ability of the proposed numerical workflow to capture the different response of the pore system to either decreasing or increasing wetting phase saturation.

Finally, the threshold capillary pressure is computed following three different and independent strategies that yield comparable results and also in line with samples of similar permeability (Bentsen and Anli, 1977). The continuous monitoring allows to visualize the evolution of the process and highlight local phenomena (fingering, snap-off, coalescence, etc...) occurring within the pore space, that could not be captured with traditional macro-scale laboratory tests.

Chapter 4

Accuracy and reliability of capillary pressure measurements

Capillary pressure in opaque porous media cannot be measured directly. Indirect laboratory measurements rely on a variety of macroscopic methods that monitor the pressure difference between the exposed faces of a porous media sample and can only provide rough estimates. These methods rest on the basic assumption that the capillary pressure can be expressed as a function of the wetting phase saturation, only: $P_c = P_c(S_w)$. Pore-scale effects, such as fluid-fluid interface configuration, contact angle and internal pore space morphology are not accounted for.

On the other hand, numerical methods solve the governing flow equations and give the opportunity to measure flow field properties in every point of the porous domain. The contribution of interfacial forces, viscous forces and wettability is modeled by adequate terms in the momentum equation. The computed properties need to be up-scaled to derive reliable capillary pressure values.

From a *microscopic* point of view, the capillary pressure is defined as the pressure jump across the interface separating the non-wetting and the wetting phases (i.e. oil and water) that occupy the pore space, thus intimately related to the local curvature of the interface between the immiscible fluids in contact.

The *macroscopic* capillary pressure, derived by an up-scaling process from its microscopic, well-defined counterpart, is a quantity of major interest in gas and oil reservoir engineering, as it is a key quantity in controlling the fluid distribution and displacement flow throughout the pore space: P_c versus S_w curves represent a prerequisite in numerical models for the simulation of either primary or secondary gas and oil recovery. Notwithstanding this, the macroscopic approach provides only a partial depiction of P_c and in real displacement processes does not describe thoroughly all the interfacial phenomena.

4.1 Literature review

In a water-oil imbibition displacement, the capillary pressure is related to the pressure difference across the menisci separating oil ganglia from the water phase. Equilibrium or motion of a meniscus in a throat depend on the balance between the local pressure difference and the capillary pressure acting in the pore chambers adjacent to the throat. Payatakes (1982) provided an excellent explanation of dynamics occurring in oil ganglia mobilization in static, quasi-static and dynamic conditions. Several experiments reported by Bear (1972) and Scheidegger (1974) evidenced that during imbibition, as the water advances and the capillary pressure decreases, the non-wetting phase is relegated into larger pores and lastly breaks up into isolated blobs. Based on these results and according to the thermodynamic theory proposed by Leverett (1941) and Morrow (1970), Hassanizadeh and Gray (1993) state that P_c is an intrinsic property of the system, dependent on a change of interfacial free energy associated to a change in saturation. They developed a model whose key concept is that P_c can be considered as function of saturation of the wetting phase and the specific interfacial area of the non-wetting phase (area of the non-wetting phase interface per unit volume of the porous medium). More recently, the rate of change in saturation has been proved to have dynamic effects on capillary pressure (O' Carroll et al., 2010). All these studies suggest that an univocal definition of capillary pressure is pretentious and its estimation cumbersome.

Given the impossibility of measuring P_c directly, in reservoir characterization practice traditional core-flooding experiments are used. Discrepancies between the measurements obtained by various standard laboratory techniques (mercury injection, porous plate technique and centrifugation) have been observed (Wilson and Tjetland, 2001). The traditional porous-plate technique is considered the most reliable but takes several weeks to span the entire P_c curve at ambient condition. The use of layered ceramic porous-plates reduces the time required for a complete capillary pressure experiment, since it overcomes the problem of flow restrictions through the plate (Wilson and Tjetland, 2001). The alternative membrane technique allows for the continuous injection and produces a full suite of drainage-imbibition capillary pressure curves in a tenth of the time required for conventional methods (Ezewu et al., 2013). The semi-permeable membrane offers the possibility to produce selectively one fluid: a hydrophobic membrane is placed at one-end and a hydrophilic membrane at a second-end of the core sample.

Intense ongoing research focuses on faster and more reliable indirect measurement techniques of P_c (Armstrong et al., 2012; Andrew et al., 2014a; Meakin and Tartakovsky, 2009). In an advanced petro-physical laboratory, high-resolution X-ray computed tomography is routinely used to reconstruct the three-dimensional map of fluids occupying the pore space of permeable reservoir rocks undergoing flooding experiments.

Armstrong et al. (2012) and Andrew et al. (2014a) infer P_c from the tomographic three-dimensional maps of the fluids at rest. Armstrong et al. (2012) use synchrotron tomographic volumes of sub-millimetric packed glass spheres to study capillary phenomena and to evaluate the possibility of estimating P_c via curvature. A tomographic spatial resolution of 13 microns is adopted. A sequence of primary and secondary floodings is carried out and measurements are made once both fluids have reached a complete equilibrium. The pore-scale computed P_c is compared to macro-scale capillary pressure measurements carried out with transducers placed in the fluid lines above and below the porous sample. In the experiments where a sufficient equilibration time is conceded to the fluids, a relative error of 10% for imbibition and 20% for drainage is attained. The authors recognize that "*it is critical to understand how well transducer measurement values represent pore-scale interfacial curvature*".

Andrew et al. (2014a) use micro-tomographic data produced with a cone beam source at 2 and 3.5 microns of spatial resolution. Their interest is in CO_2 pore-trapping mechanisms in limestone rocks. They find little effect of voxel coarsening from 2 to 4 micron voxel side on curvature estimation. They also find little effect of amount of isosurface smoothing iterations, due to the magnitude of principal radii of curvature respect to voxel size. Moreover Andrew et al. (2014a) provide a new definition of capillary number based on the curvature-derived P_c.

4.2 Purpose of the study

In the previous chapter, we demonstrated that the relationship between P_c and final fluid saturation can be also computed by pore-scale numerical simulation of immiscible fluid displacements in the full morphology of a porous medium as reconstructed via high-resolution X-CT. The computation involves the use of CFD codes to mimic the flooding through the X-CT highly-resolved pore space.

A rather innovative and alternative method is to use high resolution X-ray tomography to visualize the fluid-fluid interfaces within the pores and to calculate their local mean curvature. This, in turn, allows to estimate the microscopic capillary pressure via the Young-Laplace equation.

We apply this indirect method to process experimental data acquired with a X-ray cone-beam laboratory station and numerical data of pore-scale numerical simulations carried out with a high-resolution computational mesh. Both the cases refer to an imbibition displacement, for which the trapped oil ganglia are analyzed one-by-one. Experimental and numerical P_c results are compared. Moreover we critically reconsider some aspects of the approach proposed by Armstrong et al. (2012) and Andrew et al. (2014a). We intend to highlight the key points of the proposed method and focus on the following items:

(i) Influence of mesh refinement on curvature estimation.

(ii) Extent of errors inherent in the numerical procedure.

(iii) Suitability of the method in computing the curvature under dynamic conditions.

(iv) Comparison of P_c values calculated from pressure field output data of numerical simulation with curvature-based P_c values.

(v) Comparison of curvature-based P_c values of experiments with those of the simulated case.

4.3 Materials and methods

4.3.1 Experimental procedure

The experimental procedure follows the main steps detailily described in Section 2.1.4. Briefly:

1. CO_2 is injected into the sample to displace all the air trapped in the system.
2. PRIMARY IMBIBITION. Brine (solution of water and KI salt) is injected upward for 50 PV until total saturation is achieved.
3. PRIMARY DRAINAGE. Oil (hexadecane) is injected downward at a flow rate of 0.2 ml/min and the pressure drop is monitored to ensure the attainment of stationary condition.
4. SECONDARY IMBIBITION. The sample is reflooded with brine at a flow rate of 0.2 ml/min, in order to displace most of the oil occupying the pore space. Brine injection is stopped once a constant pressure drop across the sample is observed.

The fluid injection flow rate in the core flooding experiments produces an interstitial velocity of 0.02 cm/s . The corresponding pore Reynolds numbers are, respectively, 4.2×10^{-5} and 1.5×10^{-4} for primary drainage and secondary imbibition. The numerical simulations are carried out at a higher interstitial velocity: this is common practice in order to reduce the computational time that is in any case of the order of weeks on a state of the art computer work-station.

The specimen (SAMPLE 1) is tomographed with the nanofocus cone-beam CT system (Nanotom) available at the Delft Unversity of Technology, whose technical specifications are reported in Section 2.1.2.

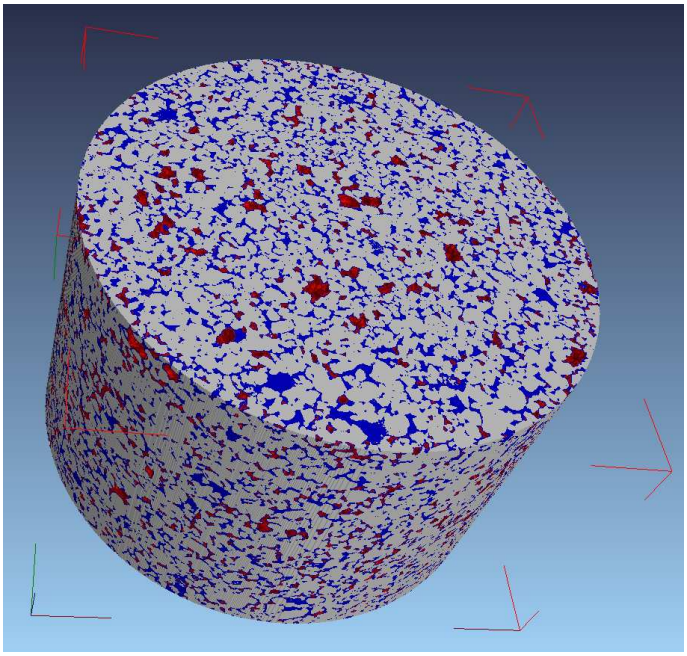

(a)

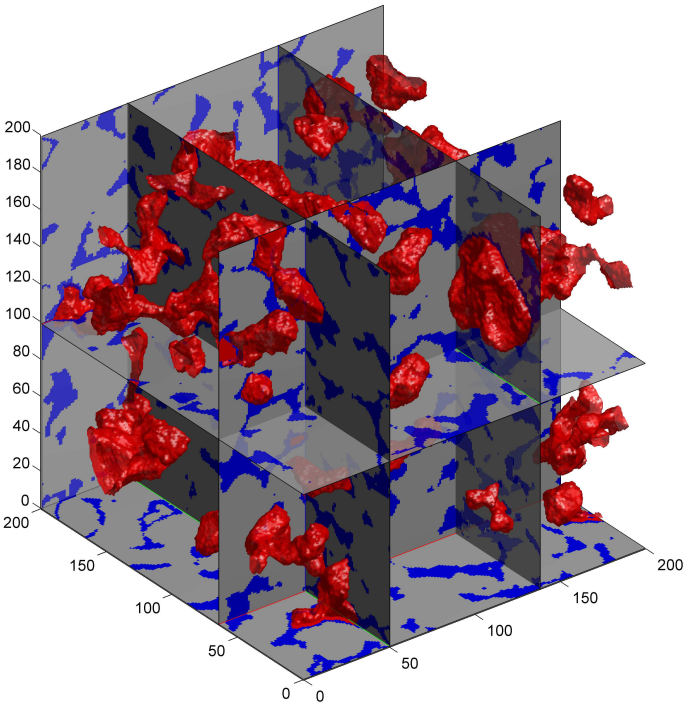

(b)

Figure 4.1: (a) Map of fluid distribution in the full tomographic volume, oil in red, brine in blue and rock in grey. (b) Ortho-slices of the fluid map segmented from a tomographic sub-volume. Voxel size is 7 μm.

The full tomographic acquisition is gained by placing the sample undergoing scanning on a high precision rotating stage, which is rotated by small angular steps while a radiographic operation is repeated at each step. The number of projections taken around a full 360 degree rotation of the core sample complies with the Nyquist sampling principle, in order to avoid under-sampling and induced artifacts. The Nyquist principle, applied to tomography, states that the minimum number of projections required for a truthful reconstruction has to be $N = (\pi\, D)\,/2$, where D is the sample diameter in pixels. The tomographic reconstruction uses the standard filtered back projection (FBP) software, which the Nanotom is provided with and is based on the FDK algorithm (Feldkamp et al., 1984). Beam hardening and ring artifacts are also corrected with routines available from the same hardware maker.

Prior flooding, the dry core plug is tomographed at a resolution of 2.5 μm in order to generate a very high-resolved mesh suitable for CDF simulations. To obtain the desired resolution the specimen is moved closed to the source and a magnification factor (ratio between object-to-detector and source-to-object distances) of 20 is achieved. Once the flooding is completed and the time needed for fluid stabilization has passed, the sample is scanned at a resolution of 7 μm and the reconstructed fluid maps are used for subsequent curvature studies.

Figure 4.1(a) shows the entire tomographic volume, where oil is visualized in red, brine in blue and the rock matrix in grey. A three-dimensional, magnified view of a sub-volume of the sample is visualized in Figure 4.1(b): it is evident that oil tends to occupy the central portions of the pores due to the water-wet nature of the rock.

4.3.2 Numerical estimation of surface curvature

Generalities

The numerical calculation of the curvature of a tessellated surface, originating from experimental data, is not a trivial task, as it implies approximating the second derivatives of the surface's representation (either implicit or parametric) and because the original data may be corrupted by noise. Noise reduction is usually attempted by *smoothing* the tessellated surface, i.e., by relocating its vertices according to suitable algorithms. Over-smoothing may adversely affect the calculation of curvature.

In this section we briefly recall and test some of the commonly used algorithms for calculating the curvature of triangulated surfaces and some techniques for the mitigation of the curvature noise due to low mesh quality.

Let us consider a regular surface Σ in three-dimensional space and a point $P \in \Sigma$ on it. The surface admits a normal N_P and a tangent plane T_P. Letting $\boldsymbol{u} \in T(P)$ be a unit vector tangent to the surface, we may define a plane $\Pi_{\boldsymbol{u}}$ as generated from vectors N_P and $\boldsymbol{u}$. The principal curvatures λ_{max} and λ_{min} of a surface Σ at

P may be defined as the maximum and minimum curvatures among all intersection curves $\delta_{\boldsymbol{u}} \equiv \Sigma \cap \Pi_{\boldsymbol{u}}$. Using a local coordinate system (x, y, z) where x, y lie on T_P and z is parallel to N_P, a parametric representation of Σ in a neighborhood of P is $(x, y, h(x, y))$. The signed, normal curvature $\kappa_{\boldsymbol{u}}$ of $\delta_{\boldsymbol{u}}$ at P is given by (Kreyszig, 1991):

$$\kappa_{\boldsymbol{u}}(x = 0, y = 0) = \frac{\partial^2 h}{\partial x^2}\, u_x^2 + 2\,\frac{\partial^2 h}{\partial x\,\partial y}\, u_x\, u_y + \frac{\partial^2 h}{\partial y^2}\, u_y^2 \tag{4.1}$$

so that the maximum and minimum values of $\kappa_{\boldsymbol{u}}$ are the eigenvalues of the hessian matrix $H(x, y)$ of $h(x, y)$ at $(x, y) = (0,0)$. The *mean* and *Gaussian* curvatures of Σ at P, κ_M and κ_G, respectively, are defined as:

$$\kappa_M \equiv \frac{\lambda_{min} + \lambda_{max}}{2}; \quad \kappa_G \equiv \lambda_{min}\,\lambda_{max} \tag{4.2}$$

Patch-fitting methods calculate analytically the curvature of local polynomial approximations Σ_P to a tessellated surface in a neighborhood of each vertex P. In the following, only two specific polynomial approximations are considered, namely:

$$z = a\,x^2 + b\,x\,y + c\,y^2 \qquad \text{method PF3} \tag{4.3}$$

$$z = a\,x^2 + b\,x\,y + c\,y^2 + d\,x + e\,y + f \qquad \text{method PF6} \tag{4.4}$$

The free parameters in (4.3) and (4.4) are determined by least-squares minimization of the normal distance between the polynomial approximation and the tessellated surface at the vertices surrounding a given vertex P. Rings of neighbour vertices are selected at once: ring-1 vertices are incident to node P; ring-2 vertices are incident to ring-1 vertices; and so on. In the considered implementations of the Patch Fitting algorithm the number of rings is selected dynamically, so as to provide a sufficient number of neighbour vertices to yield an over-determined least-squares approximation. It is well-known that widening the influence region of a vertex bears a sort of smoothing effect on the calculated curvature (Rusinkiewicz, 2004). Eventually, the principal, mean and Gaussian curvatures of the approximated surface at the target node are calculated by (4.1) and (4.2).

The tensor-averaging method (Rusinkiewicz, 2004) (henceforth identified as TA) is based on a finite-difference approximation of the Second Order Fundamental Tensor on the facets, followed by a weighted average onto the vertices from the surrounding facets. It is worth remarking that the TA method yields exact curvature at each vertex of a tessellated sphere.

The numerical calculation of curvature is very sensitive to the quality of the triangulated surface. In order to reduce the amount of high-frequency noise a Mean Curvature Flow filtering procedure (MCF hereafter) is adopted (Yagou et al., 2002; Langer et al., 2005).

Further issues on local curvature estimation

The robustness of the combined numerical procedure yielding the curvature of a tessellated surface is assessed by carrying out several numerical experiments.

An approximately uniform triangular tessellation of a unit sphere is generated by minimizing the generalized electrostatic potential energy of a system of charged particles (Semechko, 2015). The considered tessellated surface is topologically closed with 200 vertices. The mesh quality is defined in terms of the Condition Number Shape Measure (Garimella et al., 2004) and ranges between 0.75 and 1. Prior evaluating the curvature a MCF smoothing (Yagou et al., 2002) operation is applied, with different numbers of iterations (0 iterations means no smoothing). The number of mesh nodes is progressively increased from 200 to 5000.

It is verified that the TA method yields exact results for this particular case. The curvature estimate provided by the PF3 and PF6 methods improves with increasing mesh resolution, with superior accuracy for the PF3 method on the coarsest meshes and comparable accuracy on the finest considered meshes.

Also it turns out that the Condition Number Shape Measure is capable of identifying regions where the curvature approximation is not accurate. Smoothing alters significantly this framework, as the shrinking-volume effect yields higher curvatures, though the quality of the tessellation is not sensibly affected. After 20 smoothing iterations the sphere's surface becomes wobbling and the sphere is shrunk significantly: the 2-norm error (unweighted) of the Gaussian curvature at the vertices, calculated with algorithm TA, is as high as 65.5%.

In addition, the 800 vertices used to represent a tessellated unitary sphere are displaced radially by adding a uniformly distributed random noise (St. Dev. = 0.03). Different numbers of MCF smoothing iterations are applied to the tessellated sphere prior to evaluate the curvature. It turns out that increasing the number of smoothing iterations up to an upper limit improves the results as the high-frequency noise is filtered out. However, beyond this limit (approximately 20 iterations with the TA algorithm) over-smoothing deteriorates the results.

4.3.3 Volume filtering and segmentation

The surface curvature is estimated considering the oil ganglia trapped within the pores at the end point of an imbibition process. The whole procedure requires high-resolution spatial data, where solid and fluid phases can be easily identified. The full tomographic volume of the inspected rock sample is obtained by stacking the slices reconstructed via FBP of the radiographic projections collected at the detector. The parameter-free median filter with a neighbour window $3 \times 3 \times 3$ is used to remove digital noise. The median filter preserves edges and does not erode small structures in the image. It replaces each voxel luminosity by the median of

luminosity of the 27 surrounding voxels. The resulting histogram of voxel luminosity presents distinguishable peaks and valleys and it is suitable for the selection of two thresholds for a region-based segmentation of wet volumes containing oil or doped water (brine) in the pore space, as shown in Figure 4.2.

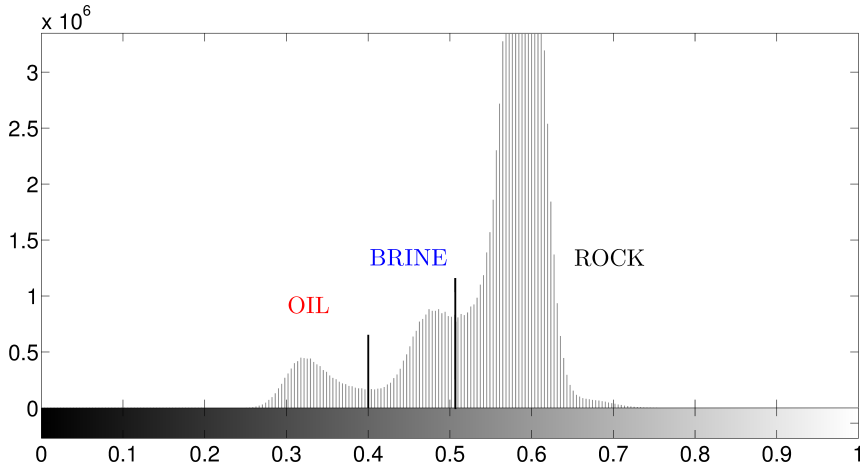

Figure 4.2: Histogram of voxel luminosity for a three-phase oil-brine-rock system.

The continuous luminosity field is segmented and converted into a discrete, three-level field used for morphological measurements of the pore space and enclosed fluids. The labelled oil volumes are identified one-by-one and their bounding box is used to isolate the corresponding gray level volume from the filtered tomographic volume. This sub-volume is then used to extract a triangulated isosurface of the oil ganglion. The isosurface extraction method based on the distance map is also adopted for the high-resolution digital volume used for fluid-dynamic simulation. In this case, the volume fractions α, identifying the presence of one or both fluids in a void voxel, are used to separate one-by-one oil ganglia from the connected water phase. A standard marching cubes algorithm is employed to extract the surface mesh (Figure 4.3(a)), while a surface-smoothing algorithm is adopted to remove the high-frequency noise (Figure 4.3(b)).

It is verified that the mesh extracted from the map of linear attenuation of the materials traversed by the X-rays, i.e., a three-dimensional gray-scale map, is locally smoother than a mesh extracted from binary segmented volumes, thus more suitable for curvature calculations. This finding is corroborated by the diagram of Figure 4.4 reporting the relative error on the numerically computed curvature for a triangulated sphere. The sphere is extracted from a binarized volume (green curve) and from a real value distance map (blue curve). There is a sensible lower error when the sphere is extracted from real data. This is done for a series of spheres of different resolution and size, i.e., number of voxels per sphere radius.

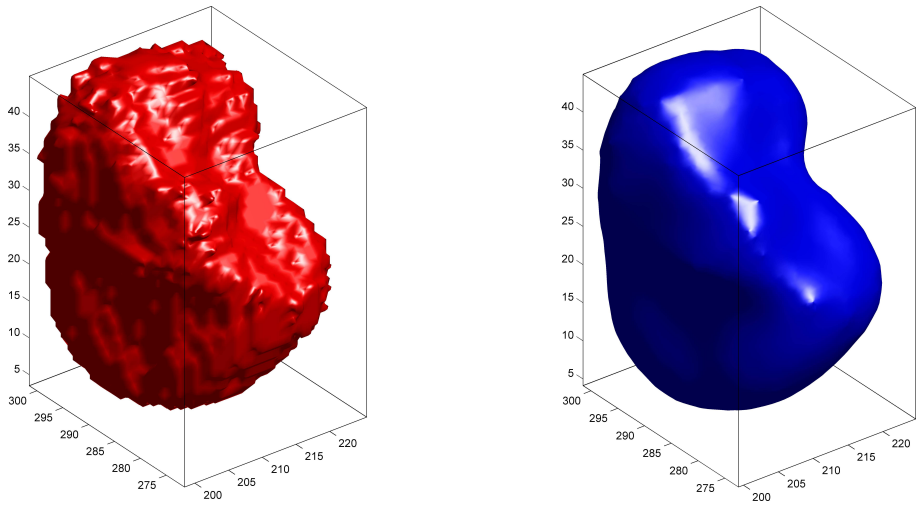

(a) (b)

Figure 4.3: Ganglion isosurface, as extracted (a) and after smoothing (b).

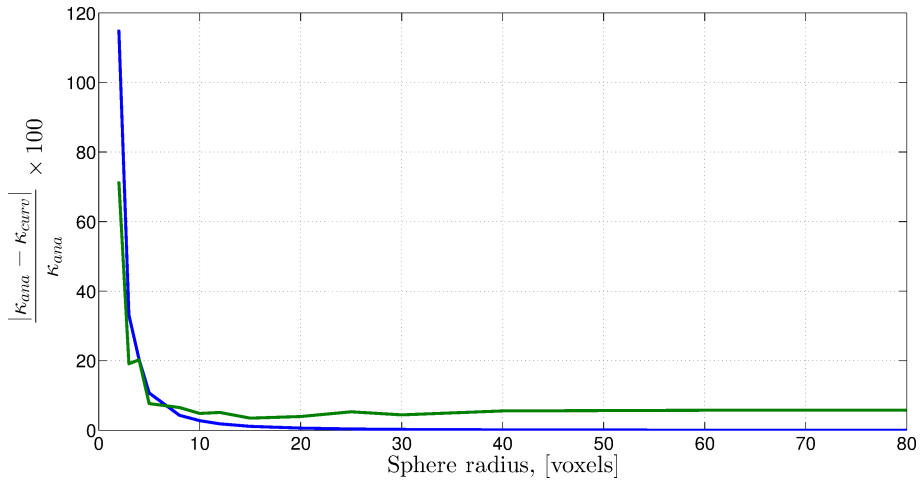

Figure 4.4: Relative error in curvature estimation of a binarized sphere (green line) and of a sphere extracted from a 3D real value distance map (blue line).

Examples of a curvature-mapped triangulated isosurface of a sphere are visualized in Figures 4.5 and 4.6. In Figure 4.5 the left-hand sphere has a resolution of 8 voxels/radius, the right-hand a resolution 100 voxels/radius. The surface generated in the coarsen mesh exhibits κ_M values more dispersed than those calculated for the refined mesh: the standard deviation of κ_M distribution is 0.0061 and 6.4185 $\times 10^{-5}$ for the low-resolution and high-resolution meshes, respectively.

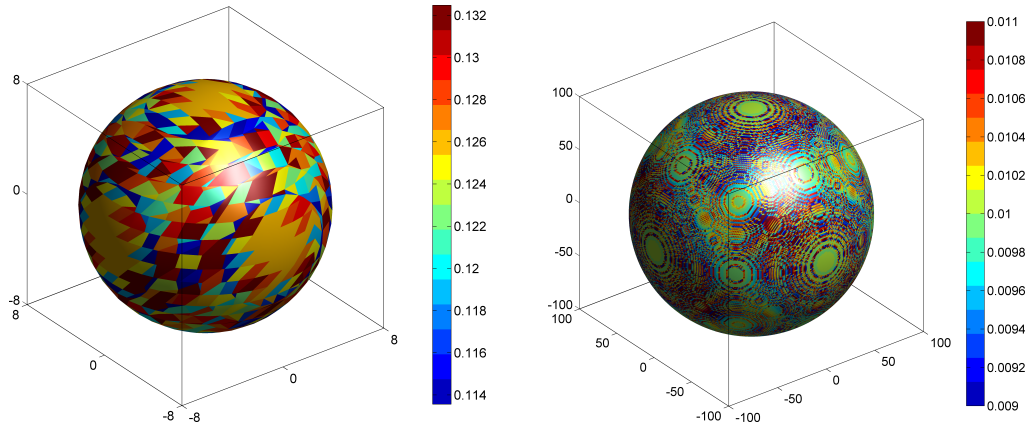

(a) (b)

Figure 4.5: Effect of resolution on curvature estimation. (a) Curvature map of a 8-voxels-radius sphere ($\kappa_{ana} = 0.125$, $\bar{\kappa}_M = 0.126$, St. Dev = 0.0061). (b) Curvature map of a 100-voxels-radius sphere ($\kappa_{ana} = 0.01$, $\bar{\kappa}_M = 0.01$, St. Dev = 6.4185 $\times 10^{-5}$).

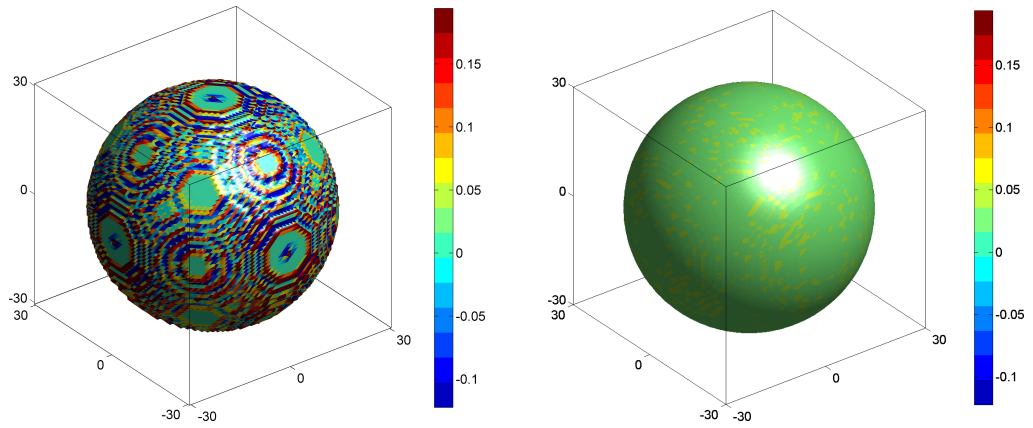

(a) (b)

Figure 4.6: Effect of isosurface extraction method on curvature estimation. (a) Curvature map of a 30-voxels-radius sphere extracted from a binarized volume ($\kappa_{ana} = 0.0\overline{3}$, $\bar{\kappa}_M = 0.0315$, St. Dev = 0.0977). (b) Curvature map of a 30-voxels-radius sphere extracted from a distance map ($\kappa_{ana} = 0.0\overline{3}$, $\bar{\kappa}_M = 0.0\overline{3}$, St. Dev = 0.0021).

In Figure 4.6 the isosurface extracted from a binarized sphere (left-hand) is compared to that extracted from a distance map (right-hand), thus naturally "smooth". The maps of both cases are visualized in the same range of mean curvature values. The standard deviations of κ_M distribution are 0.0977 and 0.0021, respectively. Figure 4.7(b) shows the surface of a ganglion colored with the value of the local curvature. Convexity is identified by positive values. In general surface-smoothing removes high frequency noise, yielding lower absolute values of the surface-averaged mean curvature. Figure 4.7(a) shows the portion of the closed surface which is non in contact with the solid matrix. The ganglion curvature used for capillary pressure calculation, by means of the Young-Laplace equation, is averaged on this portion.

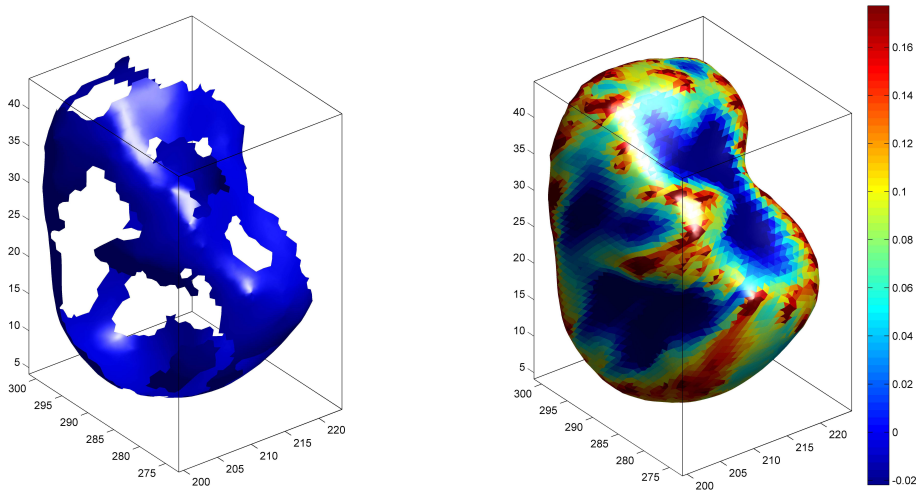

(a) (b)

Figure 4.7: (a) Portion of the ganglion isosurface not in contact with the porous matrix material and (b) isosurface coloured with the magnitude of the curvature.

4.3.4 CFD simulations

Given the mentioned impossibility of measuring P_c directly, at a pore-scale level, a CFD study is undertaken on a 300^3 voxels sub-volume of the same Bentheimer sandstone sample shown in Figure 4.1. To this end, as stated above, the rock sample is tomographed at higher resolution (2.5 μm versus 7 μm). The aim of the CFD study is to link two independent strategies of capillary pressure estimation. Indeed, the capillary pressure is calculated both as the difference between the phase pressure fields and as the pressure jump determined by the local mean curvature at the fluid-fluid interfaces. The commercial computational fluid dynamics (CFD) software ANSYS FLUENT® is used to simulate the multiphase flow in the 3D meshed

pore space. The CFD solver is used to mimic a pore-scale single-phase flow, as well. The absolute permeability computed in three orthogonal directions (k_x = 3.48 Darcy, k_y = 2.77 Darcy, k_z = 1.89 Darcy) reveals a slight anisotropy of the considered digital volume, although the values are of the same order of magnitude of the experimentally obtained k (3.20 Darcy).

The boundary conditions for two-phase flow simulation are: *velocity inlet* and *pressure outlet* at inlet and outlet sections, respectively; *no-slip* condition and *wall-adhesion*, specified through the static contact angle between oil and brine, at the rock/pore interface.

The properties of the fluids (brine and oil) employed in the numerical experiments are imposed in conformity to those measured with specific laboratory tests:

$$\begin{aligned} \rho_b &= 1069.3 \ \text{kg/m}^3 \ ; & \gamma_b &= 1.203 \times 10^{-3} \ \text{kg/m} \cdot \text{s} \\ \rho_o &= 777.2 \ \text{kg/m}^3 \ ; & \gamma_o &= 3.205 \times 10^{-3} \ \text{kg/m} \cdot \text{s} \\ \sigma_{o,b} &= 0.04 \ \text{N/m} \ ; & \theta_s &= 40^\circ \end{aligned}$$

where ρ and γ are the density and dynamic viscosity of the fluids, $\sigma_{o,b}$ is the oil/brine surface tension and θ_s is the static contact angle. The surface tension $\sigma_{o,b}$ and the static contact angle θ_s are specified in reference to the recent studies of Rezki et al. (2013) and Yang et al. (2008) on oil/brine systems.

Oil is injected within the brine-saturated sample, to replicate a primary drainage. At irreducible brine saturation, the drainage is stopped and brine is forced to penetrate the pore space, mimicking a secondary imbibition. The sequence of images in Figure 4.8 shows the evolution of the oil phase during the simulated drainage.

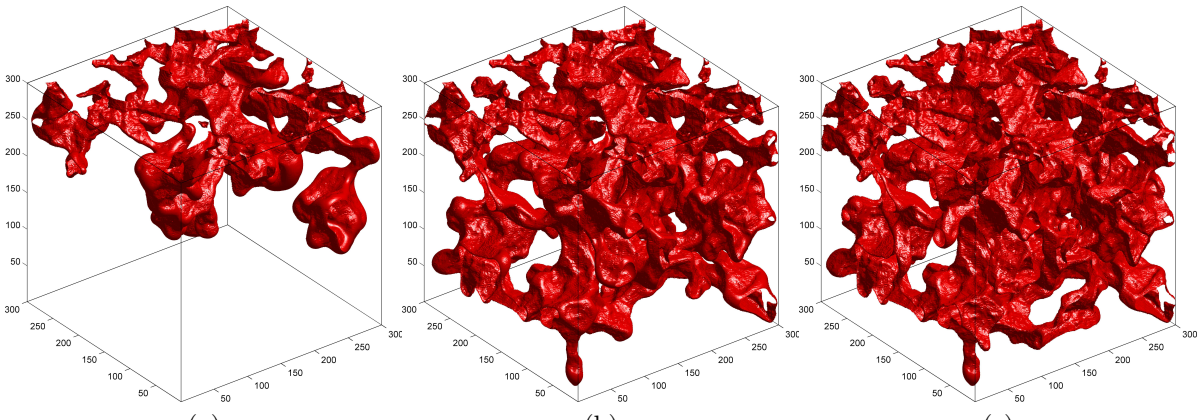

(a) (b) (c)

Figure 4.8: Three consecutive stages in the oil phase front evolution during the drainage displacement. Brine is not shown.

Once the residual oil saturation is attained, the brine injection is discontinued and *no-slip* (i.e., *wall*) conditions are imposed on both inlet and outlet sections in order to keep the saturation constant. The achievement of a stationary equilibrium condition is witnessed by the continuous decrease of the fluid's kinetic energy, from 1.82×10^{-11} J to 1.12×10^{-19} J. The capillary number (ratio between viscous and capillary forces), diminished in value from 1.60×10^{-3} to 5.46×10^{-8}, is also used as a parameter for stabilization control.

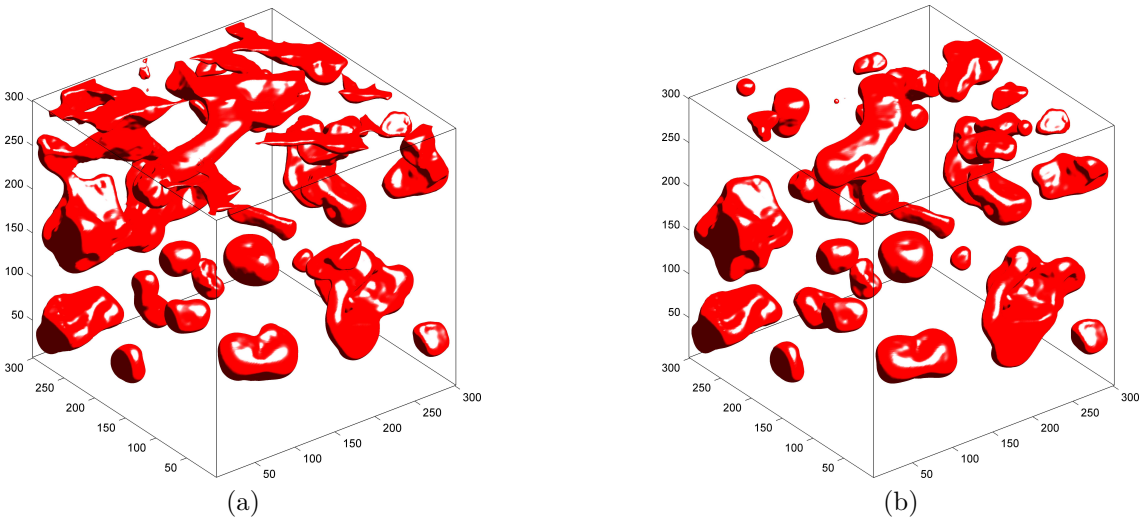

Figure 4.9: Effect of stabilization on oil ganglia distribution and shape. Dynamic case (a) and stabilized case (b).

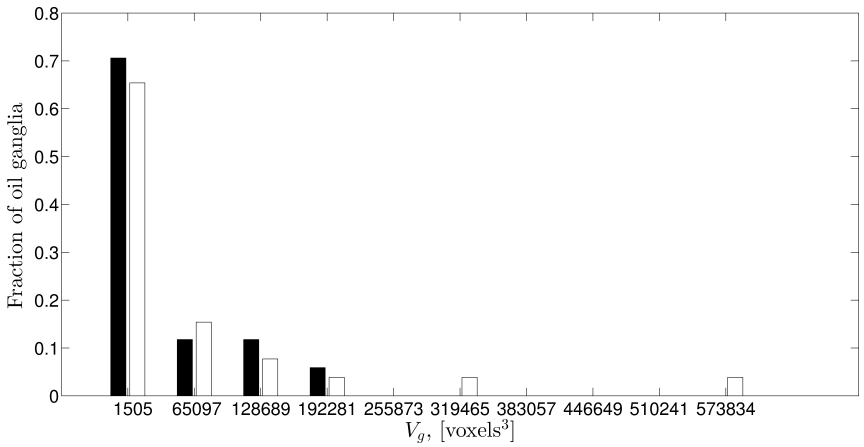

Figure 4.10: Distribution of oil ganglia volumes extracted from the simulated domain during the displacement process (white bars) and at the end of stabilization (black bars).

The stabilization process is characterized by the tendency of oil bodies to become more spherical and by trapping phenomena, such as snap-off, whereby the oil bubble interface becomes unstable and ruptures. The oil ganglia distribution in dynamic and equilibrium conditions is shown in Figure 4.9. The stabilization process leads to an increase of the total number of ganglia (from 26 to 34), particularly the number of small volume bodies. Figure 4.10 reports the normalized histograms of oil ganglia volumes extracted from a simulated imbibition process, in dynamic (white bars) and equilibrium (black bars) conditions.

In Figure 4.11 a two-dimensional section of the phase map shows the water and oil occupation of the pore space as computed by CFD simulations. The interface smearing is limited to no more than three voxels. The corresponding pressure distribution in Figure 4.12 demonstrates that the pressure jump across the surface of ganglia takes place over a wider distance, while the oil pressure within each ganglion is rather uniform. The oil pressure at the fluid-fluid interface is therefore approximated by the mean oil pressure within the entire ganglion. With this strategy, we do not need to compute local oil pressure values at the interface vertices by interpolating pressure data from the neighboring vertices, a process that somehow lacks of objectivity due to the inherent smearing of the simulated fluid-fluid interface. Once a stationary equilibrium condition is attained, brine forms a continuous connected fluid network and the pressure within the brine phase is uniform throughout the sample. In view of the above, the P_c for the individual ganglion is computed as difference between the mean oil pressure in the ganglion and the mean brine pressure in the whole sample. As visible in the companion Figure 4.11 and Figure 4.12, the oil pressure within the ganglion is higher than the pressure in the surrounding brine phase and the oil tends to occupy the central part of the pores.

Inevitably, oil ganglia adapt their shape to the pore space. For an individual ganglion in equilibrium, the interface mean curvature κ_M - on the surface patches where it is not forced to adapt its shape to the boundaries of the solid matrix - is the same over the whole ganglion. This curvature is related to the pressure jump across the interface (ΔP) by means of the well-known Young-Laplace equation, which can have the following form:

$$\Delta P = 2\,\sigma_{o,b}\,\kappa_M \tag{4.5}$$

The choice of the method employed to calculate the pressure difference from pressure field data, is corroborated by the results of a numerical test on an oil spherical bubble surrounded by water in a 90^3 voxels^3 cubic domain. At the six faces of the cube the *wall* condition is imposed. No external pressure is enforced, so that the bubble undergoes a spontaneous equilibrium between the force generated by the internal pressure field and the interfacial force due to the oil/water surface tension. Oscillations of the interface produce remarkable perturbations on the pressure field, which tends to vanish as the bubble tends to stabilize, as shown in Figure 4.13.

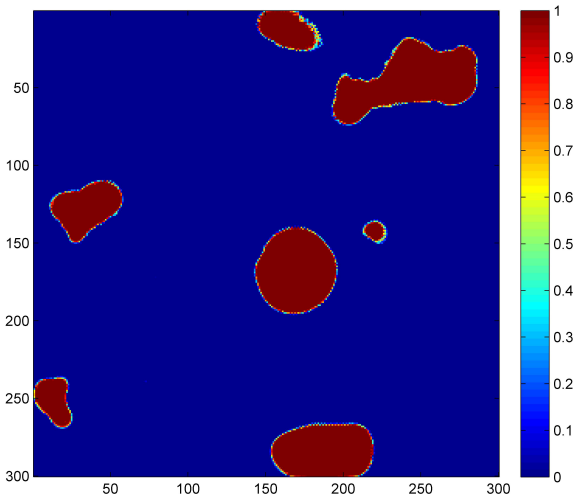

Figure 4.11: 2D oil phase map.

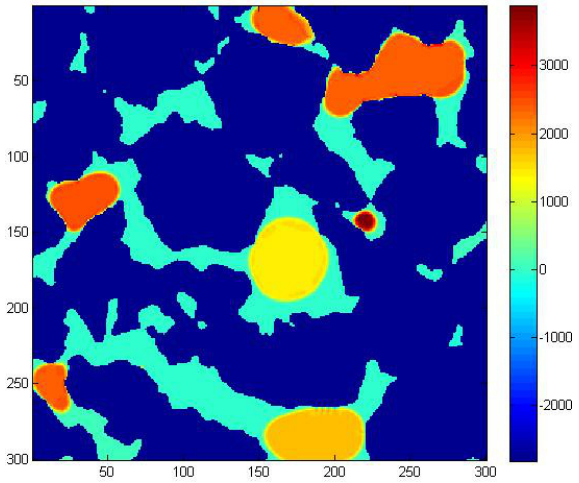

Figure 4.12: 2D pressure map in the fluid phases.

Both the curvature computed on the triangulated bubble surface (geometrical method) and the one calculated via Young-Laplace from the pressure field data obtained with the numerical simulation, are compared to the analytical curvature. The pressure-based curvature is estimated following three different approaches. The first approach (numerical method 1) consists in computing the phase pressure at the vertices of the isosurface by interpolating the pressure data from the neighbouring vertices. The second approach (numerical method 2) computes the phase pressure as an intrinsic volume-averaged pressure in the binarized volume fraction domain, i.e., the oil phase is assigned to voxels with $\alpha_o \geq 0.5$, whereas the water phase is assigned to voxels with $\alpha_o < 0.5$. In the third approach (numerical method 3)

the phase pressure is calculated by averaging the VOF output pressure data in the regions where only the considered phase is contained. The last, among the numerical methods, turned out to be more accurate with a relative error of 2.6% at the ending time. The relative error of the aforementioned methods is plotted in Figure 4.14 as a function of the dimensionless time $t^* = t\sqrt{\sigma_{o,b}/(\rho_o R^3)}$, where R is the sphere radius.

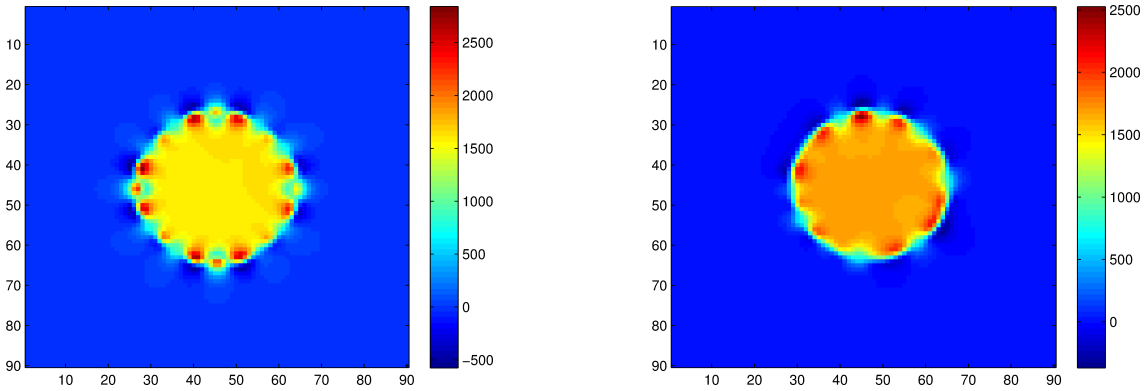

Figure 4.13: 2D pressure map of the oil spherical bubble at initial time (a) and ending time (b).

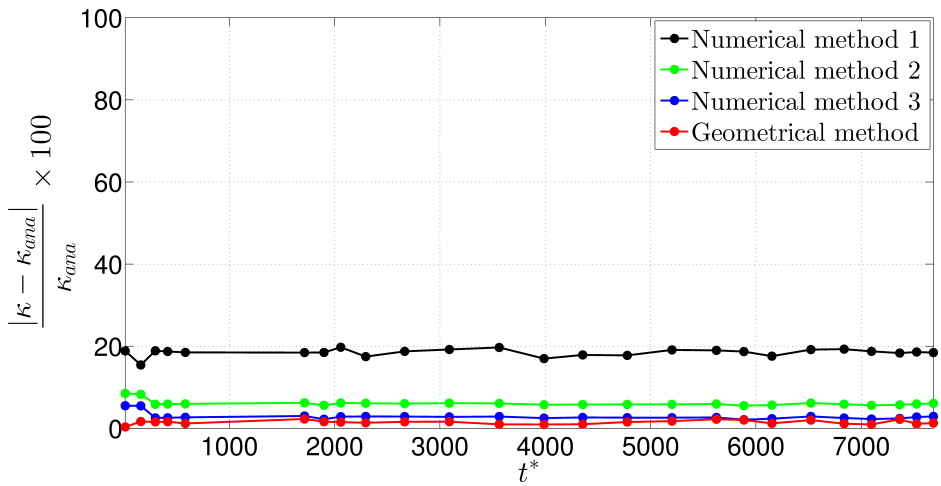

Figure 4.14: Relative error in curvature estimation of the oil spherical bubble.

4.4 Results

In figure 4.15 the abscissa axis reports the P_c derived from the simulation, computed as pressure jump across the fluid-fluid interface. The analytical Young-Laplace relationship (4.5) is also shown as a continuous line. The green square symbols scattered on the diagram refer to the equivalent diameter computed from the averaged mean curvature on each individual ganglion. The red circles refer to the equivalent diameter derived from the ganglion's volume. From the larger spread of the circles, we can deduce that the equivalent diameter computed from the curvature is the most suitable to fit the P_c data.

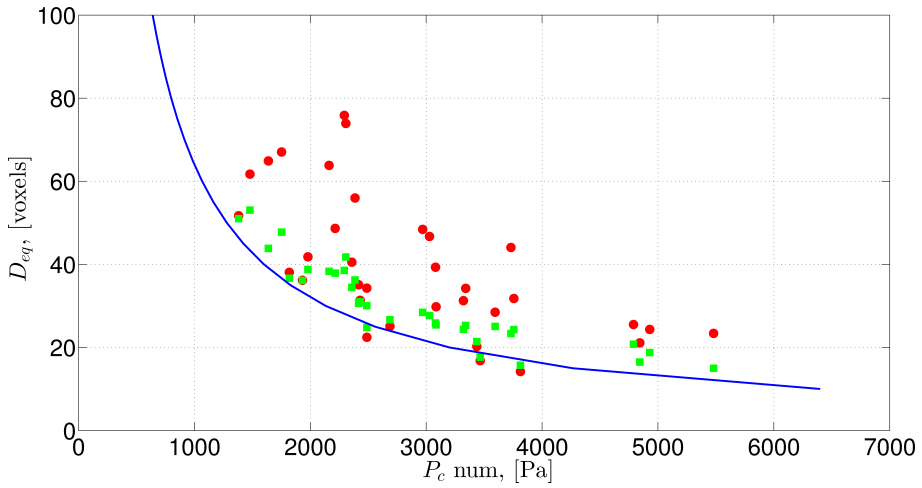

Figure 4.15: Equivalent diameter computed from the ganglion volume (red circles) and from the ganglion surface mean curvature (green squares). The Young-Laplace analytical relationship is also reported (blue solid line).

The diagrams 4.16 and 4.17 display the curvature-based P_c on the ordinates versus the pressure-based P_c of individual ganglia on the abscissas. The ganglia have been previously extracted from the volume, as resulting from two-phase numerical simulation. The size of the circles represents the volume of each ganglion, the color is related to its sphericity (ratio between the surface area of the sphere with the same volume as the non-spherical particle and the actual surface area of the latter) through the shown color-bar. The 45° solid line represents the ideal case of perfect agreement between the two methods of P_c estimation. The two diagrams refer to dynamic and equilibrium conditions. Different numbers of ganglia have been considered in the two cases, since coalescence and breakage phenomena occur during stabilization.

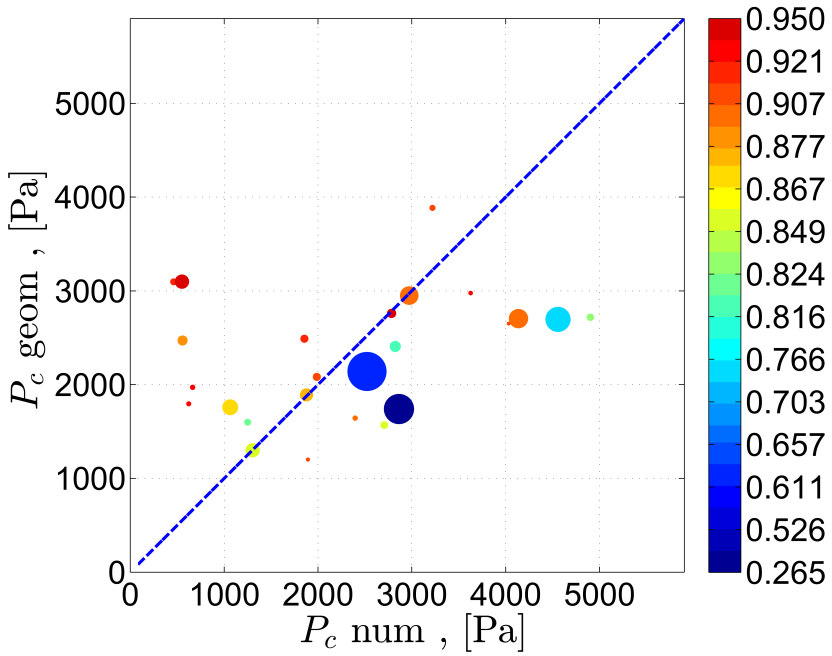

Figure 4.16: Comparison between pressure-based P_c and curvature-based P_c. **Dynamic case.**

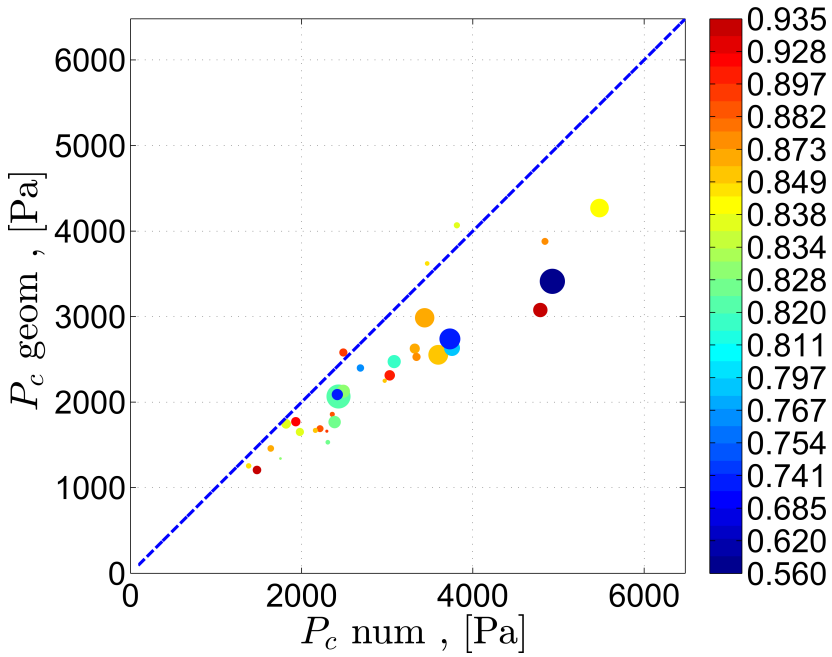

Figure 4.17: Comparison between pressure-based P_c and curvature-based P_c. **Stabilized case.**

One may notice that in the stabilized case the data scattering is remarkably lower than in the dynamic case, though $P_c\,geom$ systematically underestimates $P_c\,num$. As a whole, the capillary pressures evaluated with the two methods are in closer agreement once stability is attained and ganglia volumes become generally smaller (the smallest volume is 4339 voxels^3 and 1505 voxels^3 in the two cases, respectively). It is worth remarking that sphericity and volume of a ganglion are not an indicator of its capillary pressure magnitude. In a not-constricted flow a spherical bubble denotes an equilibrium, minimum free energy condition, for which it may be stated that P_c is strictly related to the radius of curvature by means of the Young-Laplace equation. In a porous medium, fluid flow and ganglia stabilization are deeply bound by the complex morphology of pores and throats where the physical phenomenon takes place. A high sphericity value does not imply a high P_c value, but rather the closeness to a local equilibrium condition of the region in the proximity of the ganglion. Moreover, despite the theoretical assumption stating the inverse proportionality between the ganglion volume and P_c, large ganglia may be characterized by a high P_c, if they occupy more than one pore and the curvature they form entering the adjacent throats is high.

Figure 4.18 reports the normalized histogram of P_c for oil ganglia extracted from a 800^3 voxels experimental tomographic volume that has undergone imbibition (black bars). The P_c on ganglia resulting from CFD simulation is also reported (white bars). These values (see section 4.3.4) are computed on a smaller (300^3 voxels) but higher resolution (2.5 μm) sub-volume of the same rock sample. The statistics on the experimental volume are based on 2480 ganglia, while only 34 ganglia are contained within the computational domain in the stabilized case.

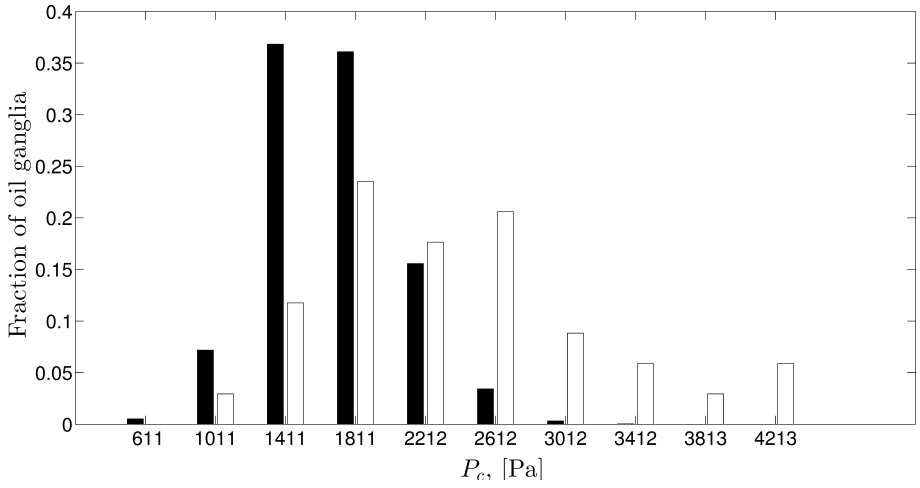

Figure 4.18: Distribution of curvature-based P_c values computed from the tomographic volume (black bars) and from the smaller high-resolution volume (white bars).

The P_c values are comparable in the two cases. The normalized distribution shows a more "clustered dataset" for the tomographic volume, by virtue of the larger set of statistical data available. The surface-area-weighted average capillary pressures computed, on the curvature basis, for the tomographic and the digital volumes are $P_c = 1440$ Pa and $P_c = 1879$ Pa, respectively.

Capillary pressure measurements via laboratory *layered* porous plate experiments on a similar consolidated Bentheimer sandstone sample ($\phi = 0.23$; $k = 1800$ mDarcy) and reported in literature (Wilson and Tjetland, 2001) are shown, as red circles, in the P_c versus brine saturation (S_w) diagram in Figure 4.19. The P_c points computed in this study on a sample from the same rock formation are also marked. The green mark refers to the mean of the P_c values calculated via curvature on the tomographic volume, at $S_w = 0.69$. The blue mark refers to the equivalent value computed via ganglia curvature from the morphology of the fluid interfaces as resulting from CFD simulations, at $S_w = 0.74$. The agreement between the experimental data and those obtained by the combined use of tomography, numerical simulation and curvature analysis is considered extremely good given the degree of reproducibility of these experiments. It should be pointed out that the authors (Wilson and Tjetland, 2001) report that one single experimental point has required tens of days to be produced and that the final equilibrium has been reached 27 days after the beginning of flooding.

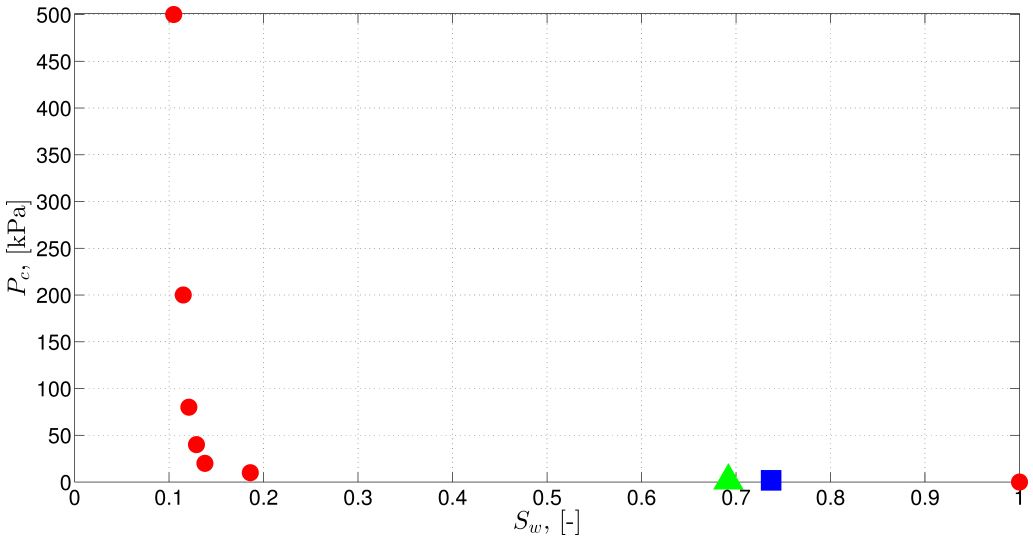

Figure 4.19: P_c measured experimentally via layered porous plate by Wilson and Tjetland (2001) (red circles) compared to P_c computed via interface curvature on the tomographic volume (green triangle) and on the digital volume at the end of the CFD simulation (blue square).

4.5 Conclusions

Commonly capillary pressure measurements provide a *macroscopic* P_c over the whole volume. Nevertheless, capillary pressure can be estimated from the curvature of fluid-fluid interfaces, reconstructed by high-resolution X-CT (Armstrong et al., 2012; Andrew et al., 2014a). This innovative indirect measurement technique is critically reconsidered in the present work. An imbibition process is numerically simulated by solving the full Navier-Stokes equations for two-phase flow at pore-scale in a digital sample of Bentheimer sandstone. Capillary pressure is estimated with two different approaches based on a one-by-one analysis of oil ganglia: as the pressure jump across the oil-water interfaces (using the pressure field data outcome of the numerical simulation) and as the pressure difference resulting from the local, mean curvature of the same interfaces, via the Young-Laplace equation. The two methods yield results in satisfactory agreement with each other and with experimental data, derived by traditional macroscopic measurement techniques, in particular once equilibrium conditions are approached and the validity of Young-Laplace relation is ensured. The direct comparison of curvature-based P_c with curvature-based P_c for a larger sample of the same rock undergone laboratory flooding, gives further evidence of the reliability of the method and demonstrates, once more, the capability of numerical simulations to estimate P_c on small rock fragments.

It is also verified that the numerical calculation of the curvature on triangulated surfaces is rather sensitive to the approximations involved in the numerical procedure, which raises serious accuracy issues: guidelines and warnings are provided to mitigate the inaccuracies arising in this process. Specifically, the results prove to be more accurate when the tessellated surface is generated on a 3D real value map, rather than a binarized volume.

All in all, the reported results suggest that the indirect measurement technique of capillary pressure, proposed by Armstrong et al. (2012) and Andrew et al. (2014a), is reliable, fast and relatively easy to implement, though several questions justify further investigation and the significance of the measured capillary pressure on the small samples tractable by this technique should be addressed.

Chapter 5

Dynamic contact angle

The dynamics of the contact line, where the advancing interface intersects the solid wall surface forming the so called contact angle, is of particular interest for its possible effect on the evolution of the percolation process. While a constant contact angle is commonly assumed at the solid wall, in a dynamic advancement process the contact angle does not remain constant and varies depending on the flow regime (injection rate), the fluids rheology (density and viscosity) and the solid surface properties (roughness and wettability). In transient processes within saturated and unsaturated porous media each of the above mentioned factors may rapidly change and a model accounting for dynamic wetting is required.

Friedman (1999), using a simplified description of a porous medium, justifies the dependance of saturation history and $P_c(S_w)$ relation on fluid flow velocity change, due to a contact angle variation occurring in transient processes in unsaturated porous media. Friedman (1999) states that, for a given P_c, the degree of wetting phase saturation decreases with increasing fluid flow velocity during imbibition and vice versa for drainage.

Hilpert and Ben-Davis (2009) analyze the infiltration of a liquid droplet into a tube-bundle porous medium as a cascade of three phases, IDA (Increasing Drawing Area), CDA (Constant Drawing Area) and DDA (Decreasing Drawing Area). In each phase, the change in contact angle and the motion of contact line are considered, as well as the contact angle hysteresis, which causes a non-unique equilibrium contact angle in rear and front parts of the droplet.

Usually CFD simulations are based on a constant static contact angle model. This limitation is relaxed in the present study, where a *dynamic contact angle* model is used to provide some insight on the role of the contact angle in a dynamic process. To this end the dynamic contact angle model is coupled with the traditional VOF-CSF model (Nichols and Hirt, 1981; Brackbill et al., 1992) to simulate the dynamics of two-phase, immiscible flows. The oil/water flow through a water-wet reservoir rock in a typical drainage displacement is considered as relevant application.

Numerical simulations are carried out for two different flow configurations:

1. A simple test-case (water/air flow within a two-dimensional micro-channel) is used to compare the VOF solutions obtained with static and dynamic contact angle to an approximate model, whose analytical solution has been proposed by (Saha et al., 2009).

2. A digital rock sample reconstructed by high-resolution X-CT, allowing to underline the differences between static and dynamic contact angle models in terms of fluid saturation profiles, ending saturations and macroscopic capillary numbers.

5.1 Dynamic wetting theory

Dynamic wetting denotes the process occurring when one fluid displaces another one from a solid surface. From a microscopic point of view, the most noticeable feature of dynamic wetting is the *contact line* which the advancing fluid forms with the defending fluid, intersecting a solid surface. Dynamic wetting has been widely discussed in literature, particularly for liquid/air systems. The nature of the solid surface and the flow conditions are only two of the main factors governing the local wetting physics. At low displacement rates, on microscopic and sub-microscopic length scales, wetting is likely to be the result of molecular solid/fluid forces. At high displacement rates, the solid/fluid interaction forces compete with hydrodynamic forces in the receding fluid, which forms a thin film on the solid surface, causing the advancing fluid to fail to wet the surface, especially if it is not perfectly smooth (Bascom et al., 1964; Teletzke et al., 1988). That is the reason why the rough surfaces of porous media are more easily wetted when velocities of the wetting advancing front are sufficiently low.

In a state of thermodynamic equilibrium, the equilibrium contact angle θ_E is related to the interfacial tensions between the solid surface and the fluid phases (σ_{s1} and σ_{s2}) and those between the fluids (σ_{12}), through the Young's equation:

$$\sigma_{s1} = \sigma_{s2} - \sigma_{12} \cos\theta_E \tag{5.1}$$

The contact angle in Eq. (5.1) is also referred to as the static contact angle, θ_s. When the contact line moves, the contact angle deviates from the equilibrium value and a *dynamic contact angle* θ_D can be measured at the intersection point. The interaction between hydrodynamic and surface tension forces yields a curvature of the fluid/fluid interface that varies sharply near the contact line.

Although a multitude of experimental data has been published over the years and the proposed models for θ_D describe reasonably well most of the phenomena experimentally observed, all these models include a limited number of variables influencing the wetting behaviour. In general, the dynamic contact angle θ_D is

supposed to depend on a long list of variables:

$$\theta_D = f\left(\theta_s,\, Ca,\, We,\, Bo,\, \frac{\gamma_{def}}{\gamma_{inv}},\, \frac{\rho_{def}}{\rho_{inv}},\, \frac{L_i}{L},\, \ldots\,,\, \phi;\, \psi, \ldots\right) \tag{5.2}$$

where $Ca = (\gamma_{inv} v)/\sigma$ is the capillary number, $We = (\rho\, v^2\, L)/\sigma$ the Weber number, $Bo = (\rho\, g\, L^2)/\sigma$ the Bond number, γ the fluid dynamic viscosity, ρ the fluid density, ϕ the medium porosity, ψ the surface roughness. L_i represents a relevant length scale other than L (characteristic macroscopic length scale of the flow). The theory universally accepted states that θ_D, for a liquid/air system, increases monotonically with the displacement velocity v and that the increment is more rapid the more viscous the advancing liquid is. Most of the empirical models describing the behaviour of θ_D ground on this assumption.

Distinct wetting mechanisms occur in liquid/solid systems with *complete wetting* ($\theta_E = 0$) and *partial wetting* ($\theta_E \geq 0$). The first empirical model, valid for non-volatile liquids which completely wet the solid surface, has been proposed by Hoffman (1975) and states that the dynamic contact angle θ_D uniquely depends on the capillary number Ca:

$$\theta_D = f_{Hoff}\,(Ca) = \cos^{-1}\left\{1 - 2\tanh\left[5.16\left(\frac{Ca}{1 + 1.31\,Ca^{0.99}}\right)^{0.706}\right]\right\} \tag{5.3}$$

Hoffman tested different organic liquids over a wide range of capillary numbers ($4 \times 10^{-5} < Ca < 36$). The model is the result of experimental observations and comparisons between the micro-scale dynamic contact angle and the macro-scale apparent contact angle within the three-phase region and neglects inertial and gravitational effects. At $Ca < 0.1$, Eq. (5.3) can be written as follows:

$$\theta_D = 4.54\, Ca^{0.353} \tag{5.4}$$

which is better known in the form proposed by Voinov (1976) and Tanner (1979):

$$\theta_D^3 = c_T\, Ca \tag{5.5}$$

Even though partially wetted surfaces may be susceptible to contact angle hysteresis between the advancing angle θ_a and the receding angle θ_r, Hoffman adapted his model to partially wetting liquid/air systems, by introducing a shift-factor $f_{Hoff}^{-1}(\theta_s)$ which accounts for a non-zero static contact angle (Figure 5.1):

$$\theta_D = f_{Hoff}\left[Ca \,+\, f_{Hoff}^{-1}\,(\theta_s)\right] \tag{5.6}$$

Hoffman's model for partially wetting systems implies that θ_D is strictly bound to its corresponding static contact angle at low Ca, whereas diverges from θ_s whenever Ca values are comparable to the term $f_{Hoff}^{-1}\,(\theta_s) = Ca^*$. Thus, given a Ca, θ_D loses

its dependence on θ_s at small θ_s values, as shown in Figure 5.2. Other empirical models describe the behaviour of the θ_D in terms of capillary number, Weber number, Bond number and viscosity ratio (Gutoff and Kendrick, 1982; Bracke et al., 1989). An exhaustive review of dynamic contact angle models has been provided by Kistler (1993).

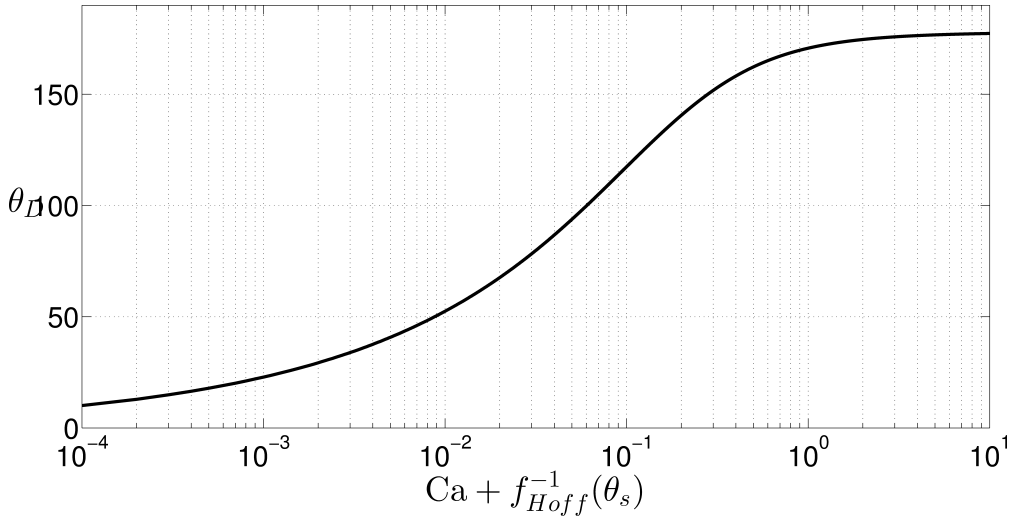

Figure 5.1: Apparent dynamic contact angle θ_D for partially wetting systems, according to Hoffman's model.

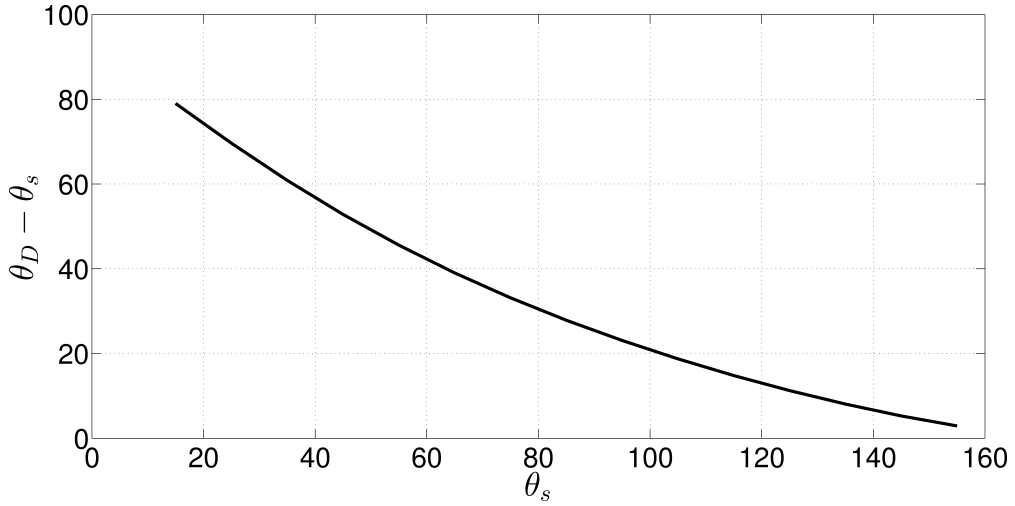

Figure 5.2: Difference between θ_D and θ_s as a function of θ_s ($Ca = 0.05$).

5.1.1 Dynamic contact angle model

The angle measured within the wetting phase and delimited by the fluid-fluid interface and the fluid-solid wall interface is conventionally defined as the *dynamic contact angle* in moving contact line problems.

The dynamic contact angle is affected by hysteretical behaviour, i.e., it is larger than the static contact angle under advancing front conditions, whereas it is smaller under receding conditions ($\theta_a \geq \theta_s \geq \theta_r$). However, in typical wetting problems (e.g. water displacing air) occurring at low displacement rates, the dynamic contact angle is supposed to remain near its static value ($\theta_D \simeq \theta_s$).

In the VOF method a fixed contact angle is usually used for moving contact line problems. Here the dynamic contact angle θ_D is assumed to vary according to the Hoffman's empirical correlation. The capillary number Ca in Eq. (5.6) is based on the fluid velocity v_{CL} at the contact line:

$$Ca = \frac{\gamma v_{CL}}{\sigma} \tag{5.7}$$

where γ is the advancing fluid viscosity and σ is the fluid-fluid interfacial tension. The contact line velocity v_{CL} is:

$$v_{CL} = \boldsymbol{v} \cdot \hat{n} \tag{5.8}$$

where $\boldsymbol{v}$ is the local fluid velocity and $\hat{n}$ is the unit normal to the interface.

An User Defined Function (UDF), originally proposed by Miller (2009) to describe the dynamics of a water droplet in a flow channel of a fuel cell, has been modified to account for the contact angle variability during two-phase displacements. The dynamic contact angle is prescribed to vary with the wall contact line velocity, according to the equations reported above. The UDF has been implemented in the ANSYS FLUENT®-VOF model.

The UDF computes the phase gradients in the cells close to the wall which contain the interface and calculates the corresponding interface normal, then it estimates the dynamic contact angle (either advancing or receding) at the current time step via Hoffman's function. A positive or negative sign of the contact line velocity indicates an advancing or receding contact angle, i.e., depending on the motion direction. The correction for partial wetting requires to know the shift-factor $f^{-1}_{Hoff}(\theta_s) = Ca^*$, which is evaluated using the bisection method in a zero finding function routine. The local capillary number Ca^* is the root of the function $f(Ca^*) = \theta_s - f_{Hoff}(Ca^*)$.

The UDF code written in C language and implemented in the solver, to simulate an oil/water displacement, is given in Appendix A.

5.2 Results

5.2.1 Test on a micro-channel

The advancement of a meniscus between two narrowly spaced plates is a commonly used configuration. This arrangement referred to as *capillary displacement* or *capillary filling*, is ideally suited to probe the mechanisms governing dynamic wetting, since gravitational and inertial effects are neglected.

A simple test-case here proposed mimics a spontaneous capillary filling within a two-dimensional micro-channel, initially occupied by air ($\rho_a = 1.205\,\mathrm{kg/m^3}$, $\gamma_a = 1.81 \times 10^{-5}\,\mathrm{kg/(m \cdot s)}$), is progressively filled with water ($\rho_w = 998.2\,\mathrm{kg/m^3}$, $\gamma_w = 0.001\,\mathrm{kg/(m \cdot s)}$). Two different flow configurations are simulated, where the equilibrium contact angle is either 30° or 60°. Results obtained by both the static and dynamic contact angle models are compared. The simple geometry adopted in the test-case consists of two plates closed to each other in order to facilitate the capillary filling. The plates width is equal to the cell side length, hence the process is tackled as a two-dimensional problem. For the test-case the channel height is $H = 2.0 \times 10^{-5}$ m, the channel length is $L_c = 3.3 \times 10^{-3}$ m. In its initial configuration the water-air flat interface is at $L_0 = 2 \times 10^{-4}$ m. For the numerical VOF simulation a regular mesh with a cell side 7.41×10^{-7} m is adopted.

The two-dimensional displacement is approached by both a VOF numerical model and an approximate analytical model. The horizontal position of the meniscus versus time is taken as the model validating-variable.

Under spontaneous capillary-filling conditions, the momentum conservation in the two-dimensional channel can be expressed in terms of a balance between the time rate of change of momentum, surface tension force and viscous force (Saha et al., 2009):

$$\frac{\mathrm{d}(\rho H\, L\, v_{\mathrm{Avg}})}{\mathrm{dt}} = 2\sigma \cos(\theta_s) - \frac{12\,\gamma\, L\, v_{\mathrm{Avg}}}{H} \tag{5.9}$$

where v_{Avg} is the average meniscus travelling velocity, H is the channel width, L is the distance travelled by the liquid meniscus, ρ is the fluid density, σ is the interfacial tension. The pressure overhead, in addition to the pure capillary pressure already accounted for by the surface tension related forces, is neglected as we deal with a *spontaneous* capillary filling. The effect of the contact line velocity on the dynamic contact angle is not kept in consideration by the analytical model, that assumes a constant contact angle value θ_s.

In the case of zero initial velocity, the analytical transient solution of Eq. (5.9) is reported in (Saha et al., 2009). Briefly:

$$L = \sqrt{\left[\frac{A}{B^2} e^{-B\,\mathrm{t}} + \frac{A\,\mathrm{t}}{B} + \left(L_0^2 - \frac{A}{B^2}\right)\right]} \tag{5.10a}$$

$$v_{\text{Avg}} = \frac{A\left(1 - e^{-B\,\text{t}}\right)}{2BL} \tag{5.10b}$$

where:

$$A = \frac{4\sigma\cos(\theta_s)}{\rho\, H}; \qquad B = \frac{12\gamma}{\rho\, H^2} \tag{5.11}$$

Here an additional transient solution, which incorporates the dynamic contact angle $\theta_D(v_{CL})$ is also implemented.

Figure 5.3 is a snapshot of the water/air interface while travelling through the channel. The displacing red phase is water ($\alpha = 1$) and the displaced blue phase is air ($\alpha = 0$). The numerical model is initialized by assigning two distinct phase regions, separated by a flat interface, to water and air. In the figure, the interface configuration is already modelled by the interfacial forces with curvature $\kappa = \nabla \cdot \hat{n}$. The interface is tracked with a piecewise-linear geometric reconstruction scheme and the smearing is limited to few cells.

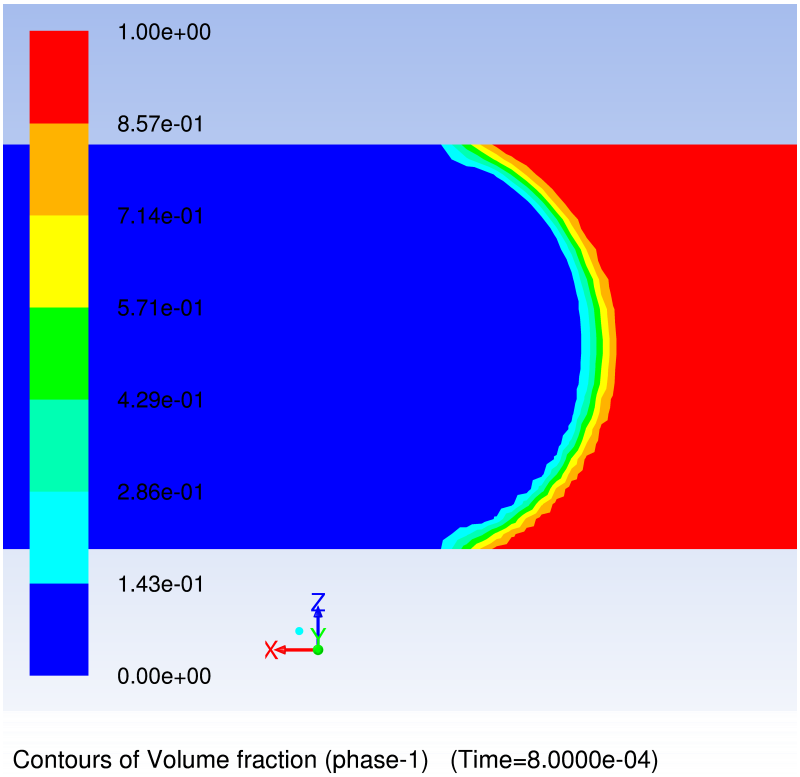

Figure 5.3: Snapshot of the interface between water (red) and air (blue) at time 8×10^{-4} s.

Figure 5.4(a) shows the distance travelled by the interface, as a function of time, predicted with the analytical models (continuous lines) and with the VOF numerical model (dashed lines). The value of the initial contact angle is 30°. The red (blue) lines refer to a 30° static (variable dynamic) contact angle model. Computed travelled distance, time and velocity are reported as dimensionless variables $\widehat{L}$, $\widehat{t}$ and $\widehat{v}$, respectively:

$$\widehat{L} \equiv \frac{L}{H}; \qquad \widehat{t} \equiv \frac{t\,\nu}{H^2}; \qquad \widehat{v} \equiv \frac{v_{\text{Avg}}\,H}{\nu} \tag{5.12}$$

where ν represents the kinematic viscosity of water.

The temporal profiles obtained with the VOF numerical model are in good agreement with those provided by the analytical models, which yield a faster movement of the interface as they neglect both inertial phenomena and viscous forces in the air phase. The distance travelled predicted with dynamic models confirms that the contact angle θ_D increases and, consequently, the $2\sigma\cos(\theta_D)$ force term lowers its contribute to the mobility of the advancing wetting phase. As a result, the velocity v_{Avg} predicted by the models considering the contact angle variability is lower than those predicted with static models, as corroborated by the profiles of Figure 5.4(b), reporting the interface advancing velocity versus time. The peak appearing in the velocity profiles is motivated by the progressive increment of the viscous resistance, initially equal to zero, which tends to counterbalance the positive capillary force.

Figures 5.5(a) and 5.5(b) refer to an initial static contact angle $\theta_s = 60°$ and strengthen the considerations derived for the case with $\theta_s = 30°$. The direct comparison of the two cases reveals a lower interface velocity for the low-wettability configuration ($\theta_s = 60°$), due to the correspondingly reduced intensity of the capillary force, proportional to $\cos(\theta_s)$.

In Figure 5.6(a) the time evolution of dynamic contact angle, as computed with the analytical models for initial static contact angle values 30° and 60°, is shown. We can easily deduce that the dynamic angles remain slightly above the corresponding static angles and with a larger difference when $\theta_s = 30°$, thus in perfect agreement with the Hoffman's postulate, stating that θ_D remains closer to θ_s for small static angles and tends to lose rapidly its sensitivity to θ_s for large static angles (see Figure 5.2).

Figure 5.6(b) shows the profile of the capillary number Ca computed with the analytical model. The aforementioned minor difference between the static and the limiting value of the dynamic contact angle when $\theta_s = 60°$ can be ascribed to the relatively lower values of the capillary number attained in this case ($Ca_{60} \approx 5.4 \times 10^{-3}$, $Ca_{30} \approx 8 \times 10^{-3}$). As evident in Figure 5.6(b), an initial static angle of 30° (high wettability) prompts a faster imbibition and, in turn, higher capillary numbers than those occurring with an initial static angle of 60° (low wettability).

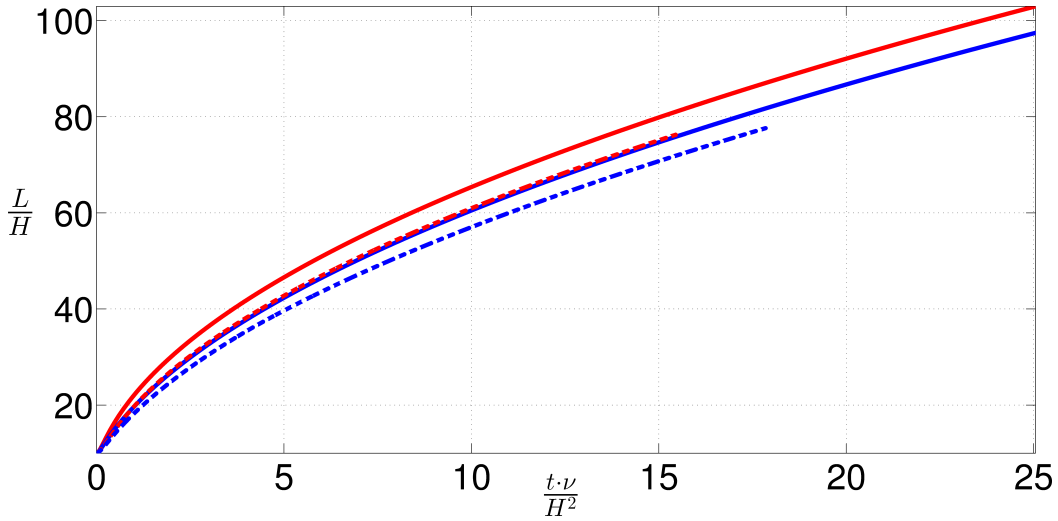

(a)

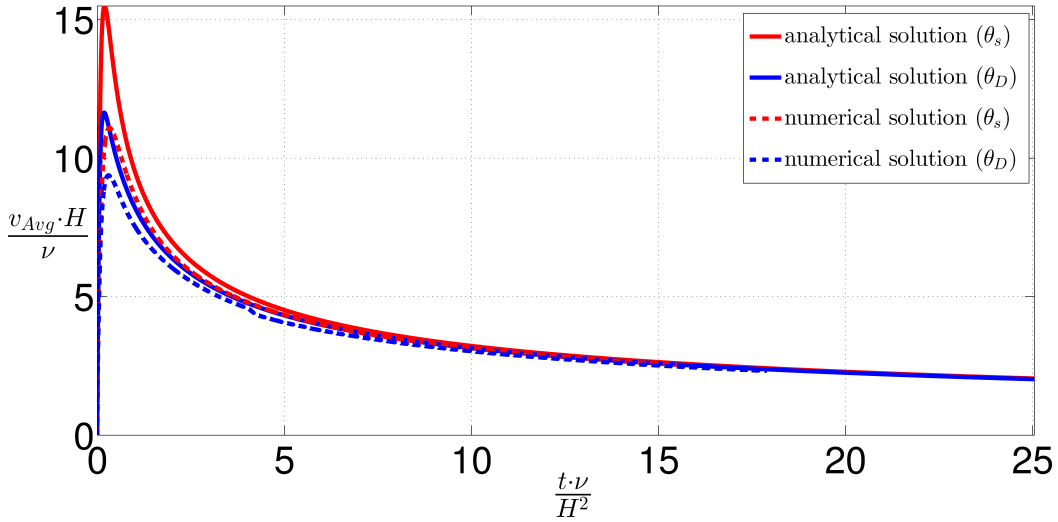

(b)

Figure 5.4: Initial contact angle is 30°. (a) Distance travelled by the interface, as a function of time. (b) Interface advancing velocity, as a function of time. Results obtained with the analytical and the VOF models are represented as solid and dashed lines, respectively. Results referred to a static and dynamic contact angle are represented in red and blue, respectively.

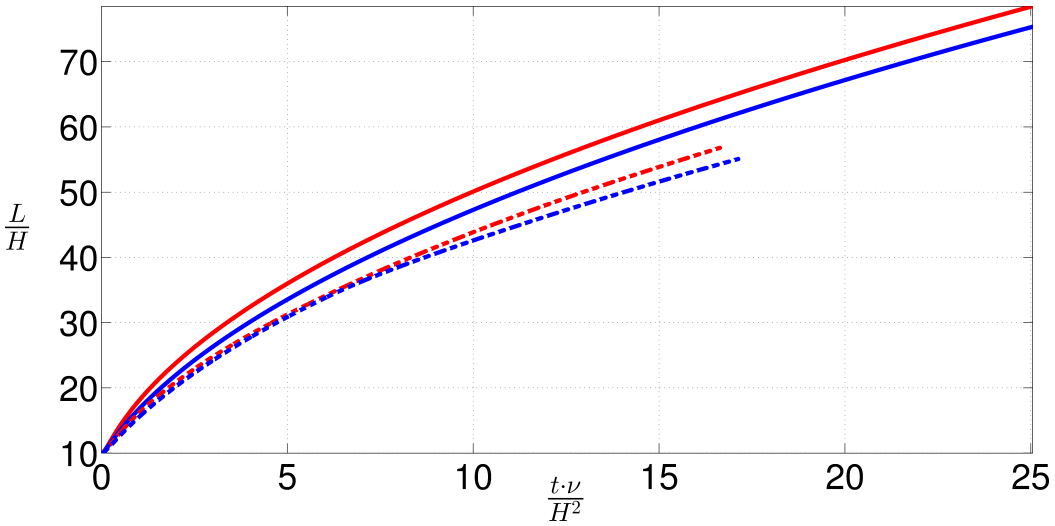

(a)

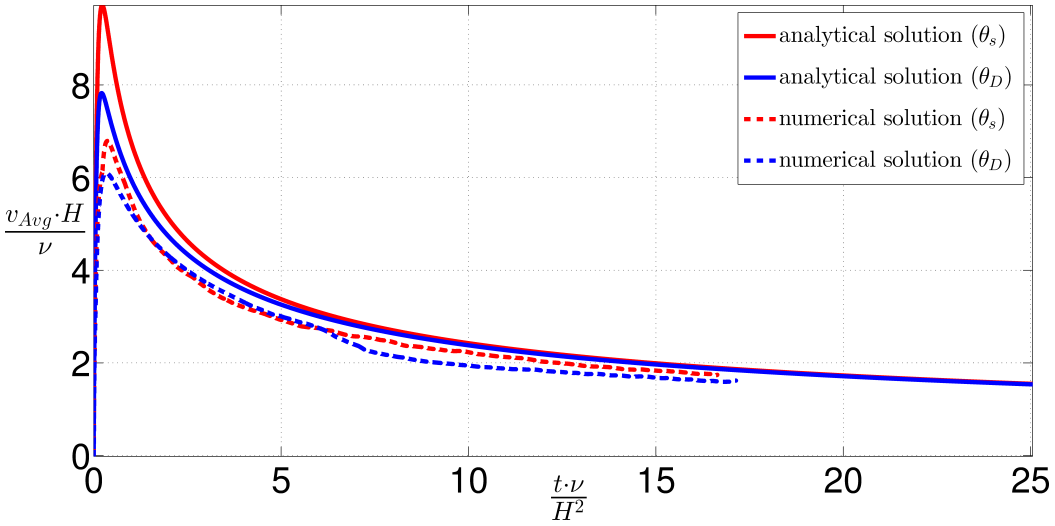

(b)

Figure 5.5: Initial contact angle is 60°. (a) Distance travelled by the interface, as a function of time. (b) Interface advancing velocity, as a function of time. Results obtained with the analytical and the VOF models are represented as solid and dashed lines, respectively. Results referred to a static and dynamic contact angle are represented in red and blue, respectively.

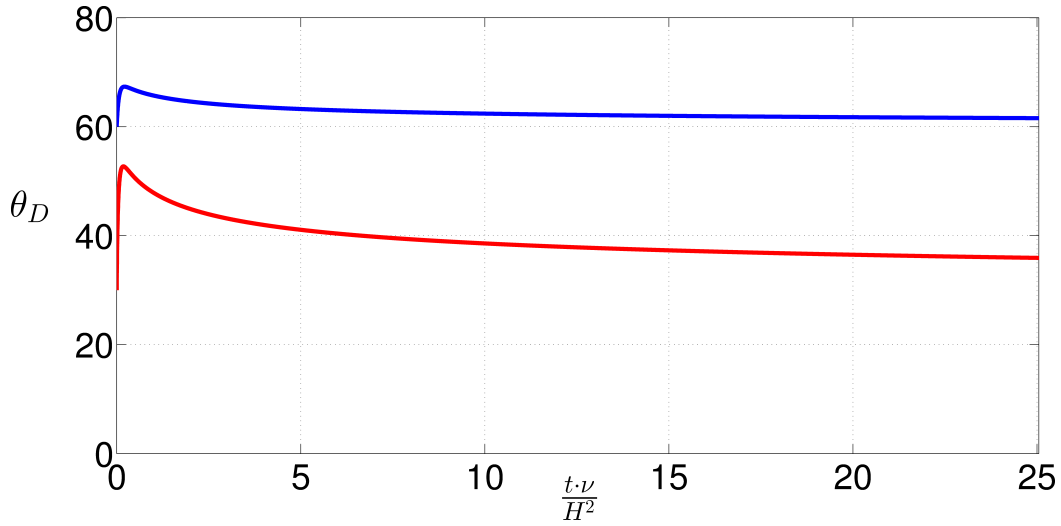

(a)

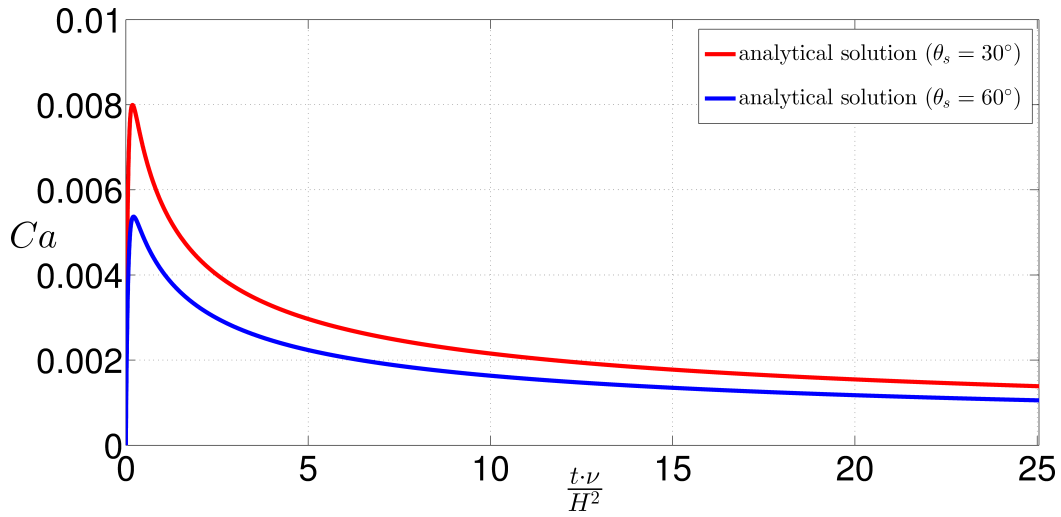

(b)

Figure 5.6: (a) Time dependence of the dynamic contact angle θ_D. (b) Time dependence of the capillary number Ca. Results are obtained with the analytical model. Red lines refer to $\theta_s = 30°$, blue lines to $\theta_s = 60°$.

5.2.2 Porous media application

The dynamic contact angle model is also applied to a drainage of water in an oil/water displacement through a rock sample. Indeed the contact angle variability affects the wettability characteristics of the solid surface and might influence the displacement evolution as well as the sample filling (i.e. saturation profiles), which represents an extremely important information for macro-scale reservoir simulations. As we demonstrated in Chapter 3, phenomena where one invading fluid is injected into the pore space to displace the defending one are used to estimate, via up-scaling, the variables of interest, such as relative permeability and capillary pressure. The dynamics of the displacement is determined by the pore space morphology, the rock wettability to each of the fluids, the fluid rheology, the flow regime and the evolution of the fluid-fluid interface resulting from macro-scale processes and micro-scale effects occurring at the solid surface. The interface is described by its curvature and the dynamic contact angle it forms with the rock solid walls.

The considered case studies mimic traditional laboratory *unsteady-state* drainage experiments. Oil (non-wetting phase) is injected in a water-saturated sample. The injection is forced by imposing a velocity ramp at the inlet section up to a maximum value v_{in}^{max}. Initially only water is produced. Breakthrough identifes the first appearance of the oil phase in the produced fluids.

Three different scenarios are examined in order to evaluate the sensitivity of macroscopic parameters, such as saturation and capillary number, to a change in flow conditions and fluid rheology. Oil properties are defined based on experimental measurents of light, medium and heavy crude oils (Al-Besharah et al., 1987). The numerical simulations are carried out using both a constant contact angle and a dynamic contact angle model. In all the tests the initial static angle, measured within the water wetting phase, is $\theta_s = 30°$. Fluid properties and flow conditions of the three models are reported in Table 5.1.

Table 5.1: Fluid rheology and flow conditions used in the numerical models.

CASE	ρ_w [kg/m^3]	γ_w [kg/(m · s)]	ρ_o [kg/m^3]	γ_o [kg/(m · s)]	v_{in}^{max} [m/s]
Case 1	998.2	0.001	800	0.003	0.03
Case 2	998.2	0.001	953	0.049	0.03
Case 3	998.2	0.001	800	0.003	0.1

The temporal profiles of oil saturation and capillary number are shown in Figures 5.7, 5.8 and 5.9. The overall capillary number Ca is evaluated according to its macroscopic definition, $Ca = \gamma_{inv}\, v_{inv}/(\sigma)$, where v_{inv} is the intrinsic volume-averaged velocity of the oil (invading) phase.

The time evolution of the oil saturation between static and dynamic contact angle models is remarkably different for the first case, as visible in Figure 5.7(a). In the dynamic model, the interface convex with respect to the oil phase adapts to the pore/grain interface and the slope of the contact line is dictated by the Hoffman's model. The contact angle is supposed to deviate from its static value. The augmented convexity of the oil/water interface allows the generally receding water phase to remain more adhesive to the solid wall. This increased water wettability results in a predicted oil saturation lower than that predicted via standard VOF with constant contact angle, particularly in the initial stage of the drainage process, when the inertial effects are rather low. The discrepancy is also detectable in the capillary pressure profiles of Figure 5.7(b). As the oil velocity and the overall macroscopic capillary number Ca become higher, the saturation profiles get close to each other and tend towards a common saturation value. At an advanced stage of the process, local phenomena such as bubble formation and break-off of the continuity of the oil phase are predominant. The oil phase is supposed not to be the only one to advance, i.e. oil bubbles detached from the main front may be replaced by the continuous water phase.

In spite of what expected from the Hoffman's theory, the increased oil viscosity in case 2 and the greater acceleration (0,67 m/s^2 vs. 0.20 m/s^2), which the injected oil phase undergoes in case 3, have no detectable effect on the process evolution. Figures 5.8 and 5.9 show an excellent agreement between static and dynamic contact angle models: both oil saturation and capillary number versus time profiles exhibit a nearly perfect overlapping and the models seems to predict similarly the overall displacement. The affinity of static/dynamic models in case 2 and case 3 is confirmed by the breakthrough times t_B, reported in Table 5.2.

Table 5.2: Breakthrough time t_B for the three (static/dynamic) models.

	Case 1 t_B, [s]	**Case 2** t_B, [s]	**Case 3** t_B, [s]
STATIC	0.0292	0.0705	0.0325
DYNAMIC	0.0586	0.0711	0.0320

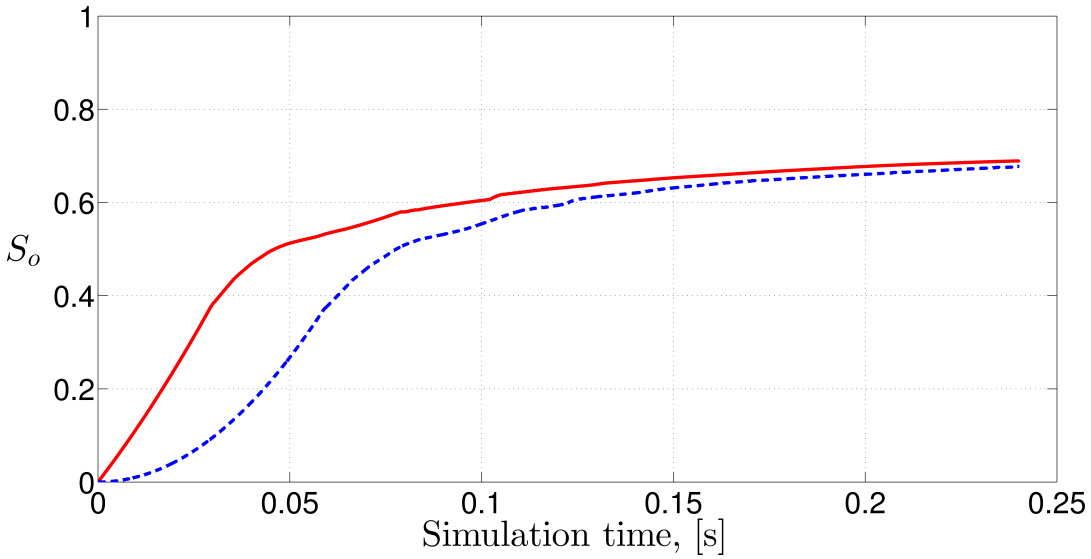

(a)

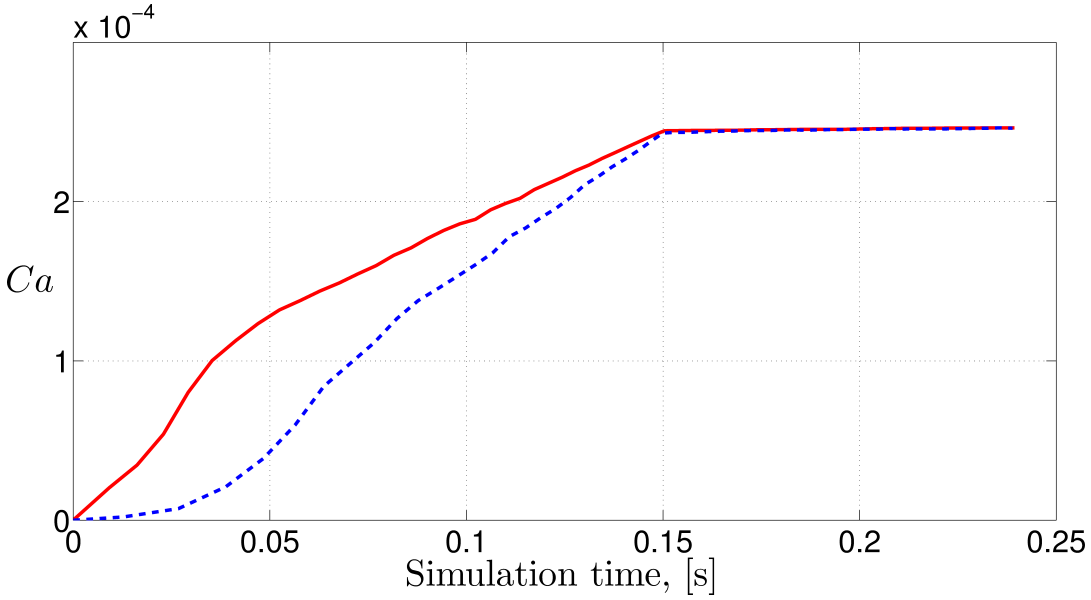

(b)

Figure 5.7: **Case 1**. (a) Oil saturation, as a function of time. (b) Macroscopic capillary number, as a function of time. Results relative to the static (dynamic) contact angle model are represented in solid red (dashed blue) line.

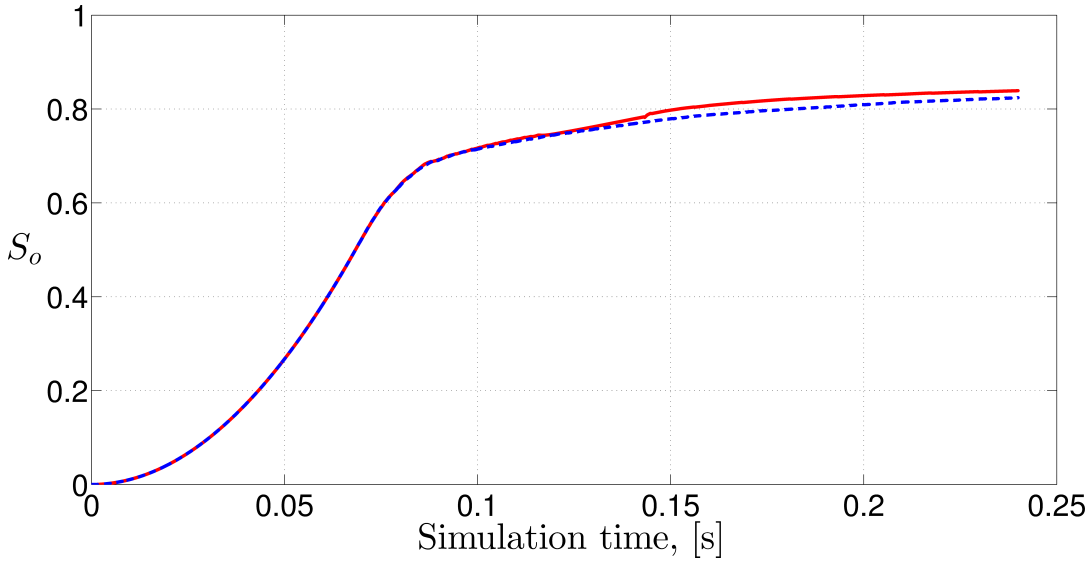

(a)

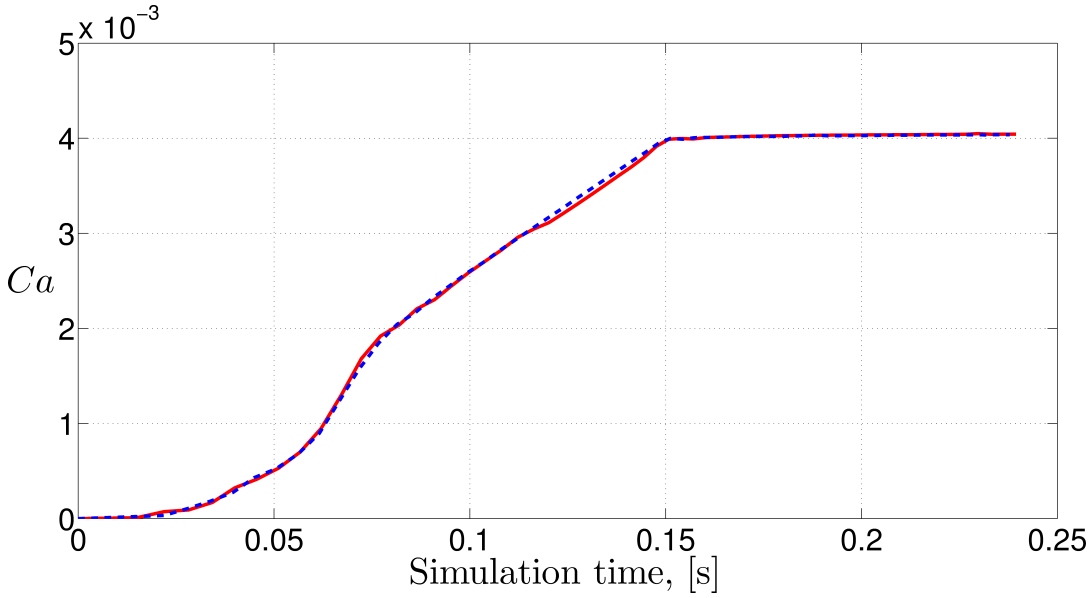

(b)

Figure 5.8: **Case 2**. (a) Oil saturation, as a function of time. (b) Macroscopic capillary number, as a function of time. Results relative to the static (dynamic) contact angle model are represented in solid red (dashed blue) line.

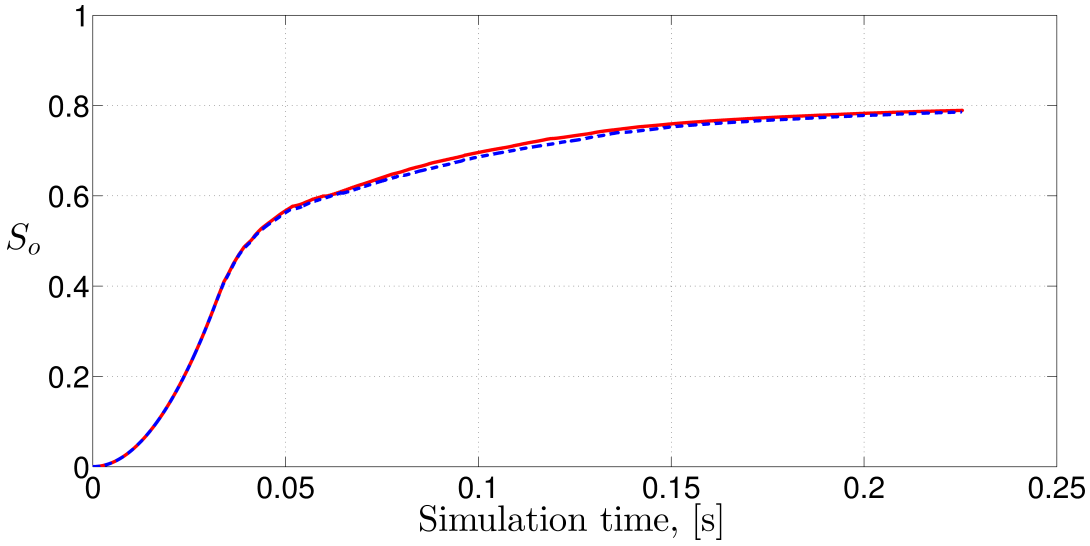

(a)

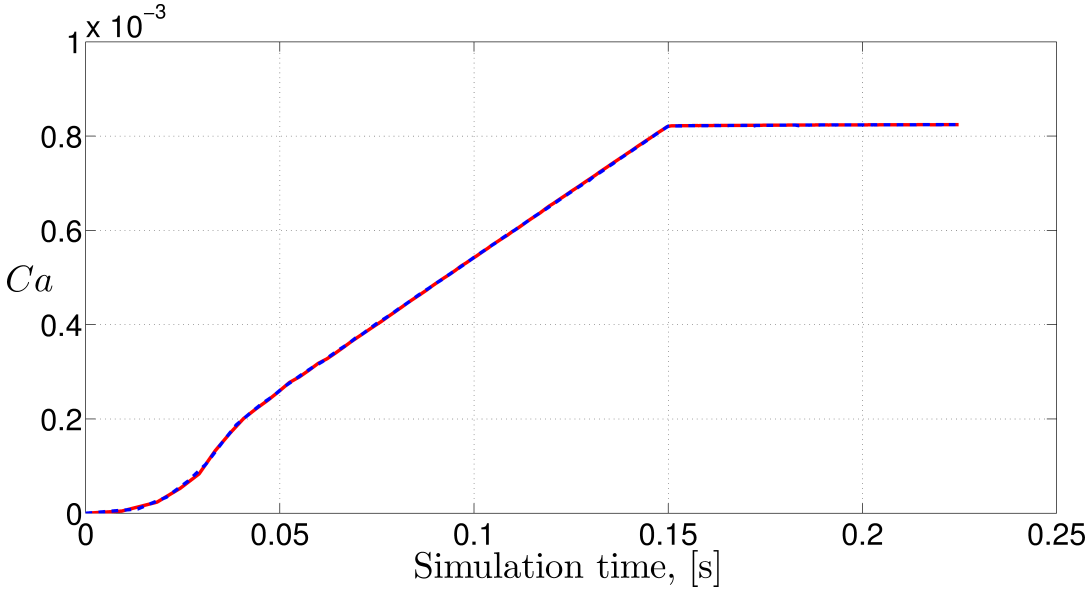

(b)

Figure 5.9: **Case 3**. (a) Oil saturation, as a function of time. (b) Macroscopic capillary number, as a function of time. Results relative to the static (dynamic) contact angle model are represented in solid red (dashed blue) line.

The gaps recorded in the ending oil saturation between the static and the corresponding dynamic contact angle model, in the three cases, are: 1.21% (case 1); 1.50% (case 2); 0.37% (case 3).

It is worth pointing out that very little is known about the physics governing the contact line motion in oil/water displacements, since most of the experimental studies concern water/air and oil/air systems. Keller et al. (2007) studied the effect of advancing velocity and fluid viscosity on the contact angle variability for several oils in an oil/air system, by using a Wilhelmy plate technique. The authors stated that a general increment of the contact angle occurs with a high-viscosity oil, even though "*the contact angle becomes insensitive to the advancing velocity above 150-200 $\mu m/s$*". It must be stressed that the viscosities tested by the authors are much higher than those here adopted, while the injection velocities are considerably lower than those imposed at the inlet section of our models.

5.3 Conclusions

To summarize, a dynamic contact angle model is implemented via User Defined Function (UDF) in a commercial solver to account for the dynamics of the interface at the contact line. A numerical VOF-based model is employed to simulate a spontaneous water capillary filling in a two-dimensional channel and numerical results are tested against exact analytical solutions. Both numerical and analytical models are improved including the dynamic contact angle, that is assumed to depend on the wall contact line velocity. Some preliminary interpretations of the role of the dynamic contact angle on capillary phenomena are derived. Specifically, the results evidenced with the test-case are the following:

- Underestimated advancement of the water front provided by the numerical models, as they consider the viscous resistance in the air phase which is neglected in the analytical models.
- Underestimated advancement of the water front produced by the dynamic contact angle models, in both analytical and numerical solutions. During the displacement, the increment of the contact angle induces a reduction in the surface force contribution to the front motion and, as a consequence, the overall process is slowed down. The effect is more evident with a larger initial static angle ($\theta_s = 60°$).
- Proven validity of the Hoffman's theory, declaring that a smaller difference between the dynamic and the static contact angle ($\theta_D - \theta_s$) is observed with a small initial static angle, whereas θ_D tends asymptotically towards its corresponding θ_s at decreasing capillary numbers.

- The temporal profiles of the capillary number, as well as the advancing front velocity, present a peak by virtue of the progressive increment of the viscous forces to counterbalance the capillary forces.

Moreover, the model accounting for the contact angle variability is applied to an oil/water displacement through a sample of reservoir rock, reconstructed with high-resolution computed tomography. The drainage is mimicked by injecting oil within the initially water-saturated sample. Certainly, basic considerations inferred with regard to fluid front advancement and contact angle variability for the test-case are not easily deducible for a rock sample and its tangled porous system, for which only a macroscopic analysis can be deduced, as a whole.

Both static and dynamic contact angle models are considered and results in terms of fluid saturation and capillary number are compared. A "sensitivity" analysis is conducted by changing the properties of the oil phase (from light to medium crude oil) and the flow conditions (oil injection rate). The results reveal no significant macroscopic effects of the interface configuration on the final sample saturation. However a remarkable disagreement between static and dynamic models is observed in the first part of the time-saturation profiles, if the fluid injected has a low viscosity and the injection rate is sufficiently low. On the contrary, the process is equally predicted with both the models, i.e., the saturation evolution seems to be insensitive to change in contact angle, when the drainage displacement is carried out at high rates or else the viscosity of the injected fluid is high.

During the spontaneous processes occurring in reservoir rocks, the advancing front velocity is very low (of the order of 10^{-5} m/s), hence a dynamic contact angle model may be considered as more adequate approach to investigate the dynamics of the fluid-fluid interface. However the Hoffman's theory, well-describing the dynamic wetting for liquid/air systems, seems not to be trustworthy for oil/water systems and in general when the viscous resistance of the displaced fluid is not negligible. In this case, a model which considers the fluid viscosity ratio ($\gamma_{def}/\gamma_{inv}$), as the one proposed by Gutoff and Kendrick (1982), should be adopted.

Chapter 6

Conclusions and recommendations for future works

This thesis presents a number of novel, non-invasive *measurement techniques* for characterization of porous media (e.g. reservoir rocks) and estimation of the related hydraulic properties:

1) X-ray radiography and micro-tomography (X-CT).

2) Numerical simulations at micro-scale of single-phase and multi-phase flows.

These innovative techniques support the complementary traditional ones consisting of invasive and time-consuming laboratory tests, performed on real porous samples. The present research aims to investigate reservoir rock samples and exploits the aforementioned methods to mainly estimate two parameters, i.e. relative permeability k_r and capillary pressure P_c, which are key factors in macro-scale reservoir simulations. These petro-physical properties are commonly estimated as macroscopic mean values and correlated to the wetting phase saturation. Measurements are acquired by connecting the terminal sections of the sample to the measurement system and may lack of accuracy when the non-wetting phase breaks off from the main front into isolated fluid parcels, which are destined to be trapped in the pore bodies. X-CT and numerical simulations rely on a different (microscopic) approach and allow for k_r and P_c estimation, from the underlying internal pore space structure.

Firstly, X-ray radiography turned out to be a fast tool, since it offers the possibility to derive the two-dimensional porosity and the brine saturation maps from simple planar images of the porous sample undergoing brine filling. The subsequent drainage with oil allowed to derive the oil maps by solving the system of linear equations in the variables 'brine length' and 'oil length', through the so-called material decomposition. The time sequence of saturation profiles was used to obtain the

fluid flow properties via history-match technique. X-ray micro-tomography principles were exploited to retrieve the third spatial dimension, by the employment of the FBP algorithm to reconstruct the internal structure of the rock sample and provide a digital volume amenable for morphological measurements and fluid-dynamic simulations. Image analysis techniques (segmentation, binarization, DT-watershed) permitted to visualize the pore space and extract the quantitative data of interest (volumetric porosity, pore volume, pore equivalent diameter). Such meaningful informations are extremely useful for determining the adequacy of the tomographic resolution to accurately describe the pore space morphology.

Secondly, the mesh extracted from the 3D pore space structure was used for the direct numerical simulation of single-phase and two-phase flows at micro-scale, by the employment of a well-established commercial solver (ANSYS FLUENT®). The absolute permeability was computed and compared to experimental results obtained for the same rock sample. Relative permeability and capillary pressure curves were derived following the *steady-state* protocol, in both drainage and imbibition processes, and put in relation to those gathered by means of dedicated laboratory tests. Results are encouraging and reveal a good agreement, especially in terms of capillary pressure and water (wetting phase) relative permeability. On the contrary, when compared to the experimental results, the oil relative permeability data exhibit a remarkable discrepancy, which could be ascribed to the limited digital sample size or, alternatively, to the tendency of the oil non-wetting phase to form isolated blobs not interacting with the measurement system in the experimental tests, thus a possible cause of misleading results. The numerical procedure looks promising in capturing the hysteretical behaviour of k_r and P_c, as well.

Thirdly, a microscopic approach was adopted to estimate local and averaged capillary pressure, by extracting the interface curvature from a set of oil ganglia during water imbibition and by applying the well-known Young-Laplace relationship. The procedure operates on a ganglion-by-ganglion basis and approximates the ganglion surface with a quadratic form. Many preliminary tests revealed a series of accuracy issues related to surface approximation and smoothing procedures, which were mitigated by means of ad hoc strategies. It was verified that a mesh extracted from a real value distance map is locally smoother than a binarized map, thus more suitable for curvature calculations. Curvature-based capillary pressures were compared to those calculated by averaging the pressure field outputs of a numerical simulation performed on a small digital sample. A closer agreement between the two sets of data (i.e. the validity of Young-Laplace) was obtained, once ganglia stability was reached and kinetic energy of the system was considerably decreased. The ganglion-by-ganglion analysis for curvature estimation was also applied to a bigger 3D tomographic volume, reconstructed, as a three-level field, after an imbibition experiment. The capillary pressure distribution of "simulated" ganglia showed a larger spread compared to the "experimental" ganglia distribution, due to the insufficient number

of instances provided by the smaller digital sample. Surface-area-weighted average capillary pressures turned out to be in extremely good agreement with capillary pressure measurements obtained via layered porous plate experiments on a rock sample of the same formation and with similar physical (porosity) and hydraulic (absolute permeability) properties.

Finally, we presented a model accounting for a variable contact angle at the solid wall in an immiscible fluid/fluid displacement. The model is based on the universally accepted Hoffman's theory, postulating a sole dependence of the contact angle on the capillary number. It well describes the behaviour of partially wetting systems, which constitute almost the entirety of reservoir rocks. The model, optimized to predict the contact angle changeability in advancing and receding conditions, was implemented in a FV-VOF solver and tested in a water capillary filling performed within a two-dimensional micro-channel. The analytical solution in terms of time-dependent water front position (water column length) and average front velocity for a static contact angle is known. An improved transient analytical solution incorporating the dynamic contact angle was also introduced. Two different initial contact angle configurations (30° and 60°) were considered. In both configurations, the numerical solutions provided lower values of water column length and front velocity than the analytical solutions, a fact that could be explained with the air viscous resistance considered with the numerical model and disregarded in the analytical model. A faster advancement was observed for the smaller angle (30°), due to the higher wettability of the water phase. The time evolution of the contact angle demonstrated the tendency of the larger angle to remain much closer to its static value than the smaller one, as expected from the Hoffman's theory. Both configurations tend to the equilibrium angle at decreasing capillary numbers. Furthermore, the dynamic contact angle model was applied to a porous medium undergoing drainage and compared to a standard constant contact angle model. The sensitivity of saturation history and capillary number on dynamics of contact angle was analyzed by changing fluid rheology and flow conditions. It was observed a noticeable agreement between the two models, as long as the viscosity of the injected fluid is high or the fluid is forced to enter the sample at high rates. Differently, the saturation profiles sensibly diverge at a first stage of the drainage process, in the less "viscous" case. However, at an advanced stage of the process, the ending saturations reached with both static and dynamic contact angle approach a common value.

The presented research claims to provide interesting tools for visualization and quantitative characterization of displacement phenomena in porous media. Certainly, the complexity of these processes in such heterogeneous domains deserves further, detailed study. Comprehension and accurate description of physics at a molecular level remain a challenge.

We outline the following suggestions for future works:

1. Optimization and thorough validation of dynamic contact angle models able to faithfully represent different liquid/liquid systems, by their implementation in 3D pore-scale numerical simulations, with particular regard to the effect of contact angle variability on hysteretical behaviour of both k_r and P_c.

2. Improvement of the contact line movement by application of a suitable slip-condition.

3. Improvement of the hystory-matching procedure for a better exploitation of the data obtained from X-ray radiographic imaging. The inversion procedure presented in Chapter 2 and reported in our published paper was rather naïve and not optimized to deal with such data.

Appendices

Appendix A

User Defined Function

```
/* UDF for Dynamic Contact Angle */
/* oil displacing water*/

#include "udf.h"
#include "sg_mphase.h"
#include "sg_vof.h"
#include "sg.h"
#include "mem.h"
#define WAT_VISCOSITY 0.001
#define OIL_VISCOSITY 0.003
#define SURF_TENS 0.05
#define inv_Hoff_30 0.0021
#define inv_Hoff_150 0.2802
#define Hoff(x) acos(1-(2.0*tanh(5.16*(pow((x/(1+(1.31*pow(x, 0.99)))), 0.706)))))
#define index_source 3

/* This Code computes the normals of the VOF function*/
DEFINE_ADJUST(store_gradient, domain)
{
        Thread *t;
        Thread **pt;
        cell_t c;
        int phase_domain_index = 1; /* Secondary Domain */
        Domain *pDomain = DOMAIN_SUB_DOMAIN(domain,phase_domain_index);
        void calc_source();
        Alloc_Storage_Vars(pDomain,SV_VOF_RG,SV_VOF_G,SV_NULL);
        Scalar_Reconstruction(pDomain, SV_VOF,-1,SV_VOF_RG,NULL);
        Scalar_Derivatives(pDomain,SV_VOF,-1,SV_VOF_G,SV_VOF_RG,
                Vof_Deriv_Accumulate);
        mp_thread_loop_c (t,domain,pt)
                if (FLUID_THREAD_P(t))
                {
                        Thread *ppt = pt[phase_domain_index];
                        begin_c_loop (c,t)
                        {
```

```
                                calc_source(c,t);
                        }
                        end_c_loop (c,t)
                }
                Free_Storage_Vars(pDomain,SV_VOF_RG,SV_VOF_G,SV_NULL);

/* Message("content of variable a is \n"); */
}


void calc_source(cell_t cell, Thread *thread)
{
        real VOF_Val[3], VOF_Mag, source, VOF_Norm[3];
        Thread *phaset;
        phaset= THREAD_SUB_THREAD(thread,1);
        if(C_VOF(cell,phaset)!=0.0 && N_TIME > 1)
        {
                /* The gradients of the VOF function are found in the x,y and z dir. */
                if (NULLP(THREAD_STORAGE(phaset, SV_VOF_G)))
                {
                Message0("N_TIME = %d, ....show-grad:Gradient of VOF is not available \n ", N_TIME);
                Error("0");
                }
                VOF_Val[0]=C_VOF_G(cell,phaset)[0];
                VOF_Val[1]=C_VOF_G(cell,phaset)[1];
                VOF_Val[2]=C_VOF_G(cell,phaset)[2];
                /* The magnitude of the VOF gradients is found so it can be normalized */
                VOF_Mag=NV_MAG(VOF_Val);
                if(VOF_Mag!=0.0)
                {
                        VOF_Mag=NV_MAG(VOF_Val);
                        VOF_Norm[0]=VOF_Val[0]/VOF_Mag;
                        VOF_Norm[1]=VOF_Val[1]/VOF_Mag;
                        VOF_Norm[2]=VOF_Val[2]/VOF_Mag;
                }
                else
                {
                        /* This is to avoid the divide by zero function*/
                        VOF_Norm[0]=0.0;
                        VOF_Norm[1]=0.0;
                        VOF_Norm[2]=0.0;
                }
                C_UDMI(cell,thread,0)=VOF_Norm[0];
                C_UDMI(cell,thread,1)=VOF_Norm[1];
                C_UDMI(cell,thread,2)=VOF_Norm[2];
        }

}
/* This Define_profile code is designed to provide a dynamic contact angle
for the VOF function*/
```

```
DEFINE_PROFILE(con_ang, t, pos)
{
     /* First the various pointer variables are created*/
    face_t f;
    cell_t c;
    real feta_d, vel_Val[3], cont_Line_Vel, VOF_Normal[3];
    real cap_Num_A, cap_Num_R, finish_Cond;
    Thread *t0,*pt;


        /* Now the main loop goes through all the faces in the boundary */
        begin_f_loop(f,t)
        {
                /* The cell and phase threads are isolated */
                c=F_C0(f,t);
                t0=THREAD_T0(t);
                pt= THREAD_SUB_THREAD(t0,1);
                /* The main formulation is only applied if the VOF is >0 */
                if(C_VOF(c,pt)!=0.0 && C_VOF(c,pt)!=1.0)
                {
                /* The velocities are recorded in each direction */
                vel_Val[0]=C_U(c,t0);
                vel_Val[1]=C_V(c,t0);
                vel_Val[2]=C_W(c,t0);
                /* The VOF normals are brought in
                */
                VOF_Normal[0]=C_UDMI(c,t0,0);
                VOF_Normal[1]=C_UDMI(c,t0,1);
                VOF_Normal[2]=C_UDMI(c,t0,2);

                /*The contact line velocity is calculated from the dot product of
                VOF and Vel*/
                cont_Line_Vel=NV_DOT(vel_Val,VOF_Normal);

                /*The capillary number is found based on contact line velocity*/

                /*The dynamic contact angle is defined then stored in the profile*/
                        if(cont_Line_Vel<0.0) /*front part of the oil droplet*/
                        {
                        /* computing Ca with oil viscosity if oil is advancing*/
                        cap_Num_A=fabs((OIL_VISCOSITY*cont_Line_Vel)/SURF_TENS);
                        feta_d=(Hoff(cap_Num_A+inv_Hoff_150));
                        F_PROFILE(f,t,pos)=feta_d;
                        }
                        else /* rear part of the oil droplet*/
                        {
                        /* computing Ca with water viscosity if water is advancing*/
                        cap_Num_R=fabs((WAT_VISCOSITY*cont_Line_Vel)/SURF_TENS);
                        feta_d=(Hoff(cap_Num_R+inv_Hoff_30));
```

```
                feta_d=M_PI-feta_d;
                F_PROFILE(f,t,pos)=feta_d;
                 }
        }
}
end_f_loop(f,t)
```

Bibliography

S. Akin. Estimation of fracture relative permeabilities from unsteady state corefloods. *J. Petrol. Sci. Eng.*, 30(1):1–14, 2001.

J. Al-Besharah, O. A. Salman, and S. A. Akashah. Viscosity of crude oil blends. *Ind. Eng. Chem. Res.*, 26:2445–2449, 1987.

L. O. Alpak, L. W. Lake, and S. M. Embid. Validation of a modified carman-kozeny equation to model two-phase relative permeabilities. In *SPE Annual Technical Conference and Exhibition, Houston, Texas*. Society of Petroleum Engineers, October 1999.

M. Andrew, B. Bijeljic, and M. J. Blunt. Pore-by-pore capillary pressure measurements using x-ray microtomography at reservoir conditions: Curvature, snap-off, and remobilization of residual CO_2. *Water Resources Research*, 50(11):8760–8774, 2014a.

M. Andrew, B. Bijeljic, and M. J. Blunt. New frontiers in experimental geoscience: X-ray microcomputed tomography and fluid flow. *Microscopy and Analysis*, 28 (2):S4–S7, 2014b.

R. T. Armstrong, M. L. Porter, and D. Wildenschild. Linking pore-scale interfacial curvature to column-scale capillary pressure. *Advances in Water Resources*, 46: 55–62, 2012.

M. Bai and J. N. Chung. Analytical and numerical prediction of heat transfer and pressure drop in open-cell metal foams. *Int. J. of Thermal Sciences*, 50(6):869–880, 2011.

S. Bakke and P. E. Øren. 3-d pore-scale modelling of sandstones and flow simulations in the pore networks. *SPE Journal*, 2(2):136–149, 1997.

J. Baruchel, J. Y. Buffiere, E. Maire, Merle P., and Piex G. *X-ray tomography in material science*. Hermes Science Publications, Paris (FR), 2000.

W. D. Bascom, R. L. Cottington, and C. R. Singleterry. Contact angle, wettability and adhesion. *Advances in Chemistry*, 43:355–379, 1964.

J. Bear. *Dynamics of Fluids in Porous Media.* Dover Publications, New York, U.S.A., 1972.

J. Bear. *Fundamentals of Transport Phenomena in Porous Media.* Martinus Nijhoff, Dordrecht, 1984.

R. G. Bentsen and J. Anli. Using parameter estimation techniques to convert centrifuge data into a capillary pressure curve. *Trans. AIME*, 56, 1977.

S. Berg, A. W. Cense, J. P. Hofman, and R. M. M. Smits. Two-phase flow in porous media with slip boundary condition. *Transport in Porous Media*, 74(3):275–292, 2008. ISSN 1573-1634.

S. Berg, R. Armstrong, H. Ott, A. Georgiadis, S. A. Klapp, A. Schwing, R. Neiteler, N. Brussee, and A. Makurat. Multiphase flow in porous rock imaged under dynamic flow conditions with fast x-ray computed tomography. *Petrophysics*, 55 (4):304–312, 2014.

J. U. Brackbill, D. B. Kothe, and C. Zemach. A continuum method for modeling surface tension. *J. Comp. Phys.*, 100:335–354, 1992.

M. Bracke, F. De Voeght, and P. Joos. The kinetics of wetting: the dynamic contact angle. *Prog. Colloid Polym. Sci.*, 79:142–149, 1989.

R. H. Brooks and A. T. Corey. Properties of porous media affecting fluid flow. *Journal of the Irrigation and Drainage Division, Proceedings of the American Society of Civil Engineers*, 92(IR2):61–88, 1966.

S. E. Buckley and M. C. Leverett. Mechanism of fluid displacement in sands. *Trans., Petroleum Division of AIME*, 146:107–116, 1942.

T. Cadoret, D. Marion, and B. Zinszner. Influence of frequency and fluid distribution on elastic wave velocities in partially saturated limestones. *J. of Geophysical Research*, 100(B6):9789–9803, 1995.

P. C. Carman. Fluid flow through granular beds. *Transactions, Institution of Chemical Engineers*, 15:150–166, 1937.

Q. Chen, W. Kinzelbach, and S. Oswald. Nuclear magnetic resonance imaging for studies of flow and transport in porous media. *J. Environ. Qual*, 31:477–486, 2002.

G. V. Chilingarian. *Relationship between Porosity, Permeability and Grain Size Distribution of Sands and Sandstones.* Van Straaten, J. U. (Editor), Elsevier Science Publ. Co., Amsterdam, 1927.

R. L. Christiansen. *Multiphase flow through porous media.* KNQ Engineering, Salt Lake City, Utah, USA, 2008.

M. E. Coles, R. D. Hazlett, P. Spanne, W. E. Soll, E. L. Muegge, and K. W. Jones. Pore level imaging of fluid transport using synchrotron x-ray microtomography. *J. Pet. Sci. Tech.*, 19(1-2):55–63, 1998.

H. Dong and M. J. Blunt. Pore-network extraction from micro-computerized tomography images. *Phys Rev E*, 80:036307, 2009.

F. A. L. Dullien. *Porous media: fluid transport and pore structure.* Academic Press, New York, 1992.

P. Egerman, J. M. Lombard, and P. Bretonnier. A fast and accurate method to measure threshold capillary pressure of caprocks under representative conditions. In *International Symposium of the Society of Core Analysts, Trondheim, Norway.* Society of Core Analysts, September 2006.

I. A. Elbakri and J. A. Fessler. Segmentation-free statistical image reconstruction for polyenergetic x-ray computed tomography with experimental validation. *Physics in Medicine and Biology*, 48(15):2453, 2003.

R. O. Ezewu, W. Akinlolu, S. Siddiqui, A. Alquaraishi, and O. Okpelu. Capillary pressure determination using the micropore membrane technique: An experimental study. 2013.

L. A. Feldkamp, L. C. Davis, and J. W. Kress. Practical cone-beam algorithm. *Journal of the Optical Society of America A: Optics and Image Science, and Vision*, 1(6):612–619, 1984.

J. H. Ferziger and M. Perić. *Computational methods for fluid dynamics.* Springer, Berlin, 2001.

S. P. Friedman. Dynamic contact angle explanation of flow rate-dependent saturation-pressure relationships during transient liquid flow in unsaturated porous media. *J. Adhesion Sci. Technol.*, 13(12):1459–1518, 1999.

R. V. Garimella, M. J. Shashkov, and P. M. Knupp. Triangular and quadrilateral surface mesh quality optimization using local parametrization. *Computer Methods in Applied Mechanics and Engineering*, 193(9-11):913–928, 2004.

T. M. Geffen, W. W. Owens, D. R. Parrish, and R. A. Morse. Experimental investigation of factors affecting laboratory relative permeability measurements. *Trans., AIME*, 192:99–110, 1951.

O. Gerbaux, F. Buyens, V. V. Mourzenko, A. Memponteil, A. Vabre, J. F. Thovert, and P. M. Adler. Transport properties of real metallic foams. *J. Colloid Interf. Sci.*, 342:155–165, 2010.

D. E. Goldberg. *Genetic algorithms in search, optimization and machine learning.* Pearson Education Asia, 2002.

A. Gunstensen, D. H. Rothman, S. Zaleski, and G. Zanetti. A lattice-boltzmann model of immiscible fluids. *Physical Review A*, 43:4320–4327, 1991.

G. S. Gupta, J. D. Litse, V. Rudolph, and E. T. White. Flow visualization study in porous media using x-rays. *Steel. Res.*, 68(10):434–440, 1997.

E. B. Gutoff and C. E. Kendrick. Dynamic contact angles. *AIChE Journal*, 28(3): 459–466, 1982.

L. D. Hall, M. H. G. Amin, E. Dougherty, M. Sanda, J. Votrubova, K. S. Richards, R. J. Chorley, and M. Cislerova. MR properties of water in saturated soils and resulting loss of MRI signal in water content detection at 2 tesla. *Geoderma*, 80 (3,4):431–448, 1997.

L. Hao and P. Cheng. Pore-scale simulations on relative permeabilities of porous media by lattice boltzmann method. *Int. J. Heat Mass Transfer*, 53(9-10):1908–1913, 2010.

S. M. Hassanizadeh and W. G. Gray. Thermodynamic basis of capilllary pressure in porous media. *Wat. Resourc. Research*, 29(10):3389–3405, 1993.

R. D. Hazlett. Simulation of capillary-dominated displacements in microtomography images of reservoir rocks. *Transp. Porous Media*, 20:21–35, 1995.

S. M. Hazzanizadeh and W. G. Gray. Thermodynamic basis of capillary pressure in porous media. *Water Resource Research*, 29(10):3389–3405, 1993.

A. L. Herring, L. Andersson, D. L. Newell, J. W. Carey, and D. Wildenschild. Pore-scale observations of supercritical CO_2 drainage in bentheimer sandstone by synchrotron x-ray imaging. *Int. J. Greenhouse Gas Control*, 25:93–101, 2014.

M. Hilpert and A. Ben-Davis. Infiltration of liquid droplets into porous media: Effects of dynamic contact angle and contact angle hysteresis. *Int. J. Multiphase Flow*, 35:205–218, 2009.

R. L. Hoffman. A study of the advancing interface. I. Interface shape in liquid-gas systems. *Journal of Colloid and Interface Science*, 50(2):228 – 241, 1975. ISSN 0021–9797.

M. Honarpour, L. Koederitz, and A. H. Harvey. *Relative permeability of Petroleum Reservoirs*. CRC Press, Boca Raton, 2000.

P. Iassonov, T. Gebrenegus, and M. Tuller. Segmentation of x-ray computed tomography images of porous materials: a crucial step for characterization and quantitative analysis of pore structures. *Water Resour. Res.*, 45:W09415, 2009.

G. Jin, C. Torres-Verdin, F. Radaelli, and E. Rossi. Experimental validation of pore-level calculations of static and dynamic petrophysical properties of clastic rocks. In *SPE Annual Technical Conference and Exhibition, Anaheim, California, U.S.A.* Society of Petroleum Engineers, November 2007.

E. F. Johnson, D. P. Bossler, and V. O. Naumann. Calculation of relative permeability from displacement experiments. *Trans. AIME*, 216:370–372, 1959.

M. Josh, L. Esteban, C. Delle Piane, J. Sarout, D. N. Dewhurst, and M. B. Clennell. Laboratory characterization of shale properties. *J. Petrol. Sci. Eng.*, 88-89:107–124, 2012.

Z. Jovanović, F. Khan, F. Enzmann, and M. Kersten. Simultaneous segmentation and beam-hardening correction in computed microtomography of rock cores. *Comput. Geosc.*, 56:142–150, 2013.

A. C. Kak and M. Slanley. *Principles of Computerized Tomographic Imaging*. Society of Industrial and Applied Mathematics, New York, 1998.

T. Kanit, S. Forest, I. Galliet, V. Mounoury, and D. Jeulin. Determination of the size of the representative volume element for random composites: statistical and numerical approach. *Int. J. Solids Struct.*, 40(13-14):3647–3679, 2003.

Y. Keehm, T. Mukerji, and A. Nur. Relative permeability simulation using the two-phase lattice-boltzmann method. In *5-th Conference & Exposition on Petroleum Geophysics, Hyderabad, India*, pages 696–703. Petroleum Geophysics, 2004.

A. A. Keller, V. Broje, and K. Setty. Effect of advancing velocity and fluid viscosity on the dynamic contact angle of pertoleum hydrocarbons. *J. Petrol. Sci. Engin.*, 58:201–206, 2007.

R. A. Ketcham and D. W. Carlson. Acquisition, optimization and interpretation of x-ray computed tomographic imagery: applications in the geosciences. *Comput. Geosc.*, 27:381–400, 2001.

S. F. Kistler. *Hydrodynamics of wetting*. Taylor & Francis, New York, 1993. in *Wettability*.

D. Koroteev, O. Dinariev, N. Evseev, D. Klemin, A. Nadeev, S. Safonov, O. Gurpinar, S. Berg, C. van Kruijsdijk, R. Armstrong, M. T. Myers, L. Hathon, and H. de Jong. Direct hydrodynamic simulation of multiphase flow in porous rock. *Petrophysics*, 55(4):294–303, 2014.

J. Kozeny. Ueber kapillare leitung des wassers im boden. *Sitzungsbericht der Akademie der Wissenschaften*, 136:271–306, 1927.

E. Kreyszig. *Differential Geometry*. Dover, New York, 1991.

S. Krishnan, J. Y. Murthy, and S. V. Garimella. Direct simulation of transport in open-cell metal foams. *Int. J. Heat Transf.*, 128:793–799, 2006.

L. W. Lake and M. N. Panda. Estimation of single-phase permeability from parameters of particle-size distribution. *American Association of Petroleum Geologists Bulletin*, 78(7):1028–1039, 1994.

T. Langer, A. Belyaev, and H-P Seidel. Exact and approximate quadratures for curvature tensor estimation. In M. Desbrun and H. Pottmann, editors, *Eurographics Symposium on Geometry Processing*, Erlangen, Germany, 2005.

R. Lenormand, E. Touboul, and C. Zarcone. Numerical models and experiments on immiscible displacements in porous media. *J. Fluid Mech.*, 189:165–187, 1988.

L. Leu, S. Berg, F. Enzmann, R. T. Armstrong, and M. Kersten. Fast x-ray microtomography of multiphase flow in berea sandstone: A sensitivity study on image processing. *Transp. Porous Media*, 105:451–469, 2014.

M. C. Leverett. Capillary behavior in porous media. *Trans. Am. Inst. Min. Metall. Pet. Eng.*, 142:152–169, 1941.

D. Loeve, F. Wilschut, R. H. Hanea, J. G. Maas, P. M. E. van Hooff, P. J. van den Hoek, S. G. Douma, and J. F. M. Van Doren. Simultaneous determination of relative permeability and capillary pressure curves by assisted history matching several scal experiments. In *International Symposium of the Society of Core Analysts, Austin, Texas (USA)*. Society of Core Analysts, September 2011.

F. Lomeland and E. Ebeltoft. A new versatile capillary pressure correlation. In *Proceedings of the International Symposium of the Society of Core Analysts*, Abu Dhabi, UAE, 2008.

F. Lomeland, E. Ebeltoft, and W. H. Thomas. A new versatile relative permeability correlation. In *Proceedings of the International Symposium of the Society of Core Analysts*, Toronto, Canada, 2005.

A. G. Loomis and D. C. Crowell. Relative permeability studies: gas-oil and water-oil systems. *USBM Bulletin*, 599, 1962.

S. K. Matthï, S. Geiger, S. G. Roberts, A. Paluszny, M. Belayneh, A. Burri, A. Mezentsev, H. Lu, D. Coumou, T. Driesner, and C. A. Heinrich. Numerical simulation of multiphase fluid flow in structurally complex reservoirs. *Geological Soc. London Spec. Publ.*, 292(1):405–429, 2007.

C. A. McPhee. Relative permeability measurements: an inter-laboratory comparison. *Soc: Petrol. Engin.*, 28826:199–211, 1994.

P. Meakin and A. M. Tartakovsky. Modeling and simulation of pore-scale multiphase fluid flow and reactive transport in fractured and porous media. *Reviews of Geophysics*, 47(3), 2009. doi: 10.1029/2008RG000263.

C. Miller. Liquid water dynamics in a model polymer electrolyte fuel cell flow channel. Master's thesis, Dept. Mech. Eng., University of Victoria (CA), 2009.

J. Mitchell, T. C. Chandrasekera, D. J. Holland, L. F. Gladden, and E. J. Fordham. Magnetic resonance imaging in laboratory petrophysical core analysis. *Physics Reports*, 526(3):165 – 225, 2013.

N. R. Morrow. Physics and thermodynamics of capillary action in porous media. *Ind. Eng. Chem. Res.*, 62(6):32–56, 1970.

N. R. Morrow, P. J. Cram, and P. G. McCaffery. Displacement studies in dolomite with wettability control by octanoic acid. *Trans. AIME*, 253(2):221–232, 1973.

P. Mostaghimi, B. Bijeljic, and M. J. Blunt. Simulation of flow and dispersion on pore-space images. *SPE Journal*, 17(4):1131–1141, 2012.

P. Mostaghimi, M. J. Blunt, and B. Bijeljic. Computations of absolute permeability on micro-ct images. *Math. Geosc.*, 45(1):103–125, 2013.

J. Murison, R. Moosavi, M. Schulz, B. Schillinger, and M. Schroter. Neutron tomography as a tool to study immiscible fluids in porous media without chemical dopants. *Energy & Fuels*, 29(10):6271–6276, 2015.

B. D. Nichols and C. W. Hirt. Methods for calculating multi-dimensional, transient free surface flows past bodies. In *Proc. First Intern. Conf. Num. Ship Hydrodynamics*, Gaithersburg, ML, Oct. 1975.

B. D. Nichols and C. W. Hirt. Volume of fluid (vof) method for the dynamics of free boundaries. *Journal of Computational Physics*, 39(1):201–225, 1981.

J. E. Nordtvedt, H. Urkedal, E. Ebeltoft, K. Kolltveit, E. B. Petersen, A. Sylte, and R. C. Valestrand. The significance of violated assumptions on core analysis results. In *Proceedings of the International Symposium of the Society of Core Analysts*, Golden, Colorado (USA), 1999. Society of Core Analysts.

D. M. O' Carroll, K. G. Mumford, L. M. Abriola, and J. I. Gerhard. Influence of wettability variations on dynamic effects in capillary pressure. *Wat. Resourc. Research*, 46, 2010.

A. S. Odeh. Effect of viscosity ratio on relative permeability. *Trans. AIME*, 216: 346–353, 1959.

X. Pan, E. Y. Sidky, and M. Vannier. Why do commercial CT scanners still employ traditional, filtered back-projection for image reconstruction? *Inverse Problems*, 25(12):123009, 2009.

A. C. Payatakes. Dynamics of oil ganglia during immiscible displacement in water-wet porous media. *Ann. Rev. Fluid Mech.*, 14:365–393, 1982.

A. E. Peksa, K. H. A. A. Wolf, and P. L. J. Zitha. Bentheimer sandstone revisited for experimental purposes. *Marine and Petroleum Geology*, 67:701–719, 2015.

E. Perfect, C.-L. Cheng, M. Kang, H. Z. Bilheux, J. M. Lamanna, M. J. Gragg, and D. M. Wright. Neutron imaging of hydrogen-rich fluids in geomaterials and engineered porous media: A review. *Earth-Science Reviews*, 129:120–135, 2014.

M. Piller, G. Schena, M. Nolich, S. Favretto, F. Radaelli, and E. Rossi. Analysis of hydraulic permeability in porous media: From high resolution X-ray tomography to direct numerical simulation. *Transport in Porous Media*, 80(1):57–78, 2009.

PRORES. SENDRA - a state of the art software tool for proper analysis and quality control of relative permeability and capillary pressure. https://www.prores.no/sendra/. Accessed: 2016-02-03.

J. Radon and P. C. Parks. On the determination of functions from their integral values along certain manifolds. *IEEE Trans. Med. Imaging*, 5(4):170–176, 2009.

O. Rezki, S. Yousef, Y. Peysson, B. Bazin, E. Maire, and O. Vizika. Pore-scale to core-scale study of capillary desaturation curves using multi-scale 3d imaging. In *SCA International Symposium, Napa Valley, California, USA*. Society of Core Analysts, September 2013.

S. Roels and J. Carmeliet. Analysis of moisture flow in porous materials using microfocus x-ray imaging. *Int. J. of Heat and Mass Transfer*, 49:4762–4772, 2006.

S. Roels, O. Ott, and P. L. J. Zitha. μ-ct analysis and numerical simulation of drying effects of CO_2 injection into brine-saturated porous media. *Int. J. Greenhouse Control*, 27:146–154, 2014.

S. Rusinkiewicz. Estimating curvatures and their derivatives on triangle meshes. In *Proceedings of the 3D Data Processing, Visualization, and Transmission, 2nd International Symposium IEEE Computer Society*, pages 486–493, Washington, DC, USA, 2004.

A. Saha, S. Mitra, M. Tweedie, S. Roy, and J. McLaughlin. Experimental and numerical investigation of capillary flow in su8 and pdms microchannels with integrated pillars. *Microfluidics and Nanofluidics*, 7(4):451–465, 2009. ISSN 1613-4982.

R. A. Salathiel. Oil recovery by surface film drainage in mixed-wettability rocks. *J. Petrol. Technol*, 25:1216–1224, 1973.

H. Samet. *Foundations of multidimensional and metric data structures*. Morgan Kaufmann Publishers, San Francisco, USA, 2006.

A. E. Scheidegger. *The Physics of Flow through Porous Media*. University of Toronto Press, Toronto, CA, 1974.

G. Schena and S. Favretto. Pore space network characterization with sub-voxel definition. *Transport in Porous Media*, 70(2):181–190, 2004.

A. Semechko. Suite of functions to perform uniform sampling of a sphere. MathWorks File Exchange website, url=https://www.mathworks.com/matlabcentral/fileexchange/37004-suite-of-functions-to-perform-uniform-sampling-of-a-sphere, Mar 2015.

D. Silin and T. Patzek. Pore space morphology analysis using maximal inscribed spheres. *Physica A: Statistical Mechanics and its Applications - Journal - Elsevier*, 371:336–360, 2006.

S. Succi. *The Lattice Boltzmann Equation for Fluid Dynamics and Beyond*. Oxford University Press, Oxford, 2001.

H. Tang, L. C. Wrobel, and Z. Fan. Tracking of immiscible interfaces in multiple-material mixing processes. *Comput. Mater. Science*, 29:103–118, 2004.

L. H. Tanner. The spreading of silicone oil drops on horizontal surfaces. *Journal of Physics D: Applied Physics*, 12(9):1473, 1979.

Z. Tavassoli, J. N. Carter, and P. R. King. Analysis of history matching errors. *Computational Geosciences*, 9(2-3):99–123, 2005.

G. F. Teletzke, H. T. Davis, and L. E. Scriven. Wetting hydrodynamics. *Rev. Phys. Appl.*, 23:989–1007, 1988.

B. Tiab and E. C. Donaldson. *Petrophysics: theory and practice of measuring reservoir rock and fluid transport properties.* Elsevier Publications, Oxford, UK, 2004.

V. Tidwell, L. Meigs, T. Christian-Frear, and C. Boney. Effects of spatially heterogeneous porosity on matrix diffusion as investigated by x-ray absorption imaging. *J. of Contaminant Hydrology*, 42:285–302, 2000.

J. Toth, T. Bodi, P. Szucs, and F. Civan. Convenient formulae for determination of relative permeability from unsteady-state fluid displacements in core plugs. *J. Petrol. Sci. Eng.*, 36(1-2):33–44, 2002.

P. van Hemert, E. S. J. Rudolph, and P. L. J. Zitha. Micro computer tomography study of potassium iodide precipitation in bentheimer sandstone caused by flow-through CO_2 drying. *Energy Procedia*, 37:3331–3346, 2013.

H. J. Vinegar and S. L. Wellington. Tomographic imaging of three-phase flow experiments. *Review of Scientific Instruments*, 58(1):96–107, 1987.

O. V. Voinov. Hydrodynamics of wetting. *Fluid Dynamics*, 11(5):714–721, 1976.

D. Wildenschild and A. Sheppard. X-ray imaging and analysis techniques for quantifying pore-scale structure and processes in subsurface porous medium systems. *Adv. Water Resour.*, 51:217–246, 2013.

G. P. Willhite. *Waterflooding.* SPE textbook series. Society of Petroleum Engineers, 1986. ISBN 9781555630058.

O. B. Wilson and B. G. Tjetland. Porous plates influence on effective drainage rates in capillary pressure experiments. In *Proceedings - SCA 2001*, Edimburgh, Scotland, 2001. Society of Core Analysts.

S. Wolfram. Cellular automaton fluids 1: Basic theory. *Journal of Statistical Physics*, 45:471–526, 1986.

M. Wu, Q. Yang, A. Maier, and R. Fahrig. A practical statistical polychromatic image reconstruction for computed tomography using spectrum binning. volume 9033, 2014.

H. Yagou, Y. Ohtake, and A. Belyaev. Mesh smoothing via mean and median filtering applied to face normals. pages 124–131, 2002.

D. Yang, Y. Gu, and P. Tontiwachwuthikul. Wettability determination of the crude oil-reservoir brine-reservoir rock system with dissolution of CO_2 at high pressures and elevated temperatures. *Energy & Fuels*, 22:2362–2371, 2008.

Y. Zaretskiy, S. Geiger, and K. Sorbie. Direct numerical simulation of pore-scale reactive transport: applications to wettability alteration during two-phase flow. *Int. J. Oil Gas Coal Tech.*, 5(2-3):142–156, 2012.

H. Zhang, S. He, C. Jiao, G. Luan, S. Mo, and X. Guo. Determination of dynamic relative permeability in ultra-low permeability sandstones via x-ray ct technique. *Journal of Petroleum Exploration and Production Technology*, 4(4):443–455, 2014.